

CARDIFF UNIVERSITY
SCHOOL OF PHYSICS AND ASTRONOMY



**THE SILICON
COLD ELECTRON BOLOMETER**

by

THOMAS LEONARD ROBERT BRIEN

February 2015

A THESIS SUBMITTED TO CARDIFF UNIVERSITY FOR THE
DEGREE OF DOCTOR OF PHILOSOPHY

To ...

Acknowledgements

Firstly I'd like to thank the academy.

Contents

Acknowledgements	i
Contents	iii
1 Introduction	1
2 The Concept of Silicon Cold Electron Bolometers	3
2.1 Introduction	3
2.2 The Principle of a Bolometer	4
2.3 The History of Cold Electron Bolometer Development	5
2.4 The Advantages & Disadvantages of Cold Electron Bolometers	9
3 The Theory of Cold Electron Bolometers	11
3.1 Introduction	11
3.2 Tunnelling Barriers	11
3.2.1 Formation of Insulating Layers	12
3.3 The Tunnelling Current	16
3.4 The Cooling Power	24
3.5 The Responsivity	30
3.6 The Sources of Electrical Noise	34
3.7 The Noise Equivalent Power	39
4 The Properties of Doped and Strained Silicon	45
4.1 Introduction	45
4.2 Intrinsic semiconductors	45
4.3 Doped semiconductors	47
4.4 Carrier Mobility	50

4.5	Strained Semiconductors	53
5	Detector Design & Fabrication	55
5.1	Introduction	55
5.2	Detector Design	55
5.2.1	Antenna Design	56
5.3	Detector Fabrication	60
5.4	Material Properties	62
6	Cryogenic Testbeds	65
6.1	Introduction	65
6.2	Sorption Refrigerators	66
6.3	Adiabatic Demagnetisation Refrigeration	69
6.4	Systems Used in This Work	71
6.4.1	Pulse Tube Cooled Cryostat with He10 Sorption Refrigerator	72
6.4.2	Liquid Helium Cryostat with Adiabatic Demagnetisation Re- frigerator	75
6.4.3	Liquid Helium Cryostat with He7 sorption refrigerator	76
6.5	Detector Holder	78
7	Detector Readout	81
7.1	Introduction	81
7.2	Requirements of the Readout System	82
7.3	Initial Testing System	82
7.3.1	Initial Readout System	82
7.3.2	Initial Bias System	88
7.4	Revisions to the Initial Bias System	92
7.4.1	Changes Made and Advantages	92
7.4.2	Performance of Updated Bias System	94
7.5	Final Testing System	97
7.5.1	Reason for replacement	97
7.5.2	Final Readout System	98
7.5.3	Final Bias System	105
7.6	Cross-Correlated Noise Measurement	108
7.6.1	Convolution	109
7.6.2	Cross Correlation	112

7.6.3	Application of Cross Correlation to Detector Readout	112
7.7	Summary of Readout and Biasing Systems	116
8	Results: Dark Measurements	119
8.1	Introduction	119
8.2	Unstrained Silicon	119
8.3	Strained Silicon	124
8.4	Comparison of Unstrained & Strained Detectors	128
Bibliography		129
Acronyms		137
Glossary		139
List of Figures		145
List of Tables		149

Chapter One

Introduction

'Begin at the beginning,' the King said gravely, 'and go on till you come to the end: then stop.'
— Lewis Carroll, *Alice in Wonderland*

Chapter Two

The Concept of Silicon Cold Electron Bolometers

Probably just going to wrap all of this into the introduction

2.1 INTRODUCTION

Bolometric detectors operate by accurately measuring the temperature of an absorbing element. Incoming radiative power causes the temperature of this element (the absorber) to increase and it is the increase which is measured. From this it follows that the greater the incident power the larger the increase in temperature. It can also be seen that for a bolometric to have a very high sensitivity (i.e. produce a measurable change in temperature for very low levels of incident power) it must be well isolated from its surroundings. It is also clear that the thermometer used must be capable of measuring extremely small changes in temperature, in practice this can mean changes as low a one millikelvin. The Silicon Cold Electron Bolometer offers benefits in both of these areas: the use of highly-doped silicon as an absorber allows the charge carriers (the actual absorbers) to be extremely well decoupled from the atomic lattice; and, when electrically biased appropriately, the current flowing through the structure is highly dependant on the temperature of these carriers. Further benefits of these devices are that natural isolation of charge carriers from there surrounds removes the requirements for more complicated arrangements often used to produce the same result, this removes the need

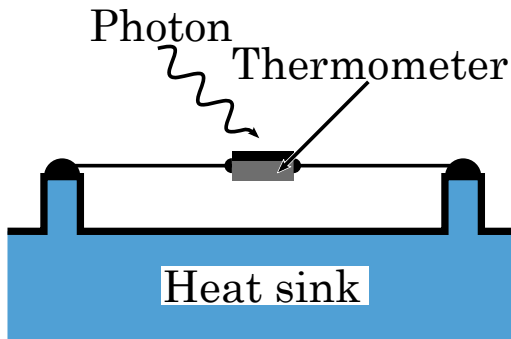


Figure 2.1: Schematic of a simple bolometer. An electrical thermometer is suspended above a heat sink by its wiring which acts as a weak thermal link to the heat sink. One side of the thermometer is painted black to increase the absorption on incident radiation. Incident power on the painted surface of the thermometer causes an increase in temperature which can be measured. Heat is removed from the thermometer via its wiring.

for complicated structures to be fabricated; furthermore, because the current flowing through a cold electron bolometer preferentially removes the most energetic electrons (the hottest), these devices can offer extremely small thermal time constants.

2.2 THE PRINCIPLE OF A BOLOMETER

Bolometers operate by measuring, to a high sensitivity, the temperature of an absorbing element. If radiative power is incident upon this absorber it will be absorbed resulting in the temperature of the absorber increasing. The greater the level of incident power then the larger the increase in the temperature of the absorber. In order to produce a sensitive bolometer two things need to be optimising: the change in temperature per unit power absorber (the thermal responsivity, S_T) needs to be as large as possible, this can be achieved by decoupling the absorber from its surroundings (such as to reduce the thermal mass of the absorber); or ensuring that the thermometer used to measure the change in the absorber's temperature is capable of measuring extremely small changes in temperature.

Figure 2.1 illustrates a basic form of bolometer. A simple electrical thermometer (such as a piece of germanium) is suspended from a heat sink via its wiring.

When power is absorbed the temperature of the material increases accordingly which results in a change in the material's electrical resistance. Heat removed to the heat sink via the thermometer's wiring. This leads to one common issue experienced when designing a bolometric detector: it is highly desirable for the time constant of the detector (the minimum time between measurable detection events) to be as small as possible, this requires the absorbed power to be removed from the absorbing element as rapidly as possible which in turn necessitates a strong thermal link between the absorber and the heat sink. However, increasing the thermal link between the heat sink and the absorber also has the effect of decreasing the sensitivity since the change in temperature within the absorber, for a given amount of absorber power, is also reduced. In most cases one has to find a trade-off between speed of operation and the sensitivity of the detector.

hunt a reference
for this

Ref.

2.3 THE HISTORY OF COLD ELECTRON BOLOMETER DEVELOPMENT

Development of the Cold Electron Bolometers has combined the developments of two fields to produce small, sensitive, and fast bolometers. These fields are those of Hot Electron Bolometers (HEBs) and tunnel-barrier superconducting electron refrigerators (also referred to as microrefrigerators or e-fridges).

Although the phenomenon of heat transport between two superconductors separated by an insulator (SIS) was first described by Parmenter (1961) as a way of improving superconductivity in one of the superconductors, it was not until 1994 that heat extraction from electrons in a normal metal island (copper in this case) to a superconductor via an insulator (NIS) was first observed by Nahum, Eiles, and Martinis (1994). From this point several improvements were made, notably including the work of Leivo, Pekola, and Averin (1996) who used a symmetric structure in which the normal island is sandwiched between the insulator-superconductor contacts (SINIS); this allowed for replacement of the extracted electrons by carriers of lower energy, improving the cooling power of such a device while also allowing for operation in both polarities. This approach of symmetric junctions allowed for electrons to be cooled from the lattice temperature of 300 mK to close to 100 mK. An interesting development in this field, although not directly applicable to cold

electron bolometers, was the work of Clark et al. (2005), who used Normal metal-Insulator-Superconductor (NIS) based electron coolers to cool a membrane, as well as its contents, from 320 mK to 225 mK; this work was also reported in Nature by Pekola (2005).

Although first proposed in 1961 by Parmenter enhancement of superconductivity through the use of Superconductor-Insulator-Superconductor (SIS) junction was first observed by Chi and Clarke (1979). However, Manninen et al. (1999), who used a slightly different arrangement whereby the a central superconductor is sandwiched by insulating contacts to a different superconductor (SIS'IS), were the first to show directly that in this arrangement the electrons were being cooled below the temperature of the lattice.

The increasing interest in the these electron refrigerators led to the work of Savin et al. (2001) who first demonstrated that an effective electron refrigerator could be formed by replacing the normal metal island in a SINIS with a highly doped semiconductor (SSmS). One immediate advantage of this device was that since it used naturally forming Schottky barriers in place of the oxide layers used in types of device fabrication was made simpler. Savin et al. showed that such a device was capable of cooling the electrons in the semiconductor from the lattice temperature of 160 mK to 120 mK. While this initial cooling was minimal, by 2003 Savin et al. had improved these devices such that they were now capable of cooling from 150 mK to less than 75 mK. Further improvements to SSmS coolers were made by Prest et al., 2011 who—by using a strained, highly doped semiconductor as the central island—were able to cool the electrons in the semiconductor from 300 mK to 174 mK.

While the use of the so-called *hot electron effect* to create a mixing heterodyne type detector was first described by Arams et al. (1966) the Hot Electron Bolometer was first envisaged by Nahum, Richards, and Mears (1993), who described a detector where incoming optical power heated the electrons in a normal metal absorber above the temperature of the lattice. The thermal isolation required to enable this independent heating of electrons comes from the fact that at low temperatures (typically less than 1 K) the inelastic collisions between the electrons and the atomic lattice are extremely infrequent, this is also factor in the effectiveness of the electron refrigerators described above. Nahum proposed the use of an insulating tunnel contact to a superconducting electrode to measure the temperature of the charges in the absorber. This is the same arrangement of

a Normal metal-Insulator-Superconductor (NIS) structure s used in the electron refrigerators described above. They noted that since the tunnelling current in a NIS junction is exponentially dependant on the temperature of the charges (as will be shown in Section 3.3 of Chapter 3), this arrangement acts as an extremely sensitive thermometer.

There have been many notable publications and developments in the field of Hot Electron Bolometers. Of particular note is the work of Karasik and Cantor who has shown that devices similar to those described by Nahum, Richards, and Mears but using a thin strip of superconductor as the absorber are capable operating with a noise equivalent power of 3×10^{-12} (Karasik et al., 2007; Karasik and Cantor, 2011). These levels of sensitivity make Hot Electron Bolometers an extremely exciting prospect for the next generation of both space and ground based telescopes. However, the speed of these devices is limited by the electron-phonon relaxation time (Karasik et al., 2007, reports a time constant of 30 μ s). Furthermore, in order to achieve the thermal isolation required for highly sensitive detectors, these devices require the fabrication of absorbing islands of size on the order of $1 \times 1 \mu\text{m}$ or smaller, with the need for contacts much smaller than this to be fabricated (Karasik and Cantor, 2011). The final undesirable feature of Hot Electron Bolometers is the need to degrade (slow) the thermal time constant in order to achieve high sensitivities (Karasik et al., 2000), in order to again increase the speed of the device, electrothermal feedback (as described by Irwin, 1995). While this use electrothermal feedback allowed microsecond scale thermal constants to be achieved it also increased the complexity of the detector operation and restricted the biasing signal to a voltage bias.

One important difference between the work of Nahum, Richards, and Mears and Karasik et al. is how their respective detectors were readout. As mentioned above, Nahum, Richards, and Mears used a NIS tunnelling contact to act as an extremely sensitive electron thermometer. Karasik et al. on the other hand simply used the change in the resistance of the superconducting absorber (which was biased such that it was held on the superconducting transition) as the means of measuring the absorbed power (this is the same technique as used for the transition edge sensor type of detector).

The concept of using the *cold electron effect* that had been shown with electron refrigerator devices, combined with the thermal isolation of the electrons from the phonons used in Hot Electron Bolometers, was first proposed in 1998 by Kuzmin,

Add glossary entry: add Electrothermal feedback

Add glossary entry: TES

Devyatov, and Golubev who further elaborated on his idea in 2000 and 2003. They described how the using NIS junctions could be used to lower the temperature of the electrons in a normal metal absorber to some rest temperature. Incident power absorbed within the absorber cause the electrons to heat up above the established rest temperature (much as in the case of the Hot Electron Bolometer). Kuzmin, Devyatov, and Golubev explained that the same NIS junctions used to cool the electrons could be used as highly sensitive electron thermometers (as had been used by Nahum, Richards, and Mears, 1993). Finally, Kuzmin, Devyatov, and Golubev showed that the time constant of such a detector would be limited by the electron tunnelling time as opposed so the thermal conductance between the electron and phonon systems. This integrated solution for both cooling and readout formed the first example of what could be called a cold electron bolometer.¹

Since the original description of a cold electron bolometer there have been numerous publications on the topic. The most prolific author on subject has been Leonid Kuzmin, who has shown the potential of such detectors to reach speeds in the order of nanoseconds (Kuzmin, 2004) and has been involved in the first optical measurement of the sensitivity of a metallic CEB detector (Otto et al., 2013), which was shown to have an amplifier limited noise equivalent power of $3.5 \times 10^{-17} \text{ W Hz}^{-1/2}$.

The work of Kuzmin et al. concentrated on Cold Electron Bolometers where the absorbing element was made from either a normal metal or a superconductor. As such, this devices are analogous to the NIS and SIS' types of electron refrigerator described earlier in this section. Due to the success of Prest et al. (2011) in achieving excellent levels of electron cooling a logical step in the development of Cold Electron Bolometers was to replace the normal metal or superconducting absorber with a highly degenerately doped semiconductor. Such a device was first described and characterised by Brien et al. (2014) and is further described in this thesis.

¹For this definition of a CEB the selection criterion was that the detector must be consciously designed to utilise direct electron to cooling with absorbed power heating the electrons above their cooled temperature.

2.4. THE ADVANTAGES & DISADVANTAGES OF COLD ELECTRON BOLOMETERS

2.4 THE ADVANTAGES & DISADVANTAGES OF COLD ELECTRON BOLOMETERS

Cold Electron Bolometers have been shown to have several advantages over other forms of bolometric detectors. Amongst these are: an extremely small thermal time constant (Kuzmin, 2004, shows this to be of the order of 10 ns), high optical sensitivities (Otto et al., 2013, achieved a noise equivalent power of 3.5×10^{-17} WHz $^{-1/2}$ —although this was limited by the readout amplifier), robust construction since now suspend membrane or back etching is required for thermal isolation, and (as shown by Salatino et al., 2014) a low susceptibility to cosmic rays.

One key disadvantage of Cold Electron Bolometers is that they cannot be connected together into an array in a way that facilitates simple readout of the array. This is the case for all bolometric detectors since there is no trivial way of reading the resistance of a number of elements on a single readout line. While being a broad issue in the field of bolometric detectors several schemes have been proposed and utilised to allow large—up to ten thousand pixels in the case of the SCUBA-2 instrument on the James Clark Maxwell Telescope Holland et al. (2013)—arrays of bolometric detectors. The two most common schemes adopted are frequency-division multiplexing and time-division multiplexing whereby the signals from the various detectors are combined such that the signal from any individual detector only contributes a small part of the total signal received at the readout electronics. Time-division multiplexing operates by the signal switching sequentially between the sources in time intervals. For example, if ten devices are to be read in one second then every 100 ms the readout system would switch to measuring the next device; this requires that each detector has an amplifier or other component which can be switched on and off. Frequency-division multiplexing on the other hand works by modulating a carrier wave, which has a specific frequency. This modulation is typically in the carrier's frequency (i.e. shifting the frequency of the signal from the carrier's rest frequency) although parameters such as the carrier's amplitude or phase may also be used. As the value of the measured quantity varies so to does the level of modulation. The frequency of the carrier wave associated with each device is different and is distributed across some frequency range. All the carrier waves in the frequency range are summed together allowing the information from several devices to be read on a single line. At a following stage in the

Add glossary entry: FDM TDM acr and gls

readout system these signals are demultiplexed by mixing the signal with a signal from a local oscillator whose frequency is the same as the original carrier. Using this approach multiple signal are read simultaneously using a single line.

Multiplexing techniques have been used to allow larger arrays of bolometric detectors to be deployed on both ground or balloon-based mission, and space based missions. Some major (historical, current, or planned) instruments of particular note which have used these techniques include: The KECK array of telescopes measuring the polarisation of the cosmic microwave background (CMB) at the South Pole, each telescope uses time-division multiplexing to readout 512 transition edge sensors across 16 channels (Orlando et al., 2010); SCUBA-2, a UK lead instrument at the John Clark Maxwell Telescope (JCMT) in Hawaii, which also utilises time-division multiplexing to readout an array of 10,240 transition edge sensors across only eight channels (Holland et al., 2013); the XMS instrument on NASA and ESA's jointly proposed IXO mission plans to use frequency-division multiplexing to read 1,600 pixels across 40 channels (Hartog et al., 2011); finally the SAFARI instrument on JAXA and ESA's joint SPICA mission² will use frequency-division multiplexing to readout arrays of 6,000 detectors using 160 channels.

Of particular interest to the field of Cold Electron Bolometers is the work of Schmidt et al. (2005) who has proposed a scheme where frequency-division multiplexing is used to readout arrays of up to 100,00 Hot Electron Bolometers. While the scheme devised by Schmidt et al. was intended for use with Hot Electron Bolometers, due to the similarities between the two detector types, it should prove compatible with Cold Electron Bolometers.

Add section on applications???

²In 2013 it was decided that the current scheme for delivering SPICA would not produce robust and timely implementation and ESA ceased to fund the development as of autumn 2013 (ESA, 2014). However, work is continuing (SRON, 2014) with the hope of launching SPICA in 2025.

Chapter Three

The Theory of Cold Electron Bolometers

3.1 INTRODUCTION

As with all areas of study within physics the fabrication and testing of Cold Electron Bolometers brings together elements from several fields including. These include concepts from quantum mechanics such as electron tunnelling, cryogenics and low temperature physics, electronics, as well as solid state physics. The study and testing of a Cold Electron Bolometer requires a strong understanding of these areas as well as the general grounding in the field of instrumentation and its associated vocabulary. These are covered in the following sections and chapters.

3.2 TUNNELLING BARRIERS

As will be explained in the following sections the Cold Electron Bolometer direct removes hot electrons from the detector's absorber. This thermally selective removal of charges is made possible through the use of a tunnelling barrier. These tunnelling barrier allows the electron systems on either side to be separated (i.e., the energy levels in the two do not have to be aligned).

Several types of tunnelling barriers exist however only those involving a superconductor shall be considered here since this is a requirement of the thermal selection required for a Cold Electron Bolometer. The four main types of contact used in Cold Electron Bolometers are:

Normal metal-Insulator-Superconductor (NIS) The simplest (at least conceptually). The two sides (the normal metal and the superconductor) are separated by an insulating layer (typically an oxide layer).

Superconductor-Insulator-Superconductor (SIS) This is essentially the same as the arrangement described above expect the normal metal is replaced by the same material as is used on the other side of the barrier.

Superconductor-Insulator-(different) Superconductor (SIS') A further progression of the systems already described. Here the materials on either side of the insulator are both superconductors but have different energy gaps (they are different superconductors).

Semiconductor-Superconductor (SmS) This structure replaces the insulator with a Schottky barrier which forms naturally between the semiconductor and a metal (or superconductor). Typically (and for all the work describe din this thesis) a highly doped semiconductor, which can be thought of as being metallic (there is no discernible band gap), is used.

Add glossary

entry: add Schottky Barrier

3.2.1 FORMATION OF INSULATING LAYERS

From the above list it can be seen that only two types of insulating barriers are typically used in the fabrication of Cold Electron Bolometers. These are: oxide layers and Schottky barriers. While both of these can be thought of as performing the same function their formation is very different. An oxide layer requires an additional stage during the device fabrication process, where oxygen is introduced to the evacuated deposition chamber. A Schottky barrier on the other hand will form naturally between a semiconductor and a metal (or superconductor), this means no additional fabrication stages are required.

An oxide insulating layer forms ionic bonds between the atoms of the metal and the oxygen atoms. This causes the outer electrons in the metal, which previously were *free* and available for current flow, to no longer be able to flow as current and thus the resistance of the material is greatly increased.

The formation of an oxide layer (illustrated form the growth of aluminium oxide in Figure 3.1) is conceptually simple. Since aluminium is commonly used as one side of a tunnelling contact aluminium oxide often forms the insulating oxide, because of this Figure 3.1 and the following explain the growth of an aluminium oxide layer (there are several other oxide layers used). After the metal

These images are

PNGs and need
changing to PDFs

cite

error is fixed

list and cite

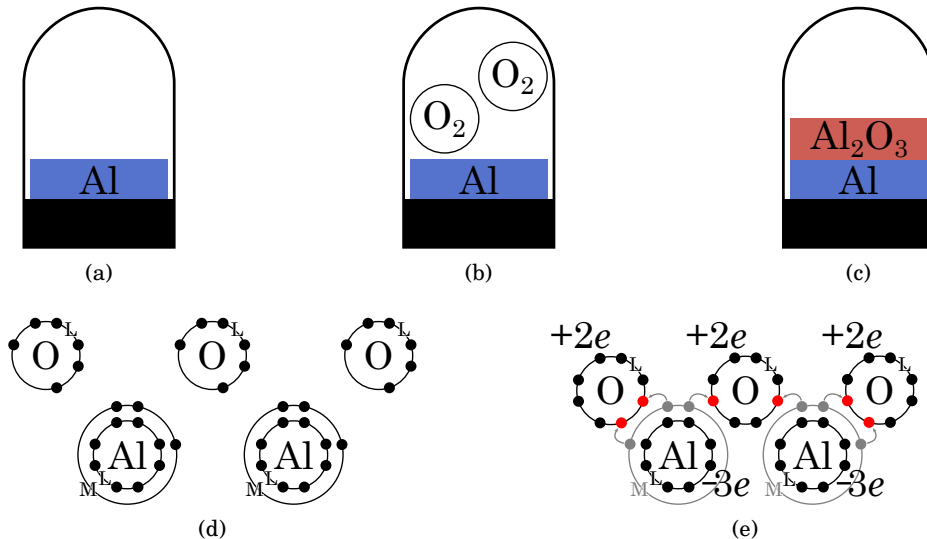


Figure 3.1: Growth (a)–(c) and ionic bond formation (d) and (e) of an aluminium oxide (Al_2O_3) layer. (a) Aluminium has been deposited (usually via evaporation) in a vacuum. (b) Oxygen is introduced into the evaporation chamber. (c) The oxygen atoms form ionic bond with the aluminium, this causes the growth of an aluminium oxide layer of the surfaces of the deposited aluminium. (d) Oxygen and aluminium atoms prior to bonding; oxygen contains six electrons in the L electron shell ($1s^2 2s^2 2p^4$), aluminium contains a full L electron shell and has three electrons in its M shell ($1s^2 2s^2 2p^6 3s^2 3p^1$). (e) The electrons from the M shells in the aluminium atoms (shown in grey for clarity) move to the L shell of the oxygen atoms (shown as the red electrons), this is the formation of ionic bonds and results in both the oxygen and aluminium atoms having their L shells filled (for tidiness the full K shell is not shown).

has been deposited by evaporation or other means (Figure 3.1a) oxygen is introduced into the deposition chamber (Figure 3.1b). The outermost electrons from the aluminium (those in the third shell, the M shell) move to the vacant states in the outer shell of the oxygen atoms (oxygen has two vacant electron states in its second shell, the L shell) forming ionic bonds between the aluminium and the oxygen, this is shown in Figures 3.1d and 3.1e. This results in a layer of aluminium oxide (Al_2O_3) forming on top of the deposited aluminium (Figure 3.1c).

While conceptually simple, in order to produce an even, high quality layer of

a desired thickness great care needs to be taken as to both the quantity of gas introduced and the temperature of the during the introduction of the oxygen gas (Cabrera and Mott, 1949; Jaeger et al., 1991). The addition of an oxide layer also necessitates an additional step in the fabrication along with the required equipment to add and monitor the flow of gas into the deposition chamber.

As opposed to an oxide layer a Schottky barrier will form naturally between a metal and a semiconductor. the barrier is formed as the electrons in the two materials move to cause the Fermi-energy in the two materials to be aligned. The concept of a naturally forming potential barrier between a semiconductor and a metal was first suggested by Schottky (1939) whose original explanation is illustrated in Figure 3.2

Schottky's explanation was that, after the semiconductor has been brought into contact with the normal metal, the electrons in the conduction band of the semiconductor (the most energetic) are able to move to the lower (energetically favourable) states above the Fermi-level in the metal (illustrated in Figure 3.2b) leaving behind positive;y charged *donor* ions. This causes the Fermi-level within the semiconductor to decrease since there are fewer electrons in the conduction band. This movement of electrons continues until there is an equilibrium established between the electron systems in the two materials (i.e. when the Fermi-levels are aligned). Away from the interface between the metal and the semiconductor the valence and conduction bands move relative to the Fermi-level however at the interface the bands move differently since it is these electrons which have moved. This causes the phenomenon of *band-bending* and the formation of a depletion region (from E_f to $E_f + \Phi_B$) in the semiconductor at the interface.

Schottky barriers are, in theory, simple to fabricate. All that is required is for the two materials to be deposited sequentially. An important caveat is that one must ensure that the first material deposited (often the semiconductor) is free of impurities or unwanted surface films (such as oxide layers). This is simple if the entire fabrication process can be performed in a single system under continuous vacuum. If however the device needs to be removed from the protection of the evacuated deposition system, to be patterned for example, then it is important to ensure that the surfaces is thoroughly cleaned prior to the deposition of the second material (a good description of surface preparation requirements is given by Roccaforte et al., 2003). Should the surface of the first material not be sufficiently cleaned contamination may either cause an insulating layer to form which, while

These are PNGs
and need setting
back to vectors
when pdflatexc fix
is done

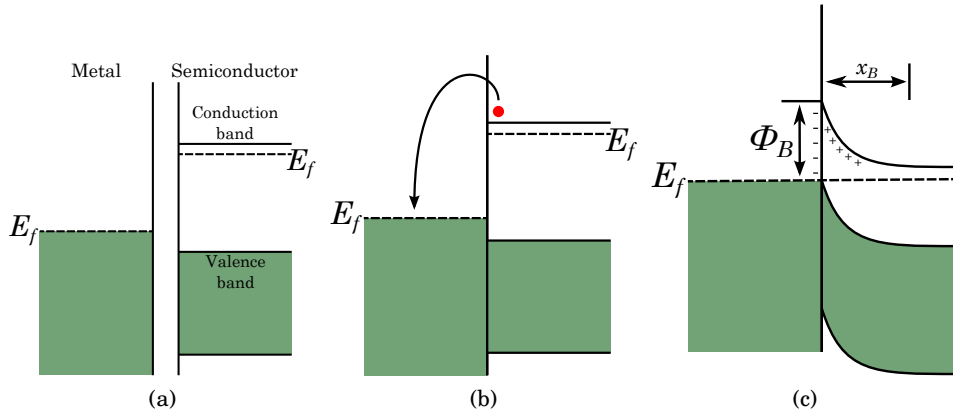


Figure 3.2: Formation of a Schottky barrier between a metal and a n-doped semiconductor. (a) before being brought into contact the energy distribution in the metal and the semiconductor are independent with the Fermi-level (E_f , shown as the dashed line) sitting at the top of the occupied states in the metal (shown at $T = 0$ K) and just below the conduction band of the semiconductor. (b) Immediately after the metal and semiconductor are brought into contact the energy levels are unchanged however electrons (red circle) start to move from the conduction band of the semiconductor to the lower energy. These electrons leave behind positively charged ions or *donor states*. (c) The movement of the most energetic electrons from the semiconductor causes the Fermi-level to move, this continues until the Fermi-level in both the materials is the same. Away from the interface the band structure of the semiconductor move relative to the Fermi-level; at the interface however this is not the case, this causes the phenomenon known as *band-bending* in the semiconductor. The height of the Schottky barrier established is related to the difference between the vacuum level in the two materials and is given by Φ_B .

itself acting as a tunnelling barrier, will inhibit or stop the development of a Schottky barrier; or alter the Fermi-level of the material and thus alter the Schottky barrier height (as discussed in the following paragraph).

One cannot simply combine any combination of semi-conductor and metal to create a Schottky barrier. As can be seen from the description above and Figure 3.2 there needs to be a difference between the inherent Fermi-levels in the two materials. If this is not the case, when the two materials are brought together there will be minimal movement of electrons from the semiconductor's conduction

band to the metal. This will cause the barrier height, ϕ_B , to be very small. A similar effect is observed when the Fermi-level of the metal is higher than that of the semiconductor, this results in the band-bending, seen in Figure 3.2c, to be downwards. This means that electrons do not encounter a barrier. Contacts of this type are known as *ohmic contacts*. A more detailed description of the formation and criteria for ohmic contacts is given by Rhoderick and Williams (1988) who also offer an excellent overview on the concepts relating to Schottky barriers.

3.3 THE TUNNELLING CURRENT

In order to understand the behaviour of a Cold Electron Bolometer it is important to understand the movement of charges, at different energies, across the tunnelling barrier. To do this we need to consider four directions of charge transfer, these are¹:

1. Charges in the superconductor with energies above the superconducting bandgap ($E > E_{f_S} + \Delta$) tunnelling into the central, semiconductor, island.
- add glossary entry 2. Quasiparticles in the superconductor whose energies are below the Fermi-energy ($E < E_{f_S} - \Delta$) tunnelling into the central island.
3. Charges in the central island with energy levels corresponding to the normal states in the superconductor ($E > E_{f_S} + \Delta$).
4. Charges in the central island with energies below corresponding to the superconducting states in the superconductor ($E < E_{f_S} - \Delta$).

Since the movement of charges in terms 3 and 4 is the opposite of those in the first two terms these act to suppress the total current.

Figure 3.3 shows these four possible forms of tunnelling when there is no bias across the structure. It can be seen that the tunnelling routes represented by numbers 1 and 3 are possible (providing there is sufficient thermal broadening of the density of states) since there are charges and vacant states on both sides of the Schottky barrier. The tunnelling shown by numbers 2 and 4 are less likely since there are very few vacant states for electrons to tunnel to.

¹In the following list E_{f_S} is used to denote the Fermi-energy in the superconductor.

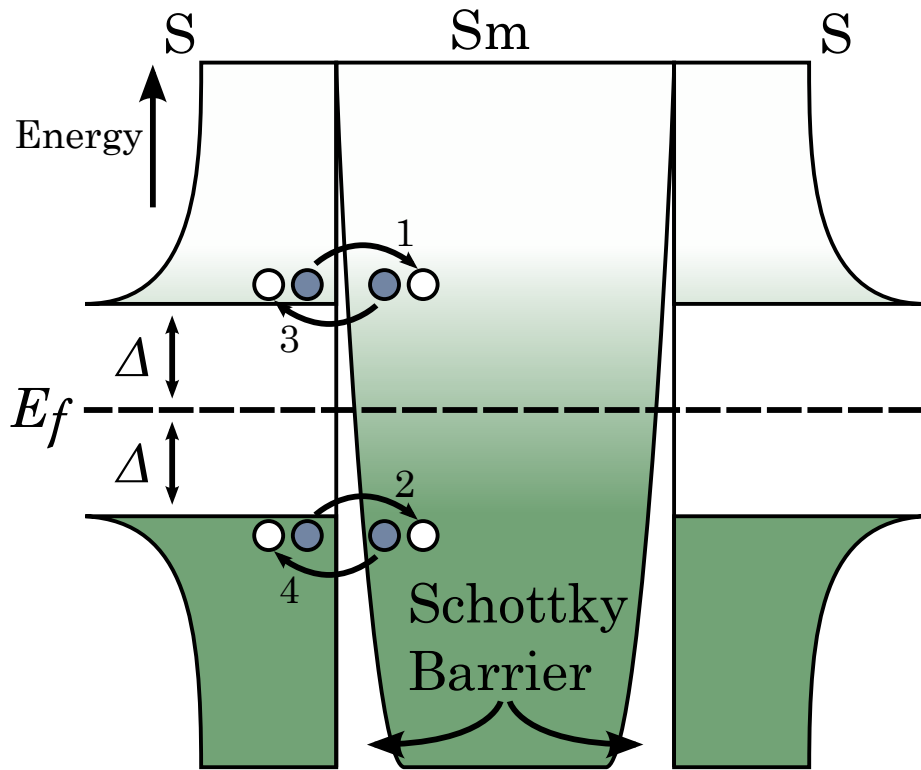


Figure 3.3: Possible tunnelling of charges in a SSmS structure, shown at non-zero temperature, without any external bias across this system and for only one junction. The density of the shading represents the number of occupied states (no shading - all states are vacant; fully shaded - all states are vacant) There are four different ways in which charges can tunnel across the structure (numbering as listed on Page 16).

By applying an external bias across the structure it is possible to shift the distribution of charges in the three layers relative to each other. This biasing causes the probability of tunnelling, via each of the routes to be altered. Figure 3.4 shows the effect of biasing a single junction structure such that the energy levels in the semiconductor (right) are raised above the energy levels in the superconductor (left). This has a notable effect to the probability of tunnelling via each of the described routes. Charges are less likely tunnel from superconductor into the semiconductor (routes one and two), since there are fewer states available in

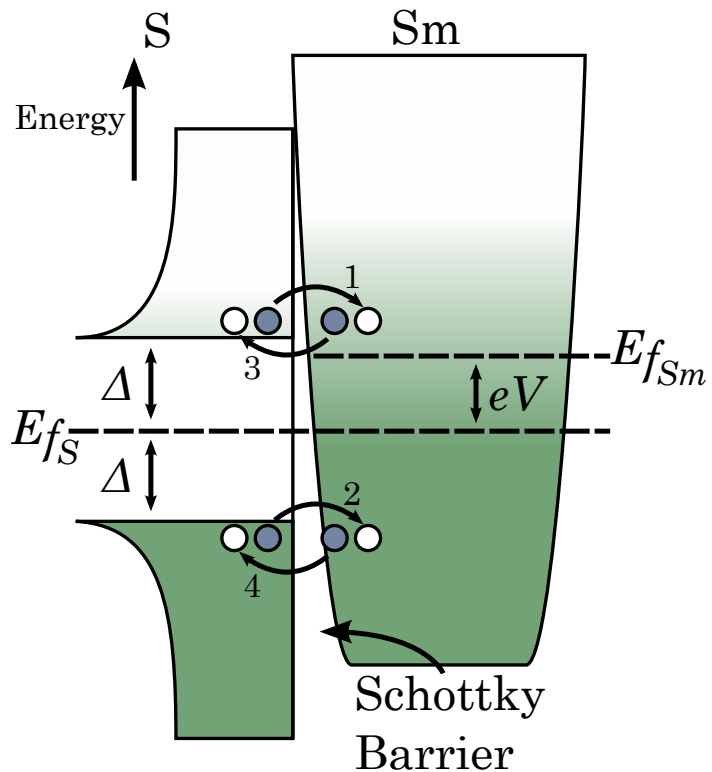


Figure 3.4: Tunnelling of charges across a single superconductor-semiconductor junction when biased by a voltage, V , such the Fermi level in the semiconductor, E_{fSm} , is raised above that of the superconductor, E_{fS} .

the semiconductor at energies corresponding to the occupied in the superconductor. Conversely, charges are more likely to move from the semiconductor into the superconductor (routes three and four) as there are a greater number of occupied states in the semiconductor with energies corresponding to the vacant states in the superconductor.

Figure 3.5 illustrates a single junction system biased in the opposite polarity to the structure shown in Figure 3.4. In this case, when compared to the unbiased state, charges are more likely to tunnel from the superconductor into the semiconductor (routes one and two) since the occupied states in the superconductor correspond to a greater number of vacant states in the semiconductor. Likewise, fewer charges will tunnel from the semiconductor into the superconductor (routes

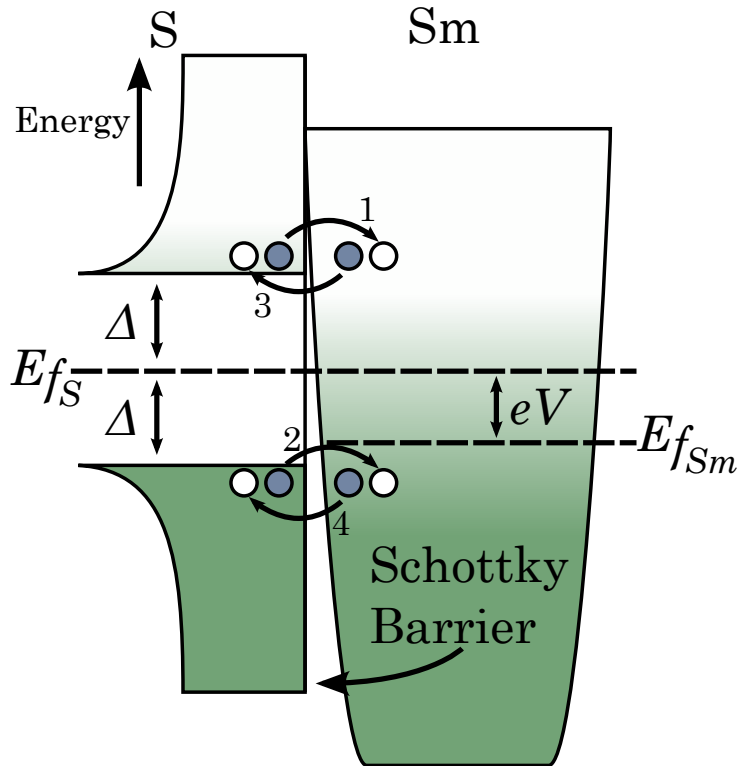


Figure 3.5: Tunnelling of charges across a single superconductor-semiconductor junction when biased in the opposite polarity to that shown in Figure 3.4. The biasing voltage, V , causes the Fermi level in the superconductor, E_{fS} , to be raised above the Fermi level in the semiconductor, E_{fSm} .

three and four) as there are fewer occupied states in the semiconductor aligned with vacant states in the superconductor.

When modelling the current in a two junction system it is useful to note that, since the two junctions can be thought of as resistors in series, we need only consider the current through one junction, since the current through each of the junction will be the same. This brings up two important definitions in the following derivation: the voltage used in these equations is defined to be the voltage dropped across a two junction system. The following equations assume there is no resistance to current flow from either the semiconductor or superconductor hence the voltage dropped across each junction will be $V/2$. The second definition to note is

that the tunnelling resistance, R_N , is defined to be the resistance of a single junction.

For each of these movements of charge it is possible to define a Fermi-distribution, q_n where the subscript n corresponds to the number of the term in the list on Page 16.

$$q_1 \sim \frac{1}{e^{\frac{|E|}{k_B T_S}} + 1}, \quad (3.1)$$

$$q_2 \sim \frac{1}{e^{\frac{-|E|}{k_B T_S}} + 1}, \quad (3.2)$$

$$q_3 \sim \frac{1}{e^{\frac{(|E|+eV/2)}{k_B T_e}} + 1}, \quad (3.3)$$

$$q_4 \sim \frac{1}{e^{\frac{-(|E|-eV/2)}{k_B T_e}} + 1}. \quad (3.4)$$

In these equations E is the energy of a carrier, k_B is Boltzmann's constant, T_S and T_e are the temperatures of the charge carries in the superconductor and the central island respectively, e is the electron charge and V is the voltage across structure. q_1 is the Fermi-distribution for charges in the superconductor with energy above the superconducting bandgap, q_2 relates to charges in the superconductor with energies below the bandgap, q_3 and q_4 are the distributions of charges in the central island with energies above and below the superconductor's bandgap respectively.

For each of the terms in the above list we can define a probability p_{1-4} that a charge will tunnel in the stated manner. This probability is related to the likelihood of an occupied state on one side of the tunnelling barrier corresponding to an empty state on the other side. For each of the forms of tunnelling defined above, this probability is:

$$p_1 = q_1 \times (1 - q_3), \quad (3.5)$$

$$p_2 = q_2 \times (1 - q_4), \quad (3.6)$$

$$p_3 = q_3 \times (1 - q_1), \quad (3.7)$$

$$p_4 = q_4 \times (1 - q_2). \quad (3.8)$$

The total movement of charges between the superconductor and the superconducting contact is related to the sum of these probabilities integrated over all

energies and, if movement from the superconductor to the semiconductor is taken to be the positive direction, is given by:

$$p_T = \int_0^\infty [p_1 + p_2 - p_3 - p_4] dE. \quad (3.9)$$

Substituting the terms for p_{1-4} from Equations 3.5–3.8 gives:

$$p_T = \int_{-\infty}^\infty [q_1 \times (1 - q_3) + q_2 \times (1 - q_4) - q_3 \times (1 - q_1) - q_4 \times (1 - q_2)] dE. \quad (3.10)$$

Expanding the bracket and cancelling the like terms yields:

$$p_T = \int_{-\infty}^\infty [q_1 - q_1 q_3 + q_2 - q_2 q_4 - q_3 + q_3 q_1 - q_4 + q_4 q_2] dE, \quad (3.11)$$

$$p_T = \int_{-\infty}^\infty [q_1 + q_2 - q_3 - q_4] dE. \quad (3.12)$$

It is possible to simplify this result further by looking at the sum of various combinations of the q terms in Equation 3.12. Of most interest is the result of $q_1 + q_2$.

$$q_1 + q_2 = \frac{1}{e^{\frac{|E|}{k_B T_S}} + 1} + \frac{1}{e^{\frac{-|E|}{k_B T_S}} + 1}, \quad (3.13)$$

$$= \frac{e^{\frac{-|E|}{k_B T_S}} + 1 + e^{\frac{|E|}{k_B T_S}} + 1}{\left(e^{\frac{|E|}{k_B T_S}} + 1\right) \times \left(e^{\frac{-|E|}{k_B T_S}} + 1\right)}, \quad (3.14)$$

$$= \frac{e^{\frac{|E|}{k_B T_S}} + e^{\frac{-|E|}{k_B T_S}} + 2}{e^{\frac{|E|}{k_B T_S}} e^{\frac{-|E|}{k_B T_S}} + e^{\frac{|E|}{k_B T_S}} + e^{\frac{-|E|}{k_B T_S}} + 1}, \quad (3.15)$$

$$q_1 + q_2 = 1. \quad (3.16)$$

A useful result can also be found from examining the result of sum $q_1 + q_2 - q_3$ and using the result of Equation 3.16 above.

$$q_1 + q_2 - q_3 = 1 - q_3, \quad (3.17)$$

$$= 1 - \frac{1}{e^{\frac{|E|+eV/2}{k_B T_e}} + 1}, \quad (3.18)$$

$$= \frac{e^{\frac{|E|+eV/2}{k_B T_e}}}{e^{\frac{|E|+eV/2}{k_B T_e}} + 1}, \quad (3.19)$$

$$= \frac{1}{e^{-\frac{|E|+eV/2}{k_B T_e}} \left(e^{\frac{|E|+eV/2}{k_B T_e}} + 1 \right)}, \quad (3.20)$$

$$q_1 + q_2 - q_3 = \frac{1}{e^{\frac{-(|E|+eV/2)}{k_B T_e}} + 1}. \quad (3.21)$$

Substituting this result into Equation 3.12 gives:

$$p_T = \int_{-\infty}^{\infty} [q_1 + q_2 - q_3 - q_4] dE, \quad (3.12 \text{ revisited})$$

$$= \int_{-\infty}^{\infty} \left[\frac{1}{e^{\frac{-(|E|+eV/2)}{k_B T_e}} + 1} - q_4 \right] dE, \quad (3.22)$$

$$= \int_{-\infty}^{\infty} \left[\frac{1}{e^{\frac{-(|E|+eV/2)}{k_B T_e}} + 1} - \frac{1}{e^{\frac{-(|E|-eV/2)}{k_B T_e}} + 1} \right] dE, \quad (3.23)$$

$$p_T = \int_{-\infty}^{\infty} \left[\frac{1}{e^{\frac{(|E|-eV/2)}{k_B T_e}} + 1} - \frac{1}{e^{\frac{(|E|+eV/2)}{k_B T_e}} + 1} \right] dE. \quad (3.24)$$

The total number of charges tunnelling can be found by multiplying this probability by the density of states in the superconductor $N_S(E)$ which, from Bardeen, Cooper, and Schrieffer (1957), is given by:

$$N_S(S) = \frac{E}{\sqrt{E^2 - \Delta^2}}, \quad (3.25)$$

where Δ is half the size of the superconducting energy gap. The energy gap is a function of the electron temperature, increasing from zero just above the superconducting critical temperature, T_c , to a maximum value of $1.764/k_B T_c$ at 0 K. The size of the energy gap with decreasing temperature is shown in Figure 3.6.

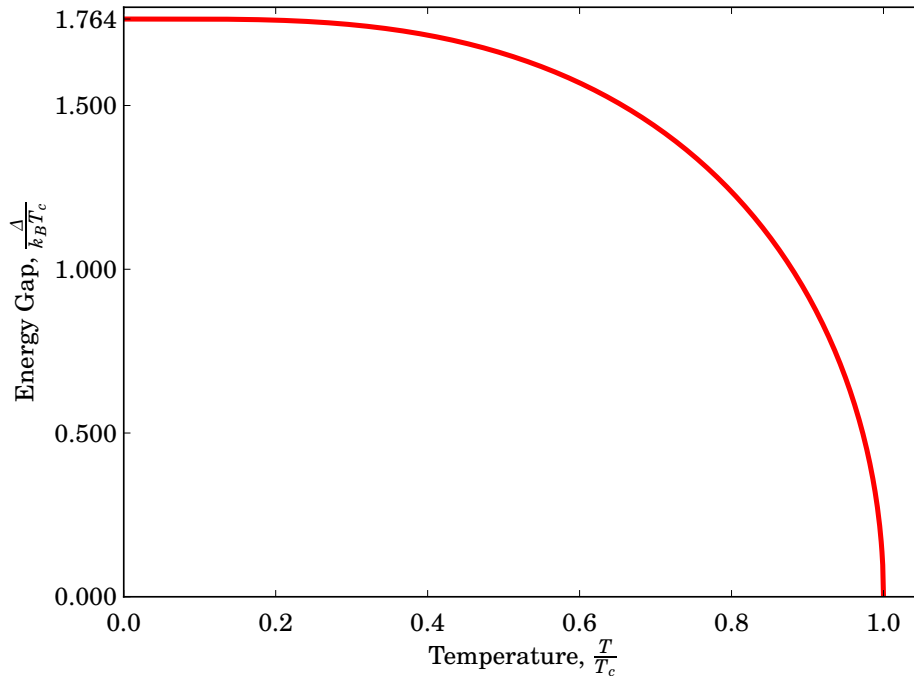


Figure 3.6: Increase in the superconducting energy gap with decreasing temperature as described by Bardeen, Cooper, and Schrieffer (1957).

Using Equation 3.25 in the result from Equation 3.24 gives the total number of charges, n , tunnelling across the barrier:

$$n = \int_{-\infty}^{\infty} \frac{|E|}{\sqrt{|E|^2 - \Delta^2}} \left[\frac{1}{e^{\frac{(|E|-eV/2)}{k_B T_e}} + 1} - \frac{1}{e^{\frac{(|E|+eV/2)}{k_B T_e}} + 1} \right] dE. \quad (3.26)$$

Finally it is possible to convert this number of charges in to a tunnelling current, I , by converting Equation 3.26 to a voltage by dividing by the electron charge, e , and using Ohm's Law with the tunnelling resistance R_N .²

$$I = \frac{1}{eR_N} n. \quad (3.27)$$

²The subscript N denotes that this is the *normal state* resistance of an current-voltage (IV) curve.

Maybe rewrite equation with $R_N/2$

Which, after substituting the term for n from Equation 3.26 gives the final result:

$$I = \frac{1}{eR_N} \int_{-\infty}^{\infty} \frac{E}{\sqrt{E^2 - \Delta^2}} \left[\frac{1}{e^{\frac{(E-eV/2)}{k_B T_e}} + 1} - \frac{1}{e^{\frac{(E+eV/2)}{k_B T_e}} + 1} \right] dE. \quad (3.28)$$

Using this result, and if the current and the voltage of a particular device have been measured it is possible to use a parameter fitting program to calculate the electron temperature.

Inspection of Equation 3.28 shows that there is an exponential dependence on the electron temperature for the tunnelling current. It is this dependency which makes the tunnelling contacts described here high sensitive thermometers. The relationship between the electron temperature and the tunnelling current (at a constant voltage bias) is shown in Figure 3.7. The tunnelling current increases rapidly with the electron temperature until the temperature of the electrons is greater than the critical temperature; at which point the tunnelling current remains constant.

3.4 THE COOLING POWER

Each time a charge leaves the central island by tunnelling into one of the superconducting contacts, as described in Section 3.3, it must be replaced by a charge from one of the superconducting contacts. When the device is biased the most likely flow of charge will be from the semiconductor into the lower energy contact ($E_{fs} - E_{fsm} = -eV/2$) and for a charge from the superconductor at a higher energy ($E_{fs} - E_{fsm} = eV/2$) to fill this vacant state. This is illustrated in Figure 3.8. Since the charges which tunnel out are replaced by less energetic charges the overall energy (and thus temperature) of the charges in the central island is reduced. It is this process which is utilised to create the microrefrigerator type of device (Nahum, Eiles, and Martinis, 1994).

This cooling of charges in the central island of the structure can be expressed as a cooling or heating power, P , depending on the exact route by which charges pass through the structure this term will either be positive, meaning that energy is added to the semiconductor and there is net heating; or it will be negative, due to energy being removed and the temperature of the charges is lowered.

To derive an expression for this power it is possible to follow a similar derivation to that given in Section 3.3 to find the tunnelling current (Equation 3.28).

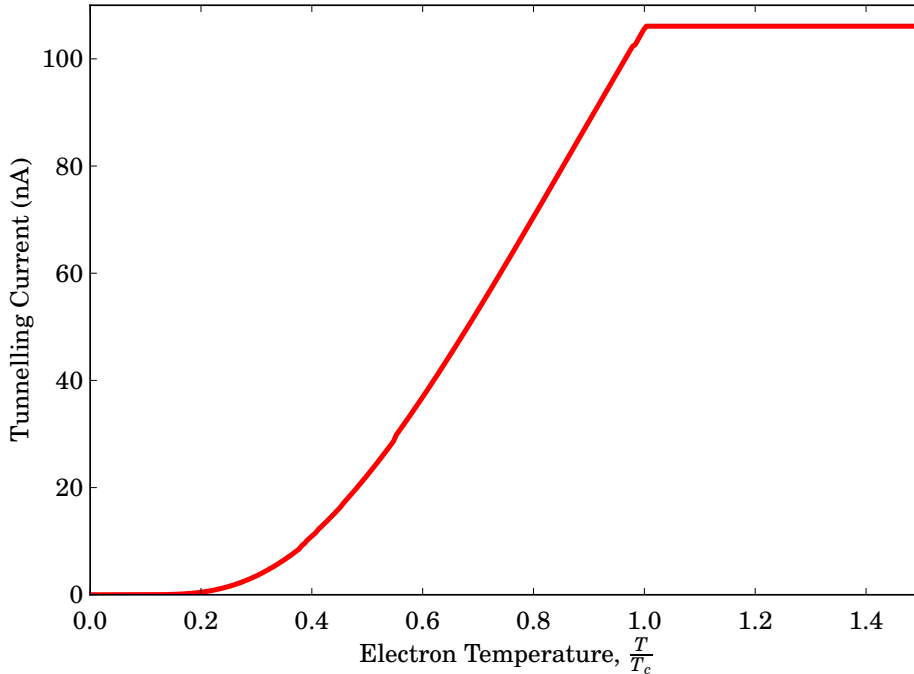


Figure 3.7: The relationship between the tunnelling current and the electron temperature. This was modelled using Equation 3.28 for a superconductor with a critical temperature of 1.2 K, biased by a voltage $V = \Delta_{T=0}$ and a tunnelling resistance, per junction, of $1 \text{ k}\Omega$.

To do this the probability, p_T , of an occupied state on one side of the barrier corresponding to a vacant state on the other is again calculated. There are four possible routes by which charges can tunnel to or from the semiconductor. These were illustrated in Figures 3.3, 3.4 and 3.5. In order to calculate the total energy added to the semiconductor each of these probabilities needs to be multiplied by the energy of the charges tunnelling.

p_1 transfers charges with energy $E + eV/2$ from the superconducting contact into the semiconductor.

p_2 transfers charges with energy $-(E - eV/2)$ from the superconductor into the semiconductor.

p_3 removes charges with energy $E + eV/2$ from the central semiconductor, this

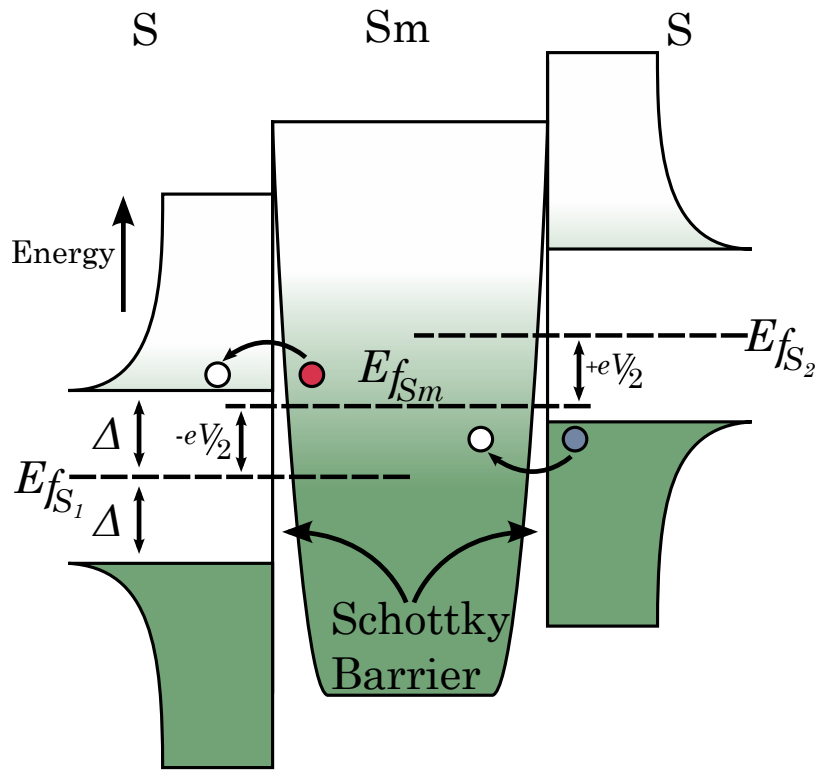


Figure 3.8: The most likely route for charges to tunnel in a biased two junction system. If the system is biased such that the energy levels in the left hand superconductor are lowered with respect the semiconductor and the states in the right hand contact are raised (as shown), the most likely movement of charges from the semiconductor will be for charges in the superconductor with energies corresponding to just above the energy gap in the left hand left hand superconductor to tunnel in to the left hand superconductor. This will create a vacant state which will be filled by a charge at the top of the superconducting state in the right hand superconductor.

means the energy contribution to the semiconductor is $-(E + eV/2)$.

p_4 removes charges with energy $-(E - eV/2)$ from the semiconductor, this results in an energy change of $E - eV/2$ in the semiconductor.

To find the total energy transferred through this tunnelling the summation of

these terms needs to be integrated over all energies and multiplied by the superconducting density of states, given by:

$$N_S(S) = \frac{E}{\sqrt{E^2 - \Delta^2}}, \quad (3.25 \text{ revisited})$$

This gives:

$$E = \int_{-\infty}^{\infty} \frac{E}{\sqrt{E^2 - \Delta^2}} \left[E(p_1 - p_2 - p_3 + p_4) + \frac{eV}{2}(p_1 + p_2 - p_3 - p_4) \right] dE. \quad (3.29)$$

One important definition which can be taken from this is that the change in energy, due movement of charges, is defined such that an increase in this term corresponds to the overall energy of the changes in the semiconductor increasing (i.e. heating of the charges).

To calculate the power, P , associated with this change in energy Equation 3.29 needs to be divide by the tunnelling resistance, R_N , (as defined on 23) and the square of the electron charge. This additional electron charge is the result of multiplying by the energy of the carries in Equation 3.29 as opposed to the charge of the carriers in Equation 3.26. One further observation needs to be made prior to arriving at a term for the tunnelling power. When deriving Equation 3.28 for the tunnelling current it sufficed to examine only a single junction. This was due to the fact that since the two junctions are in a series configuration the current through the two must be the same. In the case of the tunnelling power heat can flow through either of the two junctions, this means that for symmetrical junctions Equation 3.29 needs to be further multiplied by a factor of two. This gives:

$$P = \frac{2}{e^2 R_N} \int_{-\infty}^{\infty} \frac{E}{\sqrt{E^2 - \Delta^2}} \left[E(p_1 - p_2 - p_3 + p_4) + \frac{eV}{2}(p_1 + p_2 - p_3 - p_4) \right] dE. \quad (3.30)$$

It is useful to split this in two terms, P_1 and P_2 , such that:

$$P_1 = \frac{2}{e^2 R_N} \int_{-\infty}^{\infty} \frac{E}{\sqrt{E^2 - \Delta^2}} [E(p_1 - p_2 - p_3 + p_4)] dE, \quad (3.31)$$

$$P_2 = \frac{2}{e^2 R_N} \int_{-\infty}^{\infty} \frac{E}{\sqrt{E^2 - \Delta^2}} \left[\frac{eV}{2} (p_1 + p_2 - p_3 - p_4) \right] dE, \quad (3.32)$$

$$P = P_1 + P_2. \quad (3.33)$$

Equation 3.32 for P_2 can be rewritten as:

$$\begin{aligned} P_2 &= \frac{eV}{2} \frac{2}{e^2 R_N} \int_{-\infty}^{\infty} \frac{E}{\sqrt{E^2 - \Delta^2}} (p_1 + p_2 - p_3 - p_4) dE, \\ P_2 &= V \frac{1}{eR_N} \int_{-\infty}^{\infty} \frac{E}{\sqrt{E^2 - \Delta^2}} (p_1 + p_2 - p_3 - p_4) dE. \end{aligned} \quad (3.34)$$

By noting that tunnelling current, I , can be rewritten as:

$$I = \frac{1}{eR_N} \int_{-\infty}^{\infty} \frac{E}{\sqrt{E^2 + \Delta^2}} [p_1 + p_2 - p_3 - p_4] dE, \quad (3.28 \text{ rewritten})$$

and comparing this to Equation 3.34 it can be seen that the latter can be simply written as:

$$P_2 = IV. \quad (3.35)$$

It is possible to slightly simplify Equation 3.31, in a way similar to that performed to simplify Equation 3.9 to Equation 3.24 in Section 3.3. This starts by recalling that p_{1-4} can be written as:

$$p_1 = q_1 \times (1 - q_3), \quad (3.5 \text{ revisited})$$

$$p_2 = q_2 \times (1 - q_4), \quad (3.6 \text{ revisited})$$

$$p_3 = q_3 \times (1 - q_1), \quad (3.7 \text{ revisited})$$

$$p_4 = q_4 \times (1 - q_2). \quad (3.8 \text{ revisited})$$

Thus, the term in square brackets in Equation 3.31 (which for the sake of tidiness we will temporarily call A) can be written as:

$$A = E(p_1 - p_2 - p_3 + p_4), \quad (3.36)$$

$$\therefore P_1 = \frac{2}{e^2 R_N} \int_{-\infty}^{\infty} \frac{E}{\sqrt{E^2 - \Delta^2}} \times A dE, \quad (3.37)$$

$$A = E(q_1 \times (1 - q_3) - q_2 \times (1 - q_4) - q_3 \times (1 - q_1) + q_4 \times (1 - q_2)). \quad (3.38)$$

Multiplying out these terms gives:

$$A = E(q_1 - q_1 q_3 - q_2 + q_2 q_4 - q_3 + q_3 q_1 + q_4 - q_4 q_2), \quad (3.39)$$

$$A = E(q_1 - q_2 - q_3 + q_4). \quad (3.40)$$

This gives:

$$P_1 = \frac{2}{e^2 R_N} \int_{-\infty}^{\infty} \frac{E}{\sqrt{E^2 - \Delta^2}} [E(q_1 - q_2 - q_3 + q_4)] dE. \quad (3.41)$$

Since it is not possible to further simplify this, the final form of P_1 can be written as:

$$P_1 = \frac{2}{e^2 R_N} \int_{-\infty}^{\infty} \frac{E^2}{\sqrt{E^2 - \Delta^2}} \left[\frac{1}{e^{\frac{E}{k_B T_S}} + 1} - \frac{1}{e^{\frac{-E}{k_B T_S}} + 1} - \frac{1}{e^{\frac{(E+eV/2)}{k_B T_e}} + 1} + \frac{1}{e^{\frac{-(E-eV/2)}{k_B T_e}} + 1} \right] dE. \quad (3.42)$$

Using this result, along with that of Equation 3.35, in Equation 3.33 gives the final result of the tunnelling power as:

$$P = IV + \frac{2}{e^2 R_N} \int_{-\infty}^{\infty} \frac{E^2}{\sqrt{E^2 - \Delta^2}} \left[\frac{1}{e^{\frac{E}{k_B T_S}} + 1} - \frac{1}{e^{\frac{-E}{k_B T_S}} + 1} - \frac{1}{e^{\frac{(E+eV/2)}{k_B T_e}} + 1} + \frac{1}{e^{\frac{-(E-eV/2)}{k_B T_e}} + 1} \right] dE. \quad (3.43)$$

3.5 THE RESPONSIVITY

Like all bolometric detectors it is possible to bias a Cold Electron Bolometer with either a voltage or a current. In either case the quantity which is not providing the bias is monitored and it is in this signal that the response to a change in incident optical power will be measured. The responsivity, S , of a detector is defined as the ratio of the change in the measured signal to the change in the power absorbed in the detector. This is written as:

$$S = \frac{d\text{signal}}{dP_{abs}}, \quad (3.44)$$

where *signal* is the quantity being monitored and P_{abs} is the absorbed power. Since a bolometric detector is biased by either a voltage or a current we can define two types of responsivity. In the case of a voltage biased detector, where the current flowing through the detector is monitored, the current responsivity, S_I , is given by:

$$S_I = \frac{dI}{dP_{abs}}, \quad (3.45)$$

where I is the current being measured. For a detector biased by a current, the voltage responsivity, S_V is given by:

$$S_V = \frac{dV}{dP_{abs}}, \quad (3.46)$$

where V is the measured voltage.

These terms are general expressions and need to be rewritten such that their values can be calculated. In order to derive useful expressions for the responsivity it is important to understand the relative contributions to the heating (or cooling) of the electrons in the detector's absorber. Along with tunnelling power (Equation 3.43) which adds or removed heat via the tunnelling current the electrons in the absorber are also affected by various other sources of heating or cooling. The most significant of which are: Joule heating, P_J , due the resistance experienced by the current within the absorber; the energy from radiative source which is absorbed by the detector, P_{abs} ; and the flow of energy directly between the electron and the phonon systems, P_{e-ph} . Joule heating was first described by Joule (1837), it is caused the collisions between the charges flowing in the current and

the atomic ions in the conductor. The heating power from these collisions is given by:

$$P_J = I^2 R, \quad (3.47)$$

where I is the current flowing through a resistance R .

Unless the electron and phonon systems are at thermal equilibrium there will be a flow of heat between the two due to the thermal link between the systems. The heating (or cooling) power resulting from this flow of heat is given by:

$$P_{e-ph} = \Sigma \Omega \left(T_e^\beta - T_{ph}^\beta \right), \quad (3.48)$$

where Σ is a material constant relating to how strong the thermal link between the electrons and phonons is, Ω is the volume in which the electrons and phonons are not in thermal equilibrium, T_e and T_{ph} are the temperatures of the electrons and the phonons respectively, and β is the power dependance on the temperature of the heat flow. Unlike all of the other terms mentioned (including the tunnelling power) this term is positive for the removal of energy (cooling) from the electrons and negative for heating of the electrons.

For the absorber to be at a constant temperature these terms must add up to zero. This is referred to as the heat balance equation (or the heat balance condition) and can be expressed as:

$$P + P_{abs} + P_J - P_{e-ph} = 0, \quad (3.49)$$

where P is the tunnelling power given in Equation 3.43, P_{abs} is the power absorbed in the detector due to incident optical power, I is the current flowing through the absorber of the detector, R_{abs} is the resistance of the detector's absorber, Σ is the material constant of the absorber, Ω is the volume of the absorber, T_e and T_{ph} are the temperatures of the electrons and phonons respectively and β is the power of temperature dependency of electron-phonon cooling power, this has been found by Prest et al. (2011) to be 6. This equation is simply the equilibrium condition for temperature of the electrons in the absorber, the first three terms are defined as being positive for heating of the electrons whereas the final term is defined as being positive for cooling of the charges. The meaning of the first two terms has already been covered, the third term is simply the Joule heating of the electrons in the absorber due to the current flowing through the absorber; the final term is the

cooling of the electrons due to their thermal link to the phonons, this is positive when the temperature of the phonons is less than that of the electrons and is thus a heating power as opposed to a cooling power.

In the case of a voltage biased detector the current responsivity, S_I , can be derived by noting that Equation 3.45 can be rewritten as:

$$S_I = \frac{dI}{dP_{abs}} = \frac{\frac{\partial I}{\partial T_e}}{\frac{\partial P_{abs}}{\partial T_e}}. \quad (3.50)$$

The denominator of this can be found by differentiating the heat balance equation (Equation 3.49).

$$0 = \frac{\partial P}{\partial T_e} + \frac{\partial P_{abs}}{\partial T_e} + \frac{\partial}{\partial T_e} I^2 R_{abs} - \beta \Sigma \Omega T_e^{\beta-1}, \quad (3.51)$$

$$\frac{\partial P_{abs}}{\partial T_e} = \beta \Sigma \Omega T_e^{\beta-1} - \frac{\partial P}{\partial T_e} - \frac{\partial}{\partial T_e} I^2 R_{abs}. \quad (3.52)$$

Substituting this result into Equation 3.50 gives the final result:

$$S_I = \frac{\frac{\partial I}{\partial T_e}}{\beta \Sigma \Omega T_e^{\beta-1} - \frac{\partial P}{\partial T_e} - \frac{\partial}{\partial T_e} I^2 R_{abs}}. \quad (3.53)$$

This differs slightly from Equation 10 of Golubev and Kuzmin (2001) who do not consider the Joule heating of the absorber in their model but who do consider the effects of operating in an AC regime³.

It is possible to derive the voltage responsivity, S_V , similarly by starting with:

$$S_V = \frac{dV}{dP_{abs}} = \frac{\frac{\partial V}{\partial T_e}}{\frac{\partial P_{abs}}{\partial T_e}}. \quad (3.54)$$

Since in the current biased case the current across the detector cannot change it is possible to write:

$$\frac{dI}{dT_e} = 0 = \frac{\partial I}{\partial V} \frac{\partial V}{\partial T_e} + \frac{\partial I}{\partial T_e}, \quad (3.55)$$

$$\frac{\partial V}{\partial T_e} = \frac{-\frac{\partial I}{\partial T_e}}{\frac{\partial I}{\partial V}}. \quad (3.56)$$

³Also note that Golubev and Kuzmin define the tunnelling power to be positive for cooling of the electrons.

Using this in the numerator of Equation 3.54 yields:

$$S_V = \frac{\frac{-\frac{\partial I}{\partial T_e}}{\frac{\partial I}{\partial V}}}{\frac{\partial P_{abs}}{\partial T_e}}. \quad (3.57)$$

As in the case for the current responsivity, the numerator can be found by differentiating the heat balance equation. In the current biased case there are two subtle difference to that of Equation 3.52. This first is that the Joule heating term no longer depends on the electron temperature since the current is constant and thus:

$$\left(\frac{\partial}{\partial T_e} I^2 R_{abs} \right)_I = 0. \quad (3.58)$$

The second is the that the tunnelling power (given by Equation 3.43) is a function of both the electron temperature and the voltage (along with the temperature of the charges in the superconductor). In the voltage biased case the voltage was not a function of the electron temperature. In the current bias case since the current is fixed the voltage across the tunnelling contacts must vary with the temperature of the charges, this means that:

$$\frac{dP}{dT_e} = \frac{\partial P}{\partial V} \frac{\partial V}{\partial T_e} + \frac{\partial P}{\partial T_e}. \quad (3.59)$$

Substituting the result of Equation 3.56 gives:

$$\frac{dP}{dT_e} = \frac{\partial P}{\partial T_e} - \frac{\frac{\partial I}{\partial T_e}}{\frac{\partial I}{\partial V}} \frac{\partial P}{\partial V}. \quad (3.60)$$

Noting this along with the differential of the Joule heating power from Equation 3.58 the differential of the heat balance equation is now:

$$0 = \frac{\partial P_{abs}}{\partial T_e} + \frac{\partial P}{\partial T_e} - \frac{\frac{\partial I}{\partial T_e}}{\frac{\partial I}{\partial V}} \frac{\partial P}{\partial V} - \beta \Sigma \Omega T_e^{\beta-1}, \quad (3.61)$$

giving:

$$\frac{\partial P_{abs}}{\partial T_e} = \beta \Sigma \Omega T_e^{\beta-1} + \frac{\frac{\partial I}{\partial T_e}}{\frac{\partial I}{\partial V}} \frac{\partial P}{\partial V} - \frac{\partial P}{\partial T_e}. \quad (3.62)$$

Substituting this for the denominator of Equation 3.57 gives the final form of the voltage responsivity to be:

$$S_V = \frac{\frac{-\frac{\partial I}{\partial T_e}}{\frac{\partial I}{\partial V}}}{\beta \Sigma \Omega T_e^{\beta-1} + \frac{\frac{\partial I}{\partial T_e}}{\frac{\partial I}{\partial V}} \frac{\partial P}{\partial V} - \frac{\partial P}{\partial T_e}}. \quad (3.63)$$

This is the same, in the DC limit, as Golubev and Kuzmin (Equation 30 of 2001).

3.6 THE SOURCES OF ELECTRICAL NOISE

In order for incoming optical radiation to be measured by a detector system the output signal produced must be greater than the noise signal of the detector or the readout system used. This means that a detector with a high level of inherent noise is less sensitive than a detector with lower level of noise. When developing a detector there are two main goals. The first is to prove that the underlying principles are in fact valid and that a functioning detector can be made. The second is to make the detector as sensitive as possible⁴. Because of this it is important to have a strong understanding of the noise processes involved in a detector.

There are several physical phenomena that cause noise. These can be roughly grouped into two categories: noise due to some form of fluctuation and noise resulting from the contamination of one signal by another. It is usually possible to shield electrical wiring and components to eliminate contamination of a signal however some sources may be more problematic to remove; for example 50 Hz or *mains noise* is caused by the switching AC voltage used to power electrical equipment, since it is most likely essential to use some form of mains powered equipment to monitor a detector this noise may be more problematic to remove. Noise due to fluctuations in the energy of the charges within the detector are inevitable and can, at best, only be partially reduced through cleverly designing the detector or the materials used.

In deriving a term for the expected noise measured for a Silicon Cold Electron Bolometer three types of noise will be considered: Firstly, internal noise within the detector, these terms are due to various internal factors which cause the energy of the charges to fluctuate. Secondly, noise which is the result of incident power

⁴It is worth mentioning that, depending upon the desired application for a detector, improvements to the detector's speed may be as desirable (or even more so) as improved sensitivity.

absorbed by the device. Finally, amplifier or readout noise which is added to the signal by the electronic systems used to monitor the detector.

For the internal noise two contributions will be considered, these are the current noise $\langle \delta I \rangle$ and the power or heat flow noise $\langle \delta P \rangle$. As can be seen from Section 3.4 (and particularly Equation 3.43) these two quantities are not uncorrelated, indeed the tunnelling power depends heavily on the current (as one might expect). To address this correlation of the two quantities a third term, the correlated noise, $\langle \delta P \delta I \rangle$, is introduced.

For these terms the fluctuations that cause the corresponding noise will be taken to be governed by Poisson statistics, meaning that:

$$\sigma_x = \sqrt{\bar{x}}, \quad (3.64)$$

where σ_x is the standard deviation of the quantity x and \bar{x} is the mean value of x .

In the case of the current noise, the generated noise is due to the fluctuations in the number of electrons tunnelling across the Schottky contacts. The total number of charges, n , tunnelling (in any direction) for a two junction system is given by:

$$n = 2 \int_{-\infty}^{\infty} \frac{E}{\sqrt{E^2 - \Delta^2}} [p_1 + p_2 + p_3 + p_4] dE, \quad (3.65)$$

where p_{1-4} are the terms defined on Page 20, the factor of two comes from the fact that charges can tunnel through two junctions. This can be converted to a total noise current, I_N by dividing by the electron charge and the tunnelling resistance to give:

$$I_N = \frac{2}{eR_N} \int_{-\infty}^{\infty} \frac{E}{\sqrt{E^2 - \Delta^2}} [p_1 + p_2 + p_3 + p_4] dE. \quad (3.66)$$

Schottky (1918) provides the general formula for the shot noise due to the flow of current to be:

$$\langle \delta I \rangle = \sqrt{2eI}. \quad (3.67)$$

Substituting the noise current from Equation 3.66 gives the final equation for the shot noise due to current flow to be:

$$\langle \delta I^2 \rangle = \frac{4}{R_N} \int_{-\infty}^{\infty} \frac{E}{\sqrt{E^2 - \Delta^2}} [p_1 + p_2 + p_3 + p_4] dE, \quad (3.68)$$

Add glossary entry: Amplifier Noise

or more completely:

$$\langle \delta I^2 \rangle = \frac{4}{R_N} \int_{-\infty}^{\infty} \frac{E}{\sqrt{E^2 - \Delta^2}} \left[\frac{1}{e^{\frac{E}{k_B T_S}} + 1} + \frac{1}{e^{\frac{-E}{k_B T_S}} + 1} + \frac{1}{e^{\frac{(E+eV/2)}{k_B T_e}} + 1} \right. \\ \left. + \frac{1}{e^{\frac{-(E-eV/2)}{k_B T_e}} + 1} - 2 \frac{1}{e^{\frac{E}{k_B T_S}} + 1} \frac{1}{e^{\frac{(E+eV/2)}{k_B T_e}} + 1} \right. \\ \left. - 2 \frac{1}{e^{\frac{-E}{k_B T_S}} + 1} \frac{1}{e^{\frac{-(E-eV/2)}{k_B T_e}} + 1} \right] dE. \quad (3.69)$$

The noise due the flow of heat, either into or from the semiconducting absorber, is derived similarly. As was the case when deriving Equation 3.43 for the tunnelling power, the power noise is essentially the current noise multiplied by the energy of the charges tunnelling. Each of the routes shown in Figure 3.3 contributes a different amount of energy to the semiconductor.

As previously covered on Page 25 of Section 3.4, each of the tunnelling routes (shown on Page 17) contributes a different amount of energy (per charge tunnelling) to the semiconductor. To recap the energy change in the semiconductor due to each of the four routes is:

- Route 1 causes an energy change of $E + eV/2$,
- Route 2 causes an energy change of $-(E - eV/2)$,
- Route 3 causes an energy change of $-(E + eV/E)$,
- Route 4 causes an energy change of $E - eV/2$.

As was the case when calculating the current shot noise, it is only the magnitude of the fluctuations in the tunnelling power that are of interest when calculating the noise. This means that to find to power noise, P_N , Equation 3.30 can be rewritten as:

$$P_N = \frac{2}{e^2 R_N} \int_{-\infty}^{\infty} \frac{E}{\sqrt{E^2 - \Delta^2}} \left[E(p_1 + p_2 + p_3 + p_4) + \frac{eV}{2}(p_1 - p_2 + p_3 - p_4) \right] dE. \quad (3.70)$$

As explained by Golubev and Kuzmin (2001) the heat flow noise, $\langle \delta P \rangle$, is given by:

$$\langle \delta P \rangle = \sqrt{2EP_N}. \quad (3.71)$$

This is the same as Equation 3.67 for the current noise but the electron charge (e) is replaced by the energy (E) which is fluctuating. Combining these two equations give the heat flow noise to be:

$$\langle \delta P^2 \rangle = \frac{4}{e^2 R_N} \int_{-\infty}^{\infty} \frac{E}{\sqrt{E^2 - \Delta^2}} \left[E^2 (p_1 + p_2 + p_3 + p_4) + \left(\frac{eV}{2} \right)^2 (p_1 - p_2 + p_3 - p_4) \right] dE. \quad (3.72)$$

Substituting for p_{1-4} gives the complete result:

$$\begin{aligned} \langle \delta P^2 \rangle = & \frac{4}{e^2 R_N} \int_{-\infty}^{\infty} \frac{E}{\sqrt{E^2 - \Delta^2}} \left[E^2 \left(\frac{1}{e^{\frac{E}{k_B T_S}} + 1} + \frac{1}{e^{\frac{-E}{k_B T_S}} + 1} + \frac{1}{e^{\frac{(E+eV/2)}{k_B T_e}} + 1} \right. \right. \\ & + \frac{1}{e^{\frac{-(E-eV/2)}{k_B T_e}} + 1} + 2 \frac{1}{e^{\frac{E}{k_B T_S}} + 1} \frac{1}{e^{\frac{(E+eV/2)}{k_B T_e}} + 1} \\ & \left. \left. + 2 \frac{1}{e^{\frac{-E}{k_B T_S}} + 1} \frac{1}{e^{\frac{-(|E|-eV/2)}{k_B T_e}} + 1} \right) \right. \\ & + \left(\frac{eV}{2} \right)^2 \left(\frac{1}{e^{\frac{E}{k_B T_S}} + 1} - \frac{1}{e^{\frac{-E}{k_B T_S}} + 1} + \frac{1}{e^{\frac{(E+eV/2)}{k_B T_e}} + 1} \right. \\ & - \frac{1}{e^{\frac{-(E-eV/2)}{k_B T_e}} + 1} + 2 \frac{1}{e^{\frac{E}{k_B T_S}} + 1} \frac{1}{e^{\frac{(E+eV/2)}{k_B T_e}} + 1} \\ & \left. \left. - 2 \frac{1}{e^{\frac{-E}{k_B T_S}} + 1} \frac{1}{e^{\frac{-(|E|-eV/2)}{k_B T_e}} + 1} \right) \right] dE. \quad (3.73) \end{aligned}$$

When combining the noise sources it is important to note that the current shot noise and the heat flow noise are correlated since the tunnelling power depends heavily on the current flowing through the junctions. As such the total noise resulting from these two source is not simply given by adding them in quadrature, instead a third term, the cross-correlator, needs to be added. For two correlated noise source (e_1 and e_2) the total noise, e_T can be found by:

$$e_T^2 = e_1^2 + e_2^2 + 2Ce_1e_2, \quad (3.74)$$

where the dimensionless constant C is the *correlation coefficient* which varies between -1 (if the two sources are anti-correlated) and $+1$ (if the two sources are

perfectly correlated). This means the correlator (the final term in Equation 3.74) of the current and heat flow noise, $\langle \delta P \delta I \rangle$, is given by:

$$\langle \delta P \delta I \rangle = 2C \langle \delta P \rangle \langle \delta I \rangle. \quad (3.75)$$

The current shot noise and the power noise have been shown by Golwala, Jochum, and Sadoulet (1997) to be anti-correlated so $C = -1$. Using this results and Equations 3.67 and 3.71 gives the correlator of the current shot and power noise to be:

$$\langle \delta P \delta I \rangle = -4\sqrt{eEI_NP_N}. \quad (3.76)$$

Golubev and Kuzmin (2001) show that in the case $T_e = T_S$ then this can be simplified to :

$$\langle \delta P \delta I \rangle = -4eP. \quad (3.77)$$

Substituting Equation 3.43 for tunnelling power gives the result:

$$\begin{aligned} \langle \delta P \delta I \rangle = 4eIV + \frac{8}{eR_N} \int_{-\infty}^{\infty} \frac{E^2}{\sqrt{E^2 - \Delta^2}} & \left[\frac{1}{e^{\frac{E}{k_B T}} + 1} - \frac{1}{e^{\frac{-E}{k_B T}} + 1} \right. \\ & \left. - \frac{1}{e^{\frac{(E+eV/2)}{k_B T}} + 1} + \frac{1}{e^{\frac{-(E-eV/2)}{k_B T}} + 1} \right] dE. \end{aligned} \quad (3.78)$$

The quantised flow of heat between the electron and phonon systems causes thermal fluctuations which result in further electrical noise. This noise is given by the well known expression:

$$\langle \delta P \rangle_{e-ph} = \sqrt{4k_B T^2 G_{e,ph}}. \quad (3.79)$$

$G_{e,ph}$ is the non direction specific thermal conductance between the two systems and is given by:

$$G_{e,ph} = |G_e| + |G_{ph}|, \quad (3.80)$$

This is true since noise results from heat flow to or from either system and is always positive. G_e and G_{ph} are given by:

$$G_e = \frac{dP_{e-ph}}{dT_e}, \quad (3.81)$$

$$G_{ph} = \frac{dP_{e-ph}}{dT_{ph}}, \quad (3.82)$$

work out how this
is done

where P_{e-ph} is the heating or cooling power of the electron-phonon link, given by Equation 3.48. Substituting these into the above gives:

$$G_{e,ph} = \left| \frac{d}{dT_e} \Sigma \Omega (T_e^\beta - T_{ph}^\beta) \right| + \left| \frac{d}{dT_{ph}} \Sigma \Omega (T_e^\beta - T_{ph}^\beta) \right|, \quad (3.83)$$

$$G_{e,ph} = \beta \Sigma \Omega (T_e^{\beta-1} + T_{ph}^{\beta-1}). \quad (3.84)$$

Substituting this into Equation 3.79 gives the final form of the heat flow noise:

$$\langle \delta P \rangle_{e-ph} = \sqrt{2\beta k_B \Sigma \Omega (T_e^{\beta+1} + T_{ph}^{\beta+1})}. \quad (3.85)$$

The factor of $\sqrt{2}$ difference between the above and Equation 3.79 can be explained by setting $T_e = T_{ph} = T$ in which case the two equations are the same.

The final source of noise to be considered is the system used to readout the detector. Inevitably this will involve some form of amplifier. Any amplifier will add a certain level of noise to a signal, this is usually the result of Johnson noise from the resistors used to set the amplifier's gain but can also be the result of shot noise due to the currents flowing in the amplifier. While intelligent design of an amplifier system (described by Horwitz and Hill, 1989) can result in amplifiers with very low noise levels (often of the order of $nV\text{Hz}^{-1/2}$), it is not possible to completely remove this noise source and as such it should be included when considering the fundamental limits of a system.

3.7 THE NOISE EQUIVALENT POWER

The electrical noise is a useful quantity in that it corresponds to what one would measure when characterising a detector however the eventual goal of any detector is not to itself be an object of study but instead be used to study other objects. As such the Noise Equivalent Power (NEP) is a more useful figure of merit since it gives the minimum power that can be detected with a signal-to-noise ratio of one and an integration time of half a second⁵ this allows someone using the detector to calculate if it is appropriate for an application given restrictions such as: signal power, measurement time or acceptable signal-to-noise ratio.

⁵The factor of a half comes from the formal definition of NEP being the power needed to achieve a signal-to-noise ratio (SNR) of one with a 1 Hz bandwidth. Because of the Nyquist-Shannon sampling theorem (Nyquist, 1928a; Shannon, 1949) the bandwidth, $\Delta\nu$, is defined as $1/(2T)$, where T is the integration time.

Add glossary entry: Sampling theorem and measurement bandwidth

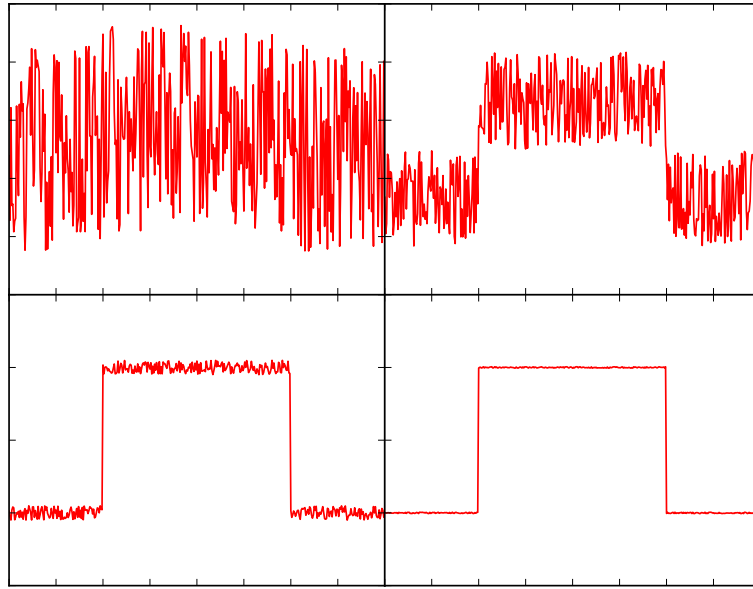


Figure 3.9: The effect of increasing the signal-to-noise ratio of a measurement. Left to right, top to bottom: $SNR = 0.1, 1, 10, 100$.

To derive the noise equivalent power it is perhaps most logical to start by specifying exactly what is meant by the *signal-to-noise ratio*. The signal-to-noise ratio is (as its name implies) simply the ratio of the amplitude of a signal to the amplitude of any noise on the signal. As such the signal-to-noise ratio, SNR , can be expressed as:

$$SNR = \frac{V_{signal}}{V_{noise}}, \quad (3.86)$$

where V_{signal} and V_{noise} are the Root Mean Square (RMS) voltages of the signal and the noise respectively.

The physical issues associated with a low signal to noise ratio are illustrated in Figure 3.9. It is clear that with $SNR = 0.1$ (upper-left in Figure 3.9) the signal can barely be seen and neither the width or amplitude can be ascertained. When the signal-to-noise ratio is increased to unity (upper tight is Figure 3.9) the presence of

a signal is clear but there are still significant uncertainties in both the amplitude and the width of the signal. When the signal-to-noise ratio is increased to 10 these uncertainties are greatly reduced and the pulse can be well characterised. Finally if the ratio is increased further to 100 the fluctuations are reduced to such a level that, except under close examination, they are not noticeable.

The units of noise equivalent power are $\text{WHz}^{-1/2}$. In order to calculate the noise equivalent power in the presence of noise sources, such as Johnson noise, which are most commonly measured or calculated as a voltage these quantities need to be converted into units of Watts. This is done by dividing the noise voltage (units: $\text{VHz}^{-1/2}$) by the voltage responsivity (Equation 3.63, units: VW^{-1}). Should the noise be measured or calculated in units of amperes (as is the case for Equations 3.66 and 3.77) then the noise needs to be divided by the differential of the IV-curve ($\partial I / \partial V$, units AV^{-1}) as well as the responsivity⁶.

The NEP is given by the total noise, e_{tot} divided by the responsivity (i.e. the incident power that would produce a signal equal in amplitude to the noise). This means it can be written as:

$$NEP = \frac{e_{tot}}{S_V \cdot SNR}. \quad (3.87)$$

The simplest example of calculating the noise equivalent power is to take the case where the measured noise is dominated by a single source. In the real world this is most commonly the case when the amplifier noise in the readout is not low enough. If we take the case where the amplifier noise, $\langle \delta V \rangle_{amp}$, is very large, i.e.:

maybe change to
 $\langle \delta V \rangle_{tot}$

Add ref to where
amp. noise is cov-
ered

$$\langle \delta V \rangle_{amp} = 100 \text{ nVHz}^{-1/2}. \quad (3.88)$$

Provided that this is significantly larger than any other noise source which contaminates the measurement then:

$$e_{tot} \approx \langle \delta V \rangle_{amp}. \quad (3.89)$$

⁶This paragraph assumes the detector is being current biased. Should the biasing signal be a voltage then sources measured in amperes do not need to be divided by the differential, whereas those measured in volts need to be divided by $\partial V / \partial I$ and the current responsivity is used.

If in this example the signal-to-noise ratio was 10^5 and the voltage responsivity was $1000 \text{ V}\text{W}^{-1}$, then the noise equivalent power would be:

$$NEP = \frac{\langle \delta V \rangle_{amp}}{S \cdot SNR}, \quad (3.90)$$

$$NEP = \frac{100 \times 10^{-9}}{1000 \times 10^5}, \quad (3.91)$$

$$NEP = 1 \times 10^{-15} \text{ W}\text{Hz}^{-\frac{1}{2}}. \quad (3.92)$$

In order to arrive at a term for total noise equivalent power of a detector system which includes a non-perfect amplifier, the various noise terms need to be converted into a noise equivalent power and then added.

Taking the noise terms individually it is possibly to see the specific conversions needed to change them to units of NEP ($\text{W}\text{Hz}^{-\frac{1}{2}}$).

For a voltage amplifier (as was always for the experiments in this thesis) the noise is in units of $\text{V}\text{Hz}^{-\frac{1}{2}}$ so division by the responsivity (which converts between volts and watts) is the only required step to convert the amplifier noise into a noise equivalent power.

$$NEP_{amp} = \frac{\langle \delta V \rangle_{amp}}{S_V}. \quad (3.93)$$

A brief inspection of the units of the heat flow noise ($\langle \delta P \rangle$) shows that this term, as expected, is already a noise equivalent power:

$$\langle \delta P \rangle = \sqrt{2EP_N}, \quad (3.71 \text{ revisited})$$

$$= \sqrt{JW}, \quad (3.94)$$

$$= \sqrt{WsW}, \quad (3.95)$$

$$= \sqrt{W^2s}, \quad (3.96)$$

$$= \sqrt{W^2 \text{Hz}^{-1}}, \quad (3.97)$$

$$\therefore \langle \delta P \rangle = \text{W}\text{Hz}^{-\frac{1}{2}}, \quad (3.98)$$

$$\therefore NEP_P = \langle \delta P \rangle. \quad (3.99)$$

A similar treatment reveals that the electron-phonon heat flow noise ($\langle \delta P \rangle_{e-ph}$)

is also already in units of noise equivalent power:

$$\langle \delta P \rangle_{e-ph} = \sqrt{2\beta k_B \Sigma \Omega (T_e^{\beta+1} + T_{ph}^{\beta+1})}, \quad (3.85 \text{ revisited})$$

$$= \sqrt{J K^{-1} W K^{-\beta} m^{-3} m^3 K^{\beta+1}}, \quad (3.100)$$

$$= \sqrt{JW}, \quad (3.101)$$

which is the same as Equation 3.94. Therefore:

$$\langle \delta P \rangle_{e-ph} = W \text{Hz}^{-1/2}, \quad (3.102)$$

$$\therefore NEP_{e-ph} = \langle \delta P \rangle_{e-ph}. \quad (3.103)$$

By dimensional analysis the units of the tunnelling current noise are shown to be $A \text{Hz}^{-1/2}$:

$$\langle \delta I \rangle = \sqrt{2eI}, \quad (3.67 \text{ revisited})$$

$$= \sqrt{CA}, \quad (3.104)$$

$$= \sqrt{AsA}, \quad (3.105)$$

$$\therefore = A \text{Hz}^{-1/2}. \quad (3.106)$$

this means that the tunnelling shot noise equivalent power NEP_S can be found by dividing the current noise by both the differential of the current by the voltage and voltage responsivity, i.e.:

$$NEP_S = \frac{\sqrt{2eI}}{\frac{\partial I}{\partial V} S_V}. \quad (3.107)$$

The final noise term to inspect is the correlator of the noise due to the tunnelling power and current ($\langle \delta P \delta I \rangle$). This is found to have units of $A \text{WHz}^{-1}$:

$$\langle \delta P \delta I \rangle = -4eP, \quad (3.77 \text{ revisited})$$

$$= CW, \quad (3.108)$$

$$= AsW, \quad (3.109)$$

$$\therefore \langle \delta P \delta I \rangle = A \text{WHz}^{-1}. \quad (3.110)$$

Add glossary entry: add shot noise

Which makes sense considering that dimensionally this is just the multiplication of $\langle \delta P \rangle$ and $\langle \delta I \rangle$. This means that the noise equivalent power due to this correlation of terms, NEP_{PI} , is given by:

$$NEP_{PI} = 2C \sqrt{\frac{eP}{\frac{\partial I}{\partial V} S_V}}, \quad (3.111)$$

$$NEP_{PI} = -2 \sqrt{\frac{eP}{\frac{\partial I}{\partial V} S_V}} \quad (3.112)$$

Having converted the various noise sources into units of NEP it is possible to arrive at a final equation for the total noise equivalent power of a CEB detector, NEP_{CEB} . This is found by simply adding the uncorrelated noise terms in quadrature with the addition of the cross-correlator of the power and current shot noise. This gives the final result for a current-biased device (i.e. a system using a voltage readout) to be:

$$\begin{aligned} NEP_{CEB}^2 &= \frac{\langle \delta V^2 \rangle_{amp}}{S_V^2} + 2\beta k_B \Sigma \Omega \left(T_e^{\beta+1} + T_{ph}^{\beta+1} \right) \\ &\quad + \langle \delta P^2 \rangle + \frac{\langle \delta P \delta I \rangle}{\frac{\partial I}{\partial V} S_V} + \frac{\langle \delta I^2 \rangle}{\left(\frac{\partial I}{\partial V} S_V \right)^2}, \end{aligned} \quad (3.113)$$

It is not advisable to write this equation more thoroughly (as was done for Equations 3.69 and 3.73) as this would be several pages long.

Go back and check that I use “current shot noise” consistently (I don’t!).

Chapter Four

The Properties of Doped and Strained Silicon

4.1 INTRODUCTION

The work detailed in this thesis explains the development (and hoped improvement) of the already existing cold electron bolometer by replacing the normal metal absorbing element used in previous devices (Kuzmin, 2004; Otto et al., 2013) with highly-doped strained silicon. As such it is useful to address the underlying principle of semiconductors and how their characteristics can be altered by either doping the material or by straining the materials atomic lattice.

4.2 INTRINSIC SEMICONDUCTORS

As is implied by their name semiconductors are material which are partially conductive—that is to say they do not conduct in the same way as a metal but nor do they prevent all current flow as insulators do. Semiconductors have a crystal lattice of atoms; the formation of this lattice can result in the creation of *free* electrons, these free electrons cease to be tightly bound to their parent nucleus (they are referred to as *delocalised*) and can flow (as current) through the crystal lattice of the material. In order for a *delocalised* electron to be able to flow as a current through the material it must first be removed from that atom to which it belongs by gaining a certain amount of energy (depending upon how tightly bound it is to

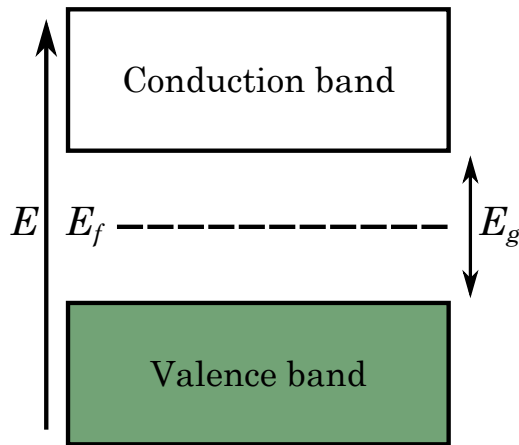


Figure 4.1: Band structure of an intrinsic semiconductor. With no additional energy for the electrons to absorb all the electrons are bound to their nucleus and exist in the valence band. In order to flow as a current they must gain enough energy to break their binding to the nucleus. For the most weakly bound electrons this energy corresponds to the band gap energy, E_g . E_f is the Fermi level, for an intrinsic (undoped) semiconductor this is located halfway through the energy gap.

the atom). This energy can be in the form of thermal energy from heating the crystal (as such semiconductors, unlike metals, have an electrical conductivity which increases with temperature) or by providing an external electrical bias across the material.

The requirement for some threshold energy to be met before an electron can flow as current can be thought of in terms of an energy band diagram, as shown in Figure 4.1. Without the input of any additional energy all the electrons are bound to their respective nuclei and are unable to flow as current through the material (the material is an insulator), these electrons have low energies and exist in the valence band shown in Figure 4.1. The top of the valence band corresponds to the most energy level of the most weakly bound electrons (that is the energy level of the outer most electron shell). However, this does not mean that any infinitely small increase in the energy of these electrons will liberate them from their nucleus, instead they must gain enough energy to enter the conduction band. This means that for the electrons in the outer most electron shells to be able to flow as current they must gain enough energy to *jump* through the band gap; this is

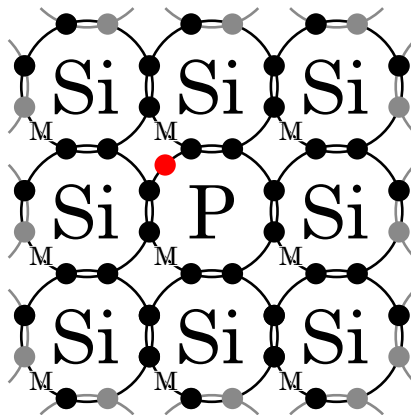


Figure 4.2: Crystal lattice of silicon with an n-type dopant (phosphorus in this case) grown into the lattice. For n-type doping the dopant has more electrons in its outer shell than are required to form covalent bonds with the surrounding atoms in the lattice, this results in an additional electron (highlighted in red above) which is not bound to the crystal lattice and acts as a *free* electron, increasing conductivity.

the band gap energy¹ and has a value of E_g .

4.3 DOPED SEMICONDUCTORS

The intrinsic semiconductor, explained above and whose energy level diagram is shown in Figure 4.1, is the basis for all forms of semiconductors and can be thought of as being characterised (at least in the sense of its energy distribution) by the size of its energy gap. However, one key advantage of semiconductors is that their conductivity can be controlled by adding impurities to the crystal lattice, this process is called *doping*.

In order for the doping to alter the electrical characteristics of a semiconductor the impurity added must bond to the crystal lattice in such a way that an unbound electron is added to the crystal or that a vacant electron state is created. Figure 4.2 illustrates the case where an unbound electron is added, referred to as *n-type* doping since a negative charge is added to the crystal. In this case the dopant impurity (phosphorus in Figure 4.2) has five electrons in its outer shell, four of

maybe add a ref?

Add glossary entry: doping

¹Throughout this work E_g will be used to refer to the band gap energy of semiconductor to avoid confusion with Δ which is used to denote half of the energy gap in a superconductor.

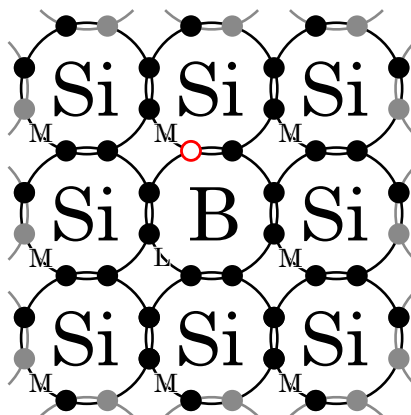


Figure 4.3: Crystal lattice of silicon with a p-type dopant (boron) grown into the lattice. For p-type doping the dopant has fewer electrons in its outer shell than the neighboring atoms. This means the atom does not form covalent bonds with all of the neighboring atoms and a hole (highlighted red) is created.

these form covalent bonds with neighboring silicon atoms however one electron does not form a covalent bond, the impurity is called a *donor* since, when ionised by a sufficient energy, the atoms *donates* an electron to the conduction band, this has the net effect of increasing the conductivity of the semiconductor.

The opposite of n-type doping is *p-type* doping—where the ‘p’ denotes positive charge—where the dopant used has fewer electrons in its outer electron shell than the rest of the atoms in the lattice. This means that there are incomplete covalent bonds (or *holes*) in the crystal structure which can capture free electrons. This is illustrated in Figure 4.3 where boron has been grown into a lattice of silicon. Boron is a group XIII element and has three electrons in its outer shell compared to silicon which has four (group XIV); this *missing* electron (shown in Figure 4.3 as an empty red circle) means that a covalent is unable to form between the dopant and one of the neighboring silicon atoms. The dopant in this case is referred to as an *acceptor* since an electron can become bound or *accepted* into the vacant state. Like n-type doping, p-type doping also has the effect of increasing the conductivity since, when ionised, the hole can become mobile and move through the lattice meaning that electrons switch places with the hole and thus also move through the lattice.

Add glossary entry: holes

Switch to vectors

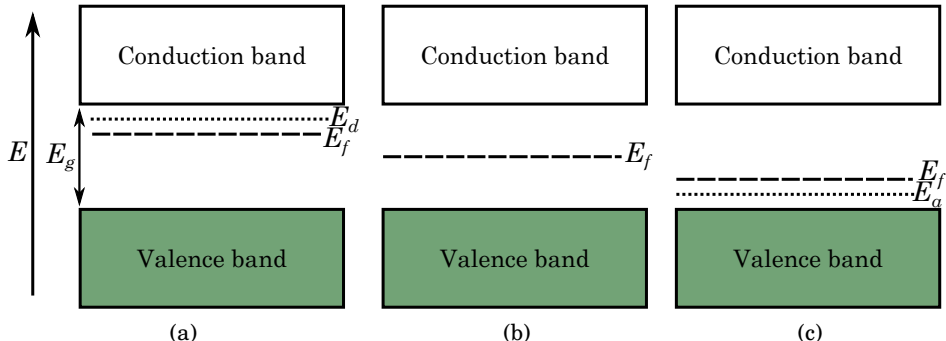


Figure 4.4: Energy level diagrams for doped semiconductor. (a) N-type doped semiconductor—since the dopant adds an additional electron to the lattice the Fermi-energy (E_f) is increased, E_d is the ionisation energy required to unbind the additional electron of the donor dopant from its parent nucleus. (b) Intrinsic semiconductor—since there are no dopants present in the lattice there are no ionisation levels and the Fermi-energy is in the middle of the band gap (as was seen in Figure 4.1). (c) P-type doped semiconductor—the dopant reduces the number of electrons (compared to an intrinsic semiconductor) and thus the Fermi-energy is reduced, E_a is the ionisation energy required to unbind the hole state from the acceptor dopant.

Since doping alters the distribution of electrons in a semiconductor, the energy level diagrams for doped semiconductors differ from that of an intrinsic semiconductor (shown in Figure 4.1). Figure 4.4 shows the energy level diagrams for n- and p-type semiconductors (Figures 4.4a and 4.4c) along with that of an intrinsic semiconductor (Figure 4.4b) for comparison. For doped semiconductors the energy level diagram include an additional level corresponding to the ionisation energy of either the additional electron from the donor atom (n-type), E_d , or hole state from the acceptor atom (p-type), E_a . Since n-type doping creates a positively charged region (due to the addition of one or more electrons) the Fermi-energy in an n-type semiconductor is increased (moved towards the conduction band) compared to the intrinsic case (Figure 4.4b). In the case of p-type doping the dopant creates a positively charged region around it where there is a shortage of electrons, this has the effect of decreasing the Fermi-energy in comparison to the intrinsic case.

One important physical feature of doping worth mentioning is that since the

dopant is added to the lattice during its growth it does not displace an atom but instead simply forms as part of the lattice.

By increasing the number of dopants present within the lattice the degree by which the conductivity of the lattice is altered can be carefully controlled. Pearson and Bardeen (1949) showed that introducing phosphorus dopants to a silicon lattice (n-type doping) at a concentration of $4.7 \times 10^{17} \text{ cm}^{-3}$ resulted in decreasing the materials resistivity to $0.3 \Omega \text{cm}$ at room temperature compared to $\approx 10^6 \Omega \text{cm}$ in the absence of any dopant atoms. Furthermore, increasing the doping concentration further to $4.7 \times 10^{20} \text{ cm}^{-3}$ (equivalent to approximately one per cent phosphorus) resulted in a resistivity of $7 \times 10^{-4} \Omega \text{cm}$.

The terminology of doped semiconductors typically distinguishes four vague levels of doping: *lightly-doped* semiconductors have doping levels $\lesssim 10^{14} \text{ cm}^{-3}$, this can be written as n^- - or p^- -type doping; *moderately-doped* semiconductors have dopant concentrations in the range $10^{14}\text{--}10^{16} \text{ cm}^{-3}$; *heavily-doped* is typically used in relation to doping levels in the approximate range $10^{16}\text{--}10^{18} \text{ cm}^{-3}$ and this level of doping is often expressed as n^+ - or p^+ -type doping; finally, when the doping level is such that the electrical behaviour of the material can be thought of as being analogous to a metal, it is referred to as being *degenerate*, this typically involves doping levels $> 10^{18} \text{ cm}^{-3}$ and is written as n^{++} - or p^{++} -type doping. While—as is true in various areas of physics—there are no exact guidelines or boundaries as to when a material ceases to be classed as lightly-doped and becomes moderately-doped, the term degenerate should be reserved in use for semiconductors which are doped to a sufficient level that they behave (electrically) like a metal.

4.4 CARRIER MOBILITY

Add glossary entry: mobility

The *mobility* of an electron or hole in a semiconducting crystal is defined as the speed at which the charge carrier *drifts* through the lattice per unit electric field. As such the mobility, μ is defined by:

$$\mu = \frac{|v|}{E}, \quad (4.1)$$

where $|v|$ is the modulus of the carrier's drift velocity and E is the electric field to which the carrier is subjected. The modulus of the drift velocity is used since mobility of electrons and holes (μ_e and μ_h respectively) are both defined to be

positive despite the fact that for an applied field of given polarity the two carrier types will move or drift in opposite directions.

It is easy to understand the relationship between the carrier mobility and the doping concentration by considering the movement of the carriers through the lattice. When an electric field is applied the carrier will be accelerated by the field, if the carrier were moving through free space then its velocity would continue to increase, due to the acceleration, to approaching the speed of light. However, in the crystal structure the carrier frequently collides with other particles (such as defects or impurities in the lattice), this causes the velocity of the carrier (on scales large than the mean free path between collisions) to be limited to some equilibrium between the accelerating force from the electric field and rate of collisions experienced. This velocity is the drift velocity referred to in Equation 4.1. After activation each dopant atom added to the lattice becomes ionised, as the carriers move through the lattice they collide with these ions and this decreases their drift velocity (and thus their mobility). Clearly increasing the doping concentration (and thus the number of ions) increases the frequency of collisions experienced by the carriers and accordingly their drift velocity and thus their mobility is decreased.

Data showing the overall relation between the mobility and the doping concentration, for both electrons and holes was compiled by Caughey and Thomas (1967)² who in turn drew heavily on the data of Irvin (1962). Caughey and Thomas used simple curve fitting techniques to fit the collected data. They showed that to a reasonable level the data for both the mobility of electrons and holes could be fitted with by:

$$\mu = \frac{\mu_{max} - \mu_{min}}{1 + \left(\frac{N}{N_{ref}}\right)^{\alpha}} + \mu_{min}, \quad (4.2)$$

where N is the number of dopant atoms per cubic centimetre, μ_{max} and μ_{min} are the maximum and minimum measured mobilities, N_{ref} is the total number of atoms per cubic centimetre, and α is a curve-fitting constant. All of these terms are dependent not only on the material but also on the carrier being studied. The fitting parameters found by Caughey and Thomas (1967) are given in Table 4.1 and their graph showing the fit to data collected for electron mobilities is reproduced in Figure 4.5

²There is a mistake in Caughey and Thomas's manuscript, the captions of Figures 1 and 2 should be switched.

Table 4.1: Carrier mobility curve-fitting parameters from Caughey and Thomas (1967).

Carrier	μ_{max} ($\text{cm}^2 \text{V}^{-1} \text{s}^{-1}$)	μ_{min} ($\text{cm}^2 \text{V}^{-1} \text{s}^{-1}$)	α	N_{ref} (cm^{-3})
Holes	495	47.7	0.76	6.3×10^{16}
Electrons	1330	65	0.72	8.5×10^{16}

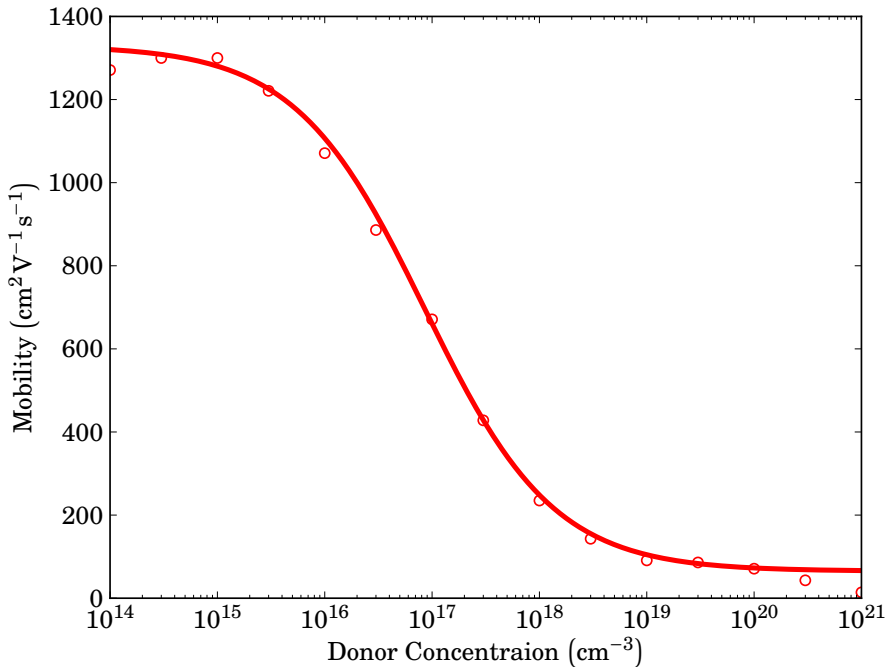


Figure 4.5: Decrease in electron mobility with increasing donor concentration. Circles—data, solid line—model fit. Reproduced, with permission, from Caughey and Thomas (1967). ©1967 IEEE.

While Equation 4.2 and the parameters found by Caughey and Thomas (1967) do not produce a model of the mobility based on physical process, they do act as a relatively accurate means of predicting the carrier mobility for a given doping concentration.

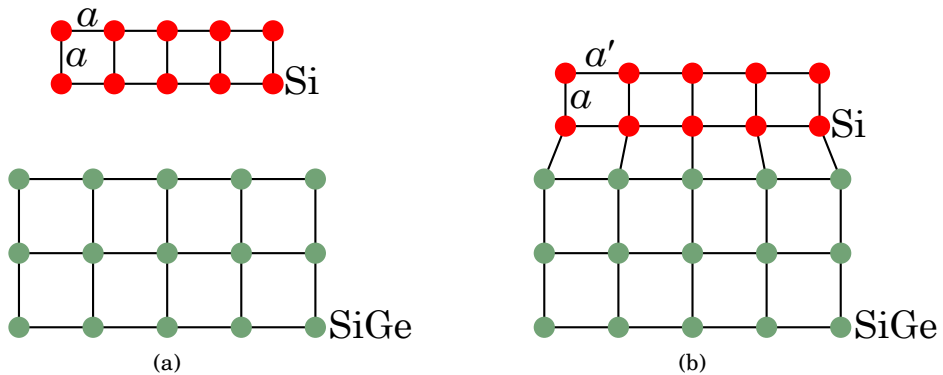


Figure 4.6: Introducing strain into a silicon lattice. (a) Silicon and silicon germanium as isolated lattices, the two materials have independent lattice spacings and in both cases the lattice spacing in both directions are the same, which is equal to a for the silicon lattice (a simple two-dimensional model is shown). (b) The effect of growing silicon atop of a layer of silicon germanium; the lattice becomes stretched or strained in the plane of the silicon germanium layer, changing the lattice spacing in this plane to a' while the lattice spacing in the vertical direction is unchanged.

4.5 STRAINED SEMICONDUCTORS

Straining silicon is the process of forcing the silicon atoms in the lattice to be slightly further apart than they would be naturally (the interatomic spacing is increased). This is achieved by growing silicon atop a buffer layer consisting of a material which has a larger atomic spacing than that of the silicon. Silicon germanium is commonly used as the buffer or straining layer since it readily forms bonds to the silicon lattice and the lattice spacing of this layer—and thus the level of strain in the silicon—can be controlled by adjusting the ratio of germanium in the silicon germanium. The concept behind the introduction of strain to a silicon lattice is shown in Figure 4.6.

[Switch to vectors](#)

The most common reason to introduce strain into a silicon lattice is to increase the carrier mobility. This occurs due to the strain forces stretching the crystal lattice, increasing the interatomic spacing and thus increasing the mean free path length between scattering events for the carriers. This is highly advantageous in

the field semiconducting electronic components where, for example, strained silicon offers substantial increases to the switching speed of transistors allowing for faster microprocessors. The improvement in carrier mobilities was first demonstrated by Welser, Hoyt, and Gibbons (1994), who showed that at low applied electric fields the electron mobility in n-doped ($N \approx 2 \times 10^{15} \text{ cm}^{-3}$) silicon strained by a SiGe layer ($\text{Si}_{0.7}\text{Ge}_{0.3}$) the mobility was increased to $\approx 1600 \text{ cm}^2\text{V}^{-1}\text{s}^{-1}$ compared to $\approx 600 \text{ cm}^2\text{V}^{-1}\text{s}^{-1}$ for a comparable unstrained system.

Another reason (particularly relevant to the field of detectors) to introduce strain into the silicon is that strained silicon has been shown by Muhonen et al. (2011) to offer decreased coupling between the electrons and the phonons. Muhonen et al. showed that at sub-Kelvin temperatures the heat flow between the electrons and the phonons was reduced by a factor of between 20–50 depending on the lattice temperature. In terms of detector performance this decrease in the electron-phonon coupling can increase a detector's sensitivity by decreasing the heat flow noise (from Equation 3.85). Furthermore, since the electrons are more thermally isolated from the lattice phonons they can, when cooled as described in Sections 3.3 and 3.4, be cooled further below the lattice temperature compared to electrons in unstrained material. This was shown by Prest et al. (2011) who used the same material described by Muhonen et al. (2011) as the central island of a microrefrigerator device. Prest et al. showed that at a lattice temperature of 300 mK a device utilising strained silicon was capable of cooling electrons to a minimum temperature of 174 mK compared to 258 mK for a device using unstrained silicon. This increase in performance is directly applicable to the cold electron bolometer not only in decreasing the heat flow noise but also by allowing the electrons in the absorber to operate at lower temperatures reducing the majority of noise contributions detailed in Section 3.6.

Optical Properties
and modelling (FP
model).

Chapter Five

Detector Design & Fabrication

5.1 INTRODUCTION

This chapter will detail the design of the Silicon Cold Electron Bolometer detectors studied in this work, it will also look at the process by which these devices have been fabricated. It should, however, be stated at the outset that the designs for these detectors had been arrived at prior to the commencement of this work; as such process by which the detector design was arrived at will not be covered here. The features of the design will have ever be examined, as will some minor modifications which were added to ensure both the detectors were both functional and relatively simple to fabricate with the facilities available in Cardiff at the time.

5.2 DETECTOR DESIGN

The designed detector was for a tin-slot antenna-coupled detector. The absorber (the doped-silicon island of the Silicon Cold Electron Bolometer, described in Chapter 3) was coupled to the antenna via Schottky contacts to the antenna's coplanar waveguide, these Schottky contacts served as the tunnelling contacts to the doped-silicon island as well as capacitively coupling incident radiation from the antenna via the same waveguide. Since the incident radiation typically has a high frequency (> 100 GHz) it couples directly to the absorber whereas the bias signal is DC and, as such, must tunnel through the Schottky contacts to reach the absorber, thus producing cooling as described in Chapter 3. A model of the final detector chip is shown in Figure 5.1.

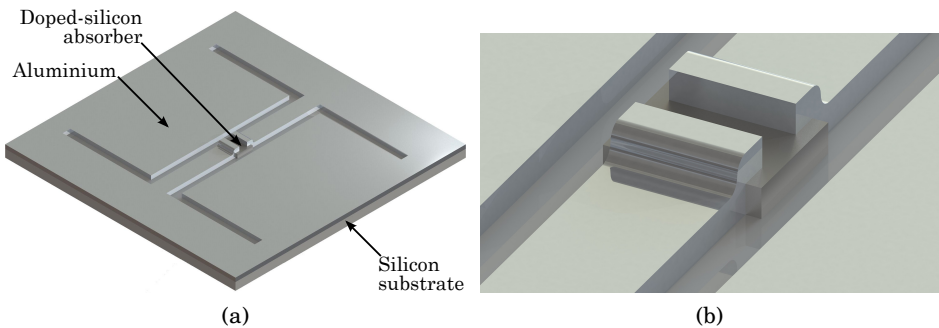


Figure 5.1: Model of Silicon Cold Electron Bolometer chip. (a)—whole detector chip with twin-slot antenna, the strained-silicon absorber is located in middle of a coplanar waveguide which is fed by a twin-slot antenna formed in an aluminium ground plane; (b)—zoomed-in view of the strained-silicon mesa which acts as the detector’s absorber. It should be noted that the height of the strained silicon mesa has been greatly exaggerated here in order to make this component visible. In reality the silicon substrate is in fact 25,000 times thicker than the mesa.

5.2.1 ANTENNA DESIGN

A twin-slot antenna was chosen for coupling radiation to the absorber, the reasons for this included the relatively simple design along with the fact this twin-slot antennae have a linearly-polarised response which allows for signals coupled to the absorber via the antenna to be differentiated from signals due to direct absorption in the strained-silicon mesa, in terms of a detector in an instrument, an antenna with a polarised response clearly allows for the polarisation of a source to be measured.

The key dimensions of a twin-slot antenna are shown in Figure 5.2. L is the length of the antenna’s slots and corresponds to half the wavelength that the antenna is intended to couple. A caveat to this is that the length corresponds to the wavelength in the medium, in the situation where radiation is coupled to the antenna via a silicon substrate (as indeed was the case in this work) where the refractive index, n , is equal to 3.42–3.48, this means that in this case $L = \lambda_0/2n \approx 0.28\lambda_0$ where λ_0 is the wavelength in free space. S is the separation between the two slots, this has been optimised via finite element simulation in Ansoft’s HFSS software. W is the width of the slots and is altered to achieve the desired antenna

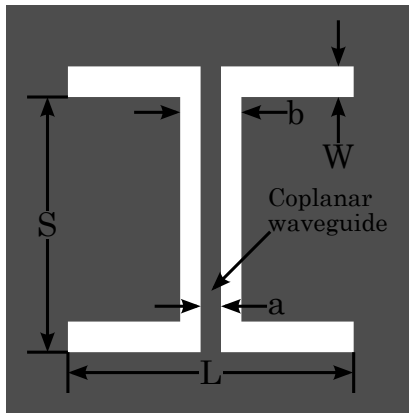


Figure 5.2: Key dimensions of a twin-slot antenna.

impedance. a and b are the dimensions of the coplanar waveguide and are governed by the desired impedance for the coplanar waveguide.

Three sets of detector design were created, each set had an antenna designed for a different frequency, the selected frequencies were: 160, 225 and 360 GHz. These frequencies were selected due to their similarity to the second to fifth bands of *Planck*'s High-Frequency Instrument (HFI) (which are 143, 217 and 353 GHz, as explained by Lamarre et al., 2003) used to study the Cosmic Microwave Background (CMB). The choice of these antenna frequencies was advantageous due to wealth of expertise—and indeed equipment—at Cardiff for these frequencies; it also allowed for the potential to access Silicon Cold Electron Bolometers for a potential application (studying the cosmic microwave background). The dimensions (as defined in Figure 5.2) of these three designs are given in Table 5.1.

Table 5.1: Dimensions of designed antennae.

Frequency (GHz)	L (μm)	S (μm)	W (μm)	a (μm)	b (μm)
160	536	333	30	30	58
225	356	230	20	30	58
360	226	155	15	30	58

It is clear that if one wishes to either bias or measure (or indeed if one wishes to do both) a bridge-type element on the coplanar waveguide then the design described above, and illustrated in Figure 5.1, has a major flaw: the metal ground

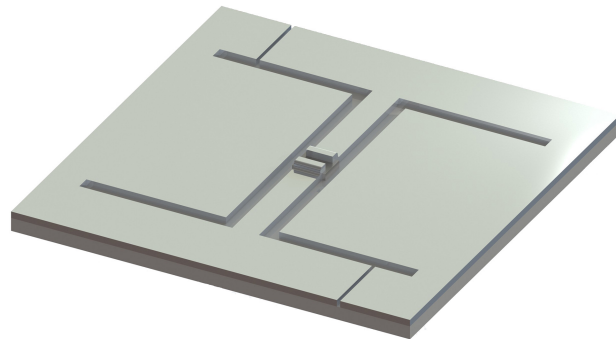


Figure 5.3: Model of Silcion Cold Electron Bolometer chip with DC cuts in the ground plane.

plane is contiguous around the twin-slot antenna and is connected directly to the coplanar waveguide, this means that any attempt to measure a resistive component on the coplanar waveguide would be futile since such a component would be shorted by the ground plane. In order to address this it was necessary to add cuts to the ground plane such as to force current to be driven through down the coplanar waveguide. These were placed on diagonally opposite slots of the antenna, this design is illustrated in Figure 5.3. While it is clear that these are required for the correct operation of the device it is fair to say that the placement of these slots was far from optimum since they altered the response of the antenna, this will be seen in greater detail in . With the gift of hindsight and greater study of literature it would have been better to have added to slots which extended the coplanar waveguide to one of the edges of the chip.

In order for the radiation to be absorbed into the doped-silicon mesa a break was made in the middle of the coplanar waveguide, where the mesa is situated. The coplanar waveguide overlapped the mesa on both sides and it was at these points that Schottky contacts were formed. This form of structure is often referred to as a bridge since the bolometer bridges the gap in the coplanar waveguide. This structure, along with the associated dimensions is illustrated in Figure 5.4.

Four different values for the contact length, c , ($(y-g)/2$ in Figure 5.4), these were 1, 3, 5 and 7 μm and were selected not only to allow a study of the effect of varying this parameter but also to help ensure successful fabrication. In all cases the dimensions g and x were 4 and 32 μm . The anticipated contact resistance for these

[add ref](#)

[add footnoted references](#)

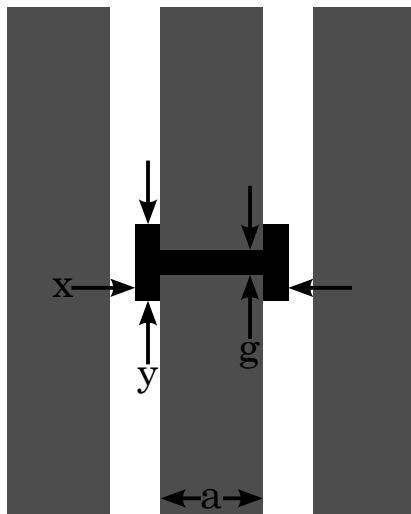


Figure 5.4: Dimensions of bolometer bridge in a coplanar waveguide. The contact length, c , is given by $(y-g)/2$.

devices was found based on the contact resistivity which has been measured for both unstrained and strained doped silicon. The measured values for the contact resistivity, ρ_c were $1.28 \times 10^{-4} \Omega\text{cm}^2$ for the unstrained doped silicon and $5.12 \times 10^{-3} \Omega\text{cm}^2$ for the strained silicon. The dimensions of the bridge were not varied with the different antennae frequencies. The dimensions and expected contact resistance, R_c , are given in Table 5.2.

Table 5.2: Dimensions and expected contact resistance for different bolometer bridge designs.

c (μm)	x (μm)	y (μm)	a (μm)	g (μm)	Unstrained	Strained
					R_c (Ω)	R_c ($\text{k}\Omega$)
1	32	6	24	4	533	21.3
3	32	10	24	4	178	7.1
5	32	14	24	4	107	4.3
7	32	18	24	4	76	3.0

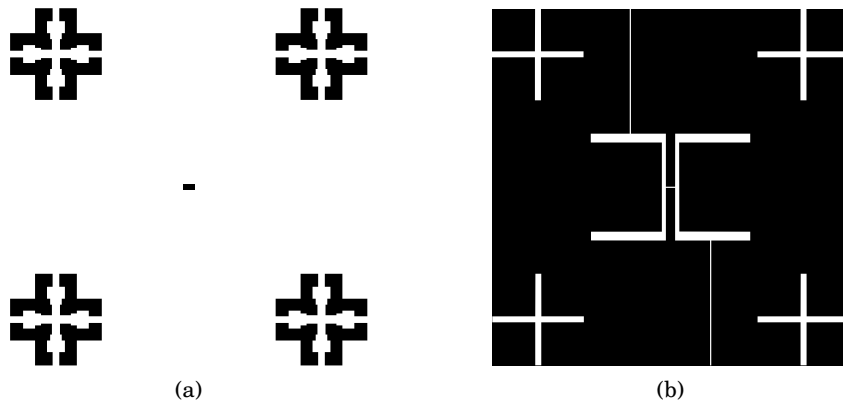


Figure 5.5: Example sections from the photomask used to fabricate Silicon Cold Electron Bolometers. (a)—first step, creation of the absorbing mesa; (b)—second step, creation of the twin-slot antenna structure. In both stages the features on the mask in black were protected from the etching process and thus were present on the final detector chip. The features in the corners are alignment marks used to align the mask during the second stage.

5.3 DETECTOR FABRICATION

The detector chips were fabricated via sputter deposition and photolithographic techniques. In order for the devices to be fabricated a photomask was created. This mask was used for the two steps in the fabrication process which required etching of a material (covered later in this section); an example of two sections of this mask, used to create a single detector, is shown in Figure 5.5. In this figure features in black are those protected from the etching process and are those present on the final detector chip. In Figure 5.5a this corresponds to doped silicon whereas in Figure 5.5b this corresponds to aluminium.

The fabrication process itself is relatively simple containing only three etching steps and a single deposition step. The full process flow for the fabrication of the detectors tested in this work is given in the following points:

Initial wafer The starting wafers have been grown at The University of Warwick and have been detailed by Muhonen et al. (2011). The wafers consist of a silicon (001) substrate, followed by a 30 nm layer of epitaxial n⁺⁺ silicon in the case of the

and illustrated
in...???

unstrained silicon. In the case of the strained silicon a 2 μm thick graded layer of $\text{Si}_{1-x}\text{Ge}_x$ is grown on top of the substrate; this layer is linearly grader from $x = 0$ at the interface to $x = 0.2$. This layer is followed by a 500 nm layer of $\text{Si}_{0.8}\text{Ge}_{0.2}$. Finally a 30 nm layer of n^{++} silicon is grown on top of the SiGe.

Mesa defined The mesa structure (the absorber) is defined with photoresist. This is applied evenly to the wafer and briefly baked to ensure all excess liquid is removed. The first stage of the photomask (Figure 5.5a) is then placed over the wafer and the photoresist is exposed to ultraviolet light through the photomask. Parts of the mask which are solid (those which are black in Figure 5.5) block the ultraviolet light, protecting the photoresist. The photoresist which has been exposed is weakened and removed with a developer solution.

Mesa etching The mesa structure is created via etching away the undesired parts of the doped-silicon layer. The etching process is unable to etch through the photoresist and thus only the regions exposed to ultraviolet light in the previous step are etched. For the creation of Silicon Cold Electron Bolometers this etching was performed with a CF_4/O_2 gas etch. The parameters for this etch were: 30 sccm at a pressure of 50 mBar and a power of 100 W.

Surface preparation During early testing of junctions it was found that in order to create a high-quality Schottky barrier it was vital to remove the thin layer of silicon oxide (SiO_2) which formed on the doped silicon during storage of the wafer and the above steps. This was performed by briefly etching the wafer in a weak aqueous solution of hydrofluoric acid. This process removed the silicon oxide layer and left hydrogen-terminated silicon at the surface, preventing re-oxidisation of the wafer.

Aluminium deposition The aluminium—which created the contacts to the doped-silicon absorber as well as the ground plane for the antenna—was deposited via sputter deposition. This was performed at a pressure of 5×10^{-3} mBar and a sputter power of 150 W. The sputtering gas used was Argon.

Antenna defined The antenna pattern was defined with the second stage of the photomask (Figure 5.5b) and the same process as described above for the mesa.

Antenna etching The antenna structure was etched using a wet etching solution consisting of 26 parts HPO_3 , 6 parts H_2O and 2 parts nitric HNO_3 . The final aluminium layer was approximately 100 μm thick.

The process above was used for the fabrication of all devices. The cross sections

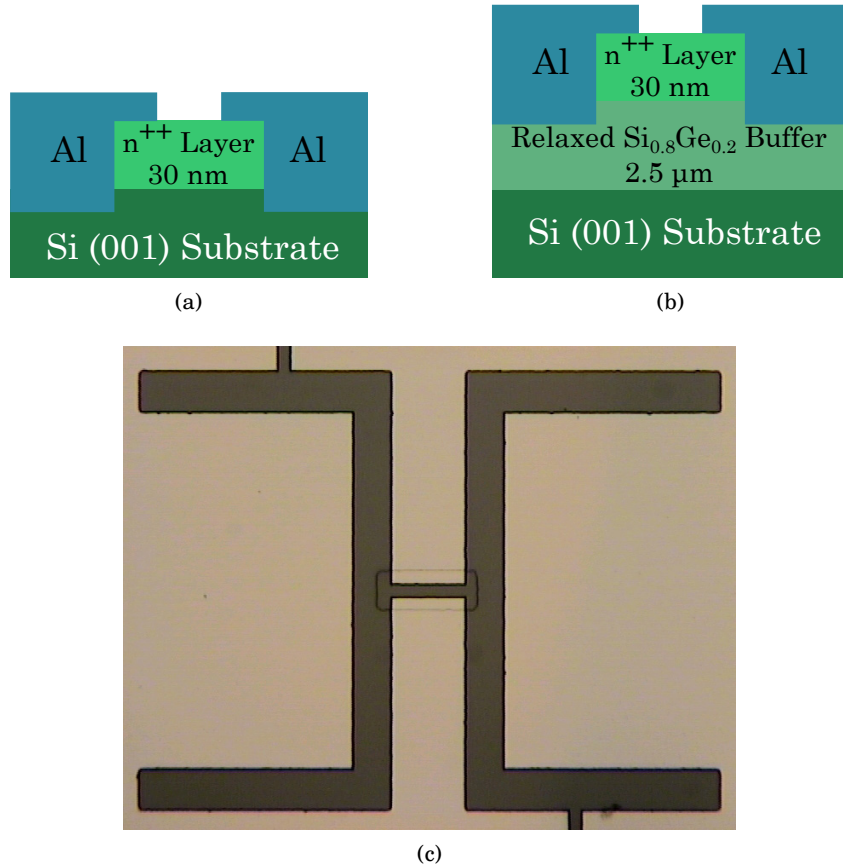


Figure 5.6: (a)—cross section of a unstrained SiCEB detector. (b)—cross section of a SiCEB detector with a strained-silicon absorber. Both cross sections are along the axis of the coplanar waveguide. (c)—optical photograph of a Silicon Cold Electron Bolometer.

of the two types of detector fabricated (those with and without a strained absorber) are shown in Figure 5.6 along with a photograph (taken using a microscope) of one of the fabricated devices.

5.4 MATERIAL PROPERTIES

As has been mentioned previously in this chapter two different silicon wafer have been used to fabricate Silicon Cold Electron Bolometers. These were an unstrained

highly-doped silicon (sometimes referred to in literature as the *control* material, wafer reference number: 5365) and strained highly-doped silicon (wafer reference number: 5362). A detailed study of these two materials has been presented by Muhonen et al. (2011) but a summary of the key properties of these two materials is given in Table 5.3.

Table 5.3: Summary of key material properties for unstrained (control) and strained silicon materials.

Parameter	Unstrained	Strained
Dopant Concentration (cm^{-3}) ^a	4×10^{19}	4×10^{19}
Strain Layer ^a	N/A	$\text{Si}_{0.8}\text{Ge}_{0.2}$
Carrier Density (cm^{-3}) ^a	3.1×10^{19}	2.7×10^{19}
Mobility ($\text{cm}^2\text{V}^{-1}\text{s}^{-1}$) ^a	192	155
Electron-Phonon Coupling, Σ ($\text{WK}^{-6}\text{m}^{-3}$) ^b	5.2×10^8	2.0×10^7
Sheet Resistance (Ω/\square)	384	571
Al-Si Junction Resistance ($\text{k}\Omega\mu\text{m}^2$)	13	512

^a From Muhonen et al. (2011).

^b From Prest et al. (2011).

The sheet resistance and aluminium-silicon junction resistance have been measured at Cardiff.

Chapter Six

Cryogenic Testbeds

6.1 INTRODUCTION

As is the case with all ultra-sensitive mid- to far-infrared detectors (as described by Richards, 1994), the silicon cold electron bolometer requires cooling to extremely low temperatures in order to operate. This requirement can be seen from the description of cold electron bolometers given in Chapter 3. Since these detectors incorporate superconducting contacts to select only the most energetic (i.e. the hottest) electrons from the detector's absorber, it is important that the superconductor is cooled sufficiently that the superconducting energy gap is close to its maximum. For the detectors studied in this work, which used aluminium contacts, it was found that cooling to approximately $\sim T_c/4$ (300 mK) allowed the detector to Add cross-ref operate reasonably. However, in order to arrive at as complete a study as possibly it was important to measure the electrical properties of the detectors to as low a temperature as possible.

To this end several different cryogenic systems have been used in the course of this work. The most significant of these (those in which results presented in this thesis were taken) were: an adiabatic demagnetisation refrigerator housed in a liquid helium cryostat, a He10 sorption refrigerator housed in a cryostat with a pulse tube cooler, and a He7 sorption refrigerator mounted on the cold plate of a liquid helium cryostat.¹ The reason for the use of these numerous system

¹Note: He7 and He10 here do not denote some strange and exotic isotopes of helium but instead the combination of pumps which make up the sorption refrigerator. Isotopes have been typeset with a leading superscript (i.e. ^4He). A He7 refrigerator contains one ^4He pump and a ^3He pump, a He10 refrigerator consists of a He7 refrigerator used as a buffer stage for a second ^3He pump.

was essentially due to availability and the associated costs of liquid helium. Primary measurements were carried out in the pulse tube cooled cryostat since this had lower running costs (due to not requiring a reservoir of liquid helium to be maintained). However (as will be seen later in this chapter), the system was not designed with the dc readout of sensitive detectors in mind and resulted in lower quality data than would have been desired; however it did provide a useful facility for asserting whether or not a device was functional. The two other systems, both of which required the supply of liquid helium, were used for very specific purposes. The ADR system was used to measure device down to extremely low temperatures (the minimum temperature achieved with this system was 80 mK) whereas the system containing a He7 refrigerator contained optical windows, horns and filters to allow the detector to observe external sources. This chapter will cover the operational principles along with the cryogenic performance and suitability for the required measurements of each of these systems.

6.2 SORPTION REFRIGERATORS

Sorption refrigerators operate by the adsorption and desorption of a working gas (helium in the case of systems intended to operate at cryogenic temperatures) from a surface or other material (most commonly activated charcoal). The released gas flows through a pipe until it is cooled by a condensation point and liquified. This liquid is collected in a stage called the evaporator. The activated charcoal is then cooled causing the gas evaporating from the liquid in the evaporator to become reattached to the charcoal thus decreasing the pressure in the system and thus the temperature of the liquid in the evaporator. An artistic impression of a single-stage sorption refrigerator is shown in Figure 6.1

In order to understand a sorption refrigerator it is perhaps easiest to consider the typical procedure followed to cycle such a system. The general procedure is as follows:

Cool system to working temperature. In order to function the condensing stage of the system must be cooled to the boiling point of the working gas (this is 4.2 K for ${}^4\text{He}$). This is performed by either filling the cryostat in which the refrigerator is housed with liquid helium (in the case of *wet* systems) or switching on the cryostat's mechanical cooler (for *dry* systems) and waiting for all the parts of the

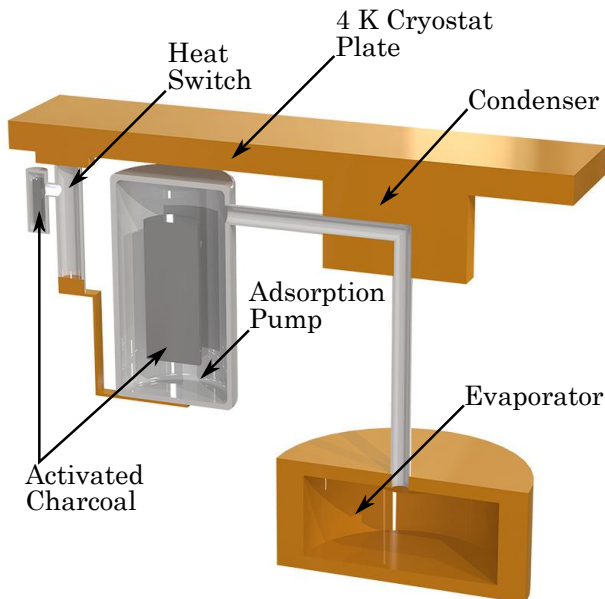


Figure 6.1: Artistic impression of the cross section of a sorption refrigerator. The 4-Kelvin plate of the cryostat is cooled by either a liquid-helium reservoir or a mechanical cooler (not shown in either case).

system to thermalise.

Heat the charcoal in the pump. The pump is heated (usually via a film resistor mounted to the outside of the pump) causing the gas to be released from the activated charcoal (sometimes referred to as the *getter*). As the charcoal is heated to above 10 K helium will begin to be released and by 25 K the vast majority will have been released.

Helium condenses. Increasing the temperature further causes the pressure within the refrigerator to increase causing the gas to come into contact with the condenser and where it will condense. This liquid will then collect in the evaporator (situated beneath the condenser).

Charcoal cooled. The charcoal in the pump is then cooled again. This is performed using a heat switch. The heat switch has one side connected to the pump and the other to the cold plate of the cryostat. The most common type of heat switch used in conjunction with sorption refrigerators is the gas-gap heat switch. This can be thought of as simply a small sorption refrigerator. The heat switch is made of two copper caps connected by extremely-thin walled stainless steel tube

(which has negligible thermal conduction); attached to this via a second thin tube is a cylinder containing a charcoal getter. The heat switch also contains helium gas. When the switch is open (off) the helium is attached to the getter and there is little or no thermal conduction between the two copper caps. The heat switch is closed (switched on) by heating the charcoal causing the helium to be released into the stainless steel tube which results in the thermal conduction between the two copper caps increasing substantially. The closing of the heat switch creates a link between the pump and the cold plate of the cryostat and thus cools the pump.

Pressure reduces. As the charcoal in the pump cools to below 25 K it is once again able to attract and hold gas. This means that as helium molecules evaporate from the liquid they become attached to the activate charcoal (through adsorption) which causes the pressure in the system to reduce. This in turn lowers the temperature of the liquid in the evaporator along with the walls of the evaporator.

The above process is for a single-stage helium-4 sorption refrigerator, such systems are capable of achieving temperatures, at the external walls of the evaporator, of around 1 K. To achieve sub-Kelvin temperatures with a sorption refrigerator one must use helium-3 as the working gas, this necessitates that the condensation point must be at a lower temperature (^3He has a critical point or 3.3 K).

In order to meet this requirement it is common practice to use a helium-4 pump as a buffer stage to cool a condensation point on a helium-3 pump (this is what is referred to as a He7 system).² This technique was first reported by Dall’Oglio et al. (1991) who at the time achieved a minimum temperature, at the evaporator of the ^3He pump, of 300 mK.

Further cooling can be achieved with sorption refrigerators by using the He7 system described above to cool a further helium-3 pump (thus making a He10 system). This type of system was first introduced by Bhatia et al. (2000) who described a system capable of achieving a minimum temperature of 234 mK for 20 hours under minimal thermal loading ($\approx 0.9 \mu\text{W}$) or 242 mK for 12 hours under a total thermal load of $3.9 \mu\text{W}$. Further improvements to design of such systems, coupled with the lower starting temperatures offered by pulse tube coolers, has resulted in minimum operating temperatures of lower than 220 mK being achieved under realistic experimental thermal loading.

²It is worth mentioning that as mechanical cooling technology (e.g. pulse tubes) is improving, these systems can, under low to medium thermal loads, other sufficiently low temperatures to cycle a helium-3 sorption cooler directly without the need of a buffer stage.

6.3 ADIABATIC DEMAGNETISATION REFRIGERATION

Adiabatic Demagnetisation Refrigeration (ADR) utilises changes in entropy in a working medium (a salt pill) which is either connected to or isolated from a heat sink depending on the stage of the refrigeration cycle. As opposed to the sorption refrigerators previously described, the heat switch technology used with adiabatic demagnetisation refrigerators (at least the systems based at Cardiff) is the mechanical heat switch. This type of heat switch uses moving parts to make physical contact between two sides of the switch. This results in the open (off) state of the switch having a much lower heat flow than in the case of the gas-gap heat switch previously mentioned. A disadvantage of this technology is that since some degree of mechanical motion is required, the automation of the switch is more complicated, requiring either solenoid- or motor-controlled switches. An artist's impression of a simple adiabatic demagnetisation refrigerator is shown in Figure 6.2, it is worth noting that it is common practice to encompass the magnet with a magnetic shield (not shown) as to reduce stray magnetic fields which may interfere with measurements.

Update to re-rendered image

As before it is beneficial when discussing the principles involved in adiabatic demagnetisation refrigeration to follow the thermal circle of such a system. A typical cycling procedure for a system such as the one illustrated in Figure 6.2 is:

Magnetic field increased. With the heat switch closed the magnet current is increased causing the salt pill to be subjected to an increasing magnetic field. This field causes the magnetic dipoles within the salt pill to align. This places the salt in a more ordered state, lowering its entropy. Thermal energy added to the salt pill is removed to the 4-Kelvin heat sink.

Heat switch opened. With the peak magnetic field (typically up to 4 T) still applied, the heat switch is opened. This disconnects the salt pill (and the attached cold stage) from the 4-Kelvin heat sink, placing these components in an adiabatic state.

Magnetic field decreased. The current supplied to the magnet is lowered gradually to decrease the magnetic field. This allows the magnetic dipoles within the salt pill to fall out of alignment thus creating a more disordered state. This produces cooling since, because the system has been placed in an adiabatic state, the

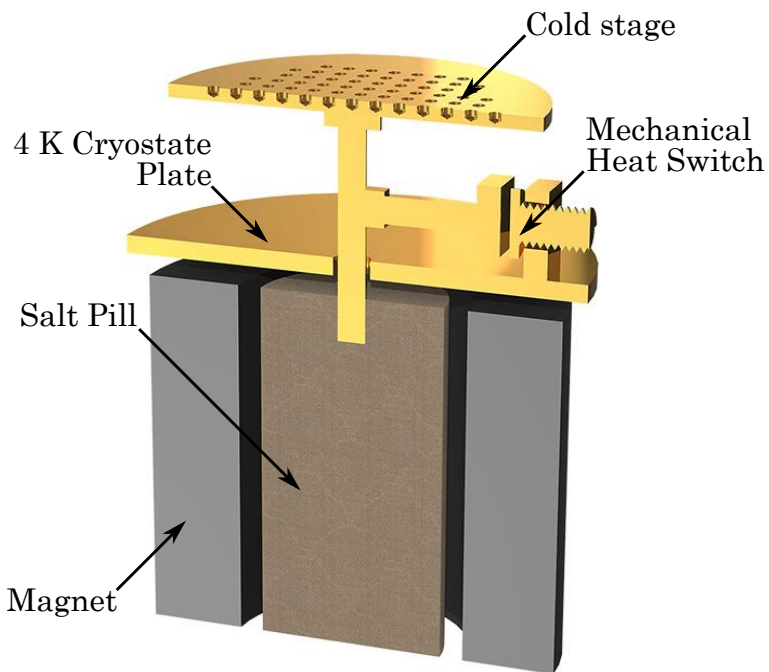


Figure 6.2: Artistic impression of a simple single-stage adiabatic demagnetisation refrigerator. The 4-Kelvin plate of the cryostat is cooled by either a liquid-helium reservoir or a mechanical cooler (not shown in either case).

total entropy cannot change. To accommodate the disorder (increased entropy) introduced by the removal of the magnetic field the temperature of the salt pill falls (lowering the entropy), maintaining the entropy at a constant level.

Once the magnetic field has been reduced once again to zero the system will slowly heat up since the dipoles are free to relax into a disordered state. This means that, at zero field, an adiabatic demagnetisation refrigerator does have zero cooling power. Due to this when adiabatic demagnetisation refrigeration is utilised for applications requiring a constant temperature to be maintained for a period of time it is necessary to decrease the field to a level corresponding to required level and hold the field at this level. As the salt pill slowly warms the field can be reduced further to compensate. Once the field has reached zero no further cooling is available and a rise in the salt pill's temperature becomes inevitable. The longer

hold time associated with this technique was not required for the measurements taken for this work and as such it was sufficient to simply reduce the magnetic field to zero and allow the salt pill (and the attached cold stage) to gradually warm.

The minimum achievable temperature of an adiabatic demagnetisation refrigerator is predominately governed by two factors: the maximum field applied to the salt will (i.e. the degree of order introduced in the non-adiabatic state) and the salt used to construct the salt pill³; some of the most prolifically used salts are: chromic caesium alum (CCA), ferric ammonium alum (FAA), and gadolinium gallium garnet (GGG); each of these has its own optimum operation temperature. The initial temperature of the refrigerator also contributes greatly towards the minimum achievable temperature but here it assumed that this is determined by the thermal reservoir (e.g. liquid helium) and cannot be improved upon.

In order to achieve temperatures below 100 mK it is necessary to use a system containing multiple salt pills. Such a two-stage system was first described by Hagmann and Richards (1994), which is not dissimilar to the system used for parts of this work. The concept of such a system is, conceptually, similar to that described for sorption refrigerators in the previous chapter. The first salt pill acts as a buffer stage for any thermal loads (such as wiring) to the coldest stage. Both stages can be cycled simultaneously since the first stage does not need to reduce the temperature of the second below any critical temperature before cycling is possible (as is the case for sorption refrigerators), instead it simply acts to reduce the thermal load on the second stage. This means only one magnet is required to run both stages. The system used in this work (manufactured by Janis Cryogenics) used in this work used gadolinium gallium garnet for the first stage and ferric ammonium alum for the second stage. These stages were capable of achieving minimum temperatures of 1 K and 70 mK respectively.

6.4 SYSTEMS USED IN THIS WORK

Three systems have been used for the majority of the low-temperatures measurements carried out in the course of this work. These were: a liquid-helium cryostat

³At this point it is worth mentioning that the depiction of a salt pill shown in Figure 6.2 is extremely simplified. For a more complete description of these components see, for example, Hagmann, Benford, and Richards (1994).

housing a two-stage adiabatic demagnetisation refrigerator; a cryostat (affectionately known as Aloysisius) with a pulse-tube cooler upon which a He10 sorption refrigerator was mounted; and a liquid-helium cryostat, containing windows to facilitate optical measurements, in which a He7 sorption refrigerator was mounted. Each of these systems served a specific role whether it be: facilitating optical measurement of detectors or characterisation at extremely low temperatures. Each of these system is discussed in greater detail in the following subsections.

6.4.1 PULSE TUBE COOLED CRYOSTAT WITH HE10 SORPTION REFRIGERATOR

The first system used to characterise Silicon Cold Electron Bolometers was a pulse tube cooled cryostat incorporating a He10 sorption refrigerator.⁴ This system had a large (260 mm in diameter) cold plate which could be cooled to a minimum temperature of 220 mK, which could be maintained for in excess of 48 hours. The system also contained a set of windows to enable the measurement of a detector's response to an external source to be measured. These windows were, for the most part, however not used since an alternative system (discussed later in this section) enable a much more complete optical study of a detector.

The main measurements that this cryostat was used for were the initial verification of the device's function (i.e. whether tunnelling contacts to the silicon absorber had formed correctly), along with dark characterisation of the device (i.e. measuring the current-voltage relationship of the detector at various bath temperatures). It is worth mentioning that pulse tube cooler based cryogenic systems can contribute additional, undesired, components when measuring noise spectra. These are caused by the pulsing of the mechanical cooler introducing movement at various stages of the cryostat. This movements can cause any of the following: thermal oscillations, movement of wiring (causing electrical variations through either changes to the wiring's capacitance or through induction), or alternations to the optical alignment of components. Clearly in order to accurately measure the performance of any device mounted within such a system it is vital not only to discover the magnitude of these effects but also to reduce their presence as much as possible. The various effects of microphonics, along with a considerably more

⁴This cryostat was affectionately known as Aloysisius since—due being large, orange and involving several hose lines for the pulse tube cooler—it possibly bore something of a resemblance to the character Aloysisius Snufflepagus in *Sesame Street* (see Sesame Workshop, 2015).

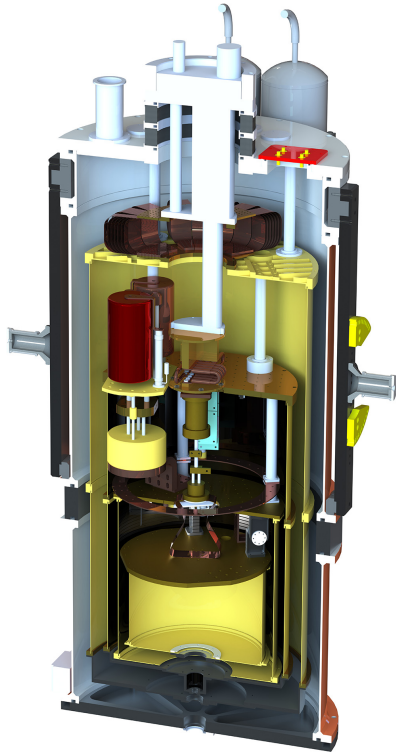


Figure 6.3: Computer-generated model of Aloysiush cryostat. Along with the various sorption pumps and heat switches the damping stages can also be seen; these are (from top to bottom) the (black) rubber rings via which the pulse tube system is mounted to the cryostat, the bent copper-shim springs, the copper braid connecting the 65 K stage of the pulse tube cooler the plate and copper shim connecting the condenser of the second ^3He sorption pump to the final cold plate.

detailed explanation of their introduction is given by Bhatia et al. (1999). In order to reduce the effect of these microphonics some form of dampening is required to reduce the force exerted on the various stages of the cryostat.

In the case of this system this has been performed via the deployment of four damping stages. Firstly, the pulse tube cooler's motor is electrical decoupled from the cryostat itself, this is performed sitting the motor on a layer of plastic and by adding PTFE spacers to the lines between the motor and the pulse tube head; on the outside of the cryostat instead on mounting the pulse tube cooler head directly

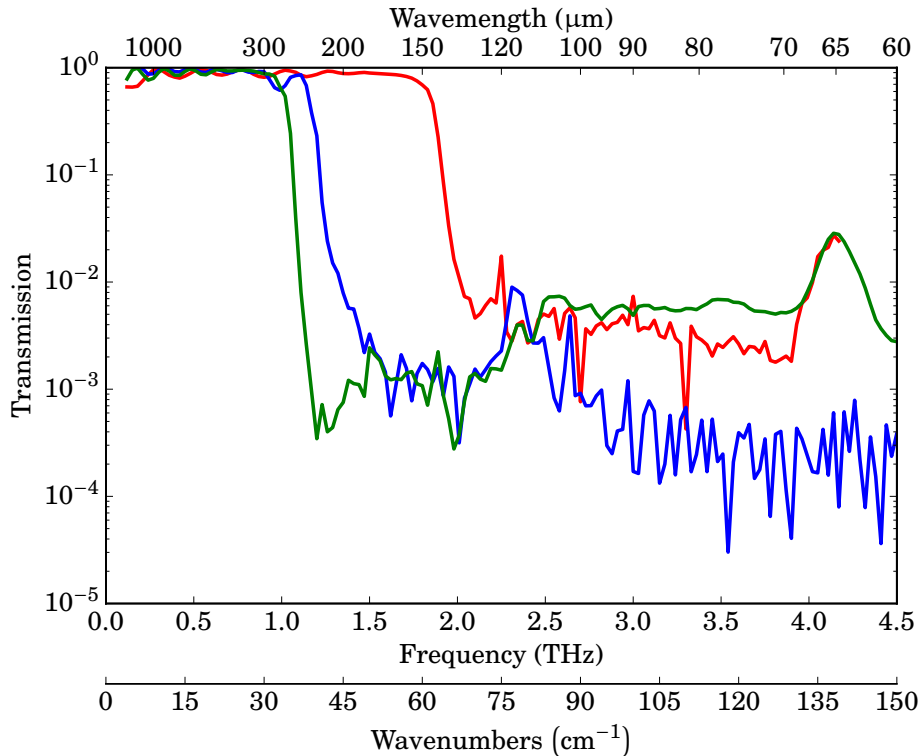


Figure 6.4: Filters mounted at various stages of the Aloysius cryostat for optical measurements. Red— 60 cm^{-1} low-pass edge filter, mounted on the 60-K shield; blue— 43 cm^{-1} low-pass edge, mounted on the 4-K shield; green— 33 cm^{-1} low-pass edge, mounted on the 350-mK shield.

to cryostat a number of rubber spacer rings (shore hardness 40) are placed between the cryostat and the head, these are sufficiently clamped to ensure a hermetic seal but allow a degree of movement to absorb some of the vibrational energy. Secondly, at the first stage of the pulse tube cooler (nominally at 65 K) the pulse tube cooler is connected to the cold plate via multiple pieces of thin-copper shim bent into a c-shape; these act like springs, dampening an vibration, while still creating good thermal link between the pulse tube cooler and the plate. At the second stage of the pulse tube cooler (nominally 3–4.2 K) a similar technique is used whereby the pulse tube cooler and the cold plate are connected via multiple strands of copper braid, this again affords a good thermal link while damping vibrations. Finally, the coldest stage of the system (that cooled by the second ${}^3\text{He}$ pump of the He10

sorption cooler) is connected to the pump via more copper shim (similar to that described earlier). All the cold plates of the system, with the exception of the coldest stage, are connected to the cryostat's outer vacuum shield by hollow stainless-steel supports with thin (compared to their length) walls. The coldest stage used rigid supports containing sapphire-sapphire contacts (these have been described by Bintley, Woodcraft, and Gannaway, 2007). A computer-generated model of this system, showing these features along with various other components can be seen in Figure 6.3.

For optical measurements in this system a set of metal-mesh filters (as described by Ade et al., 2006) were used. These not only reduced the thermal load on the colder stages of the cryostat (those with the least cooling power) but also reduced the out-of-band power on the detector (i.e. radiation with frequencies not of interest for the study being carried out). The transmission profiles of these filters can be seen in Figure 6.4. An additional band-pass filter with 3-dB bandwidth of 50 GHz centred around 150 GHz was also used. This was mounted on the front of the detector holder and is not shown in Figure 6.4.

6.4.2 LIQUID HELIUM CRYOSTAT WITH ADIABATIC DEMAGNETISATION REFRIGERATOR

The second system used to characterise Silicon Cold Electron Bolometers was a liquid helium cryostat including an adiabatic demagnetisation refrigerator. This system offered the ability to measure the current-voltage characteristics of detectors down to a bath temperature of 80 mK. The temperature of the cold plate was controlled by varying the magnetic field applied to the paramagnetic salt. Testing in this system was limited due to an inability to perform optical measurements and the high running cost associated with the system (the adiabatic demagnetisation refrigerator was housed in a medium sized cryostat and required a large amount of liquid helium in order to be cycled). This system is shown in Figure 6.5.

Not shown in Figure 6.5 is the stage upon which the device was mounted. In normal circumstances this was clamped to the 80-mK cold finger (the upper of the two gold plated rods seen emerging from the left of the aluminium support structure in Figure 6.5). Due to the magnetic fields used to thermally cycle the adiabatic demagnetisation refrigerator this stage was surrounded by a shield plated using

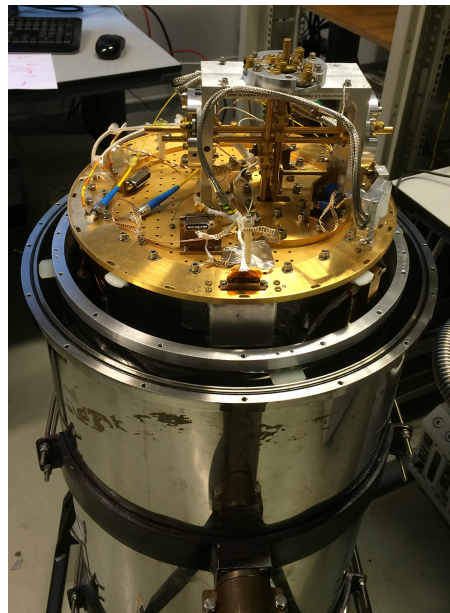


Figure 6.5: Photograph of cryostat housing the adiabatic demagnetisation refrigerator used for testing detectors. The cold fingers of the two stages of the refrigerator can be seen protruding from the top and the left of the aluminium support structure the minimum achievable temperature of these was 1 K and 80 mK respectively.

tin-lead solder (60 %, lead 40 % tin), tin-lead is a superconductor and thus expels magnetic field through the Meissner effect. In the ratio used tin-lead solder has a superconducting transition temperature of ~ 7 K, it was important that the shield is effective above the operational temperature of the adiabatic demagnetisation refrigerator's magnet to ensure that magnet fields did not become trapped within the shield.

6.4.3 LIQUID HELIUM CRYOSTAT WITH HE7 SORPTION REFRIGERATOR

The final system used for to characterise detectors was a second liquid helium cryostat, this time with a He7 sorption refrigerator. This system was used for the vast majority of optical measurements were taken, including measuring the spectral response of the detector. This system was well suited to such measurement,

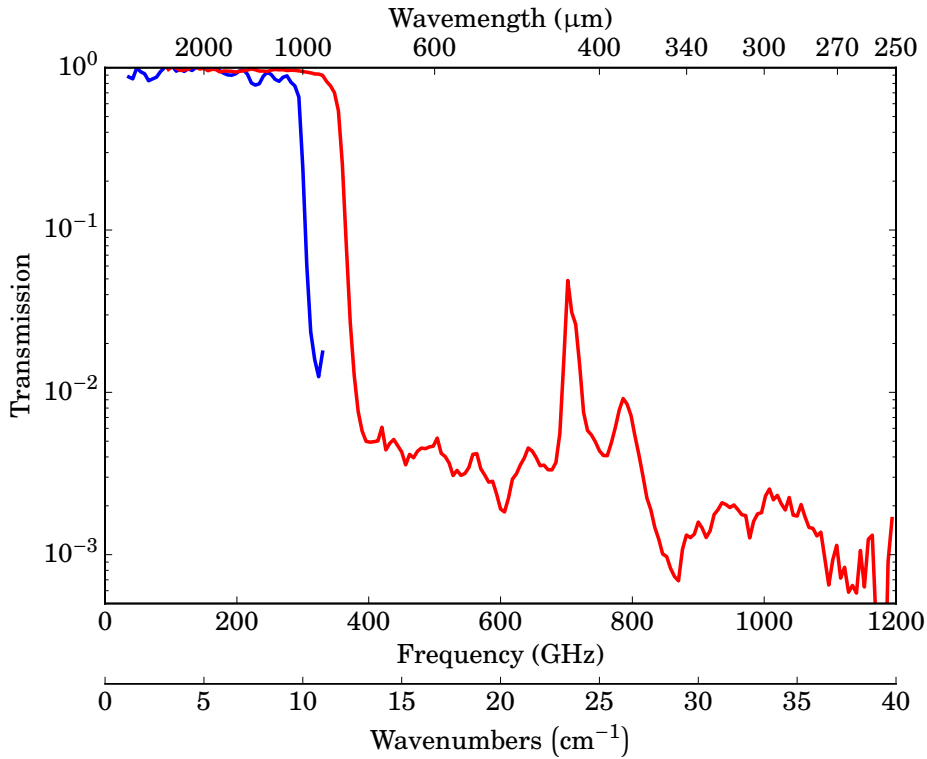


Figure 6.6: Filter profile of filters used in optical measurement cryostat. Red— 12 cm^{-1} low-pass edge filter mounted the back-to-back horns at 4.2 K; blue— 10 cm^{-1} low-pass edge filter mounted on the device holder at 350 mK. A set of thermal blockers we also used to reduce the power load on the cold stage of the cryostat; these were close to 100 % transparent at the frequencies shown and as such have not been included.

including a set of back-to-back horns produced a well defined beam of radiation at the detector stage.

As was the case with the Aloysius system, a number of filters were used to remove the out-of-band radiation, these are shown in Figure 6.6. The vacuum jacket of the cryostat contained a large (90 mm) ultra-high-molecular-weight polyethylene (UHMWPE) window. This blocked the visible and near-infrared light as well as ensuring that the vacuum was maintained. The 77-K and 4-K shield contained thermal-blocking filters; these are close to 100 % transparent in the frequency range shown in Figure 6.6 and as such the profile of these has not been plotted. In

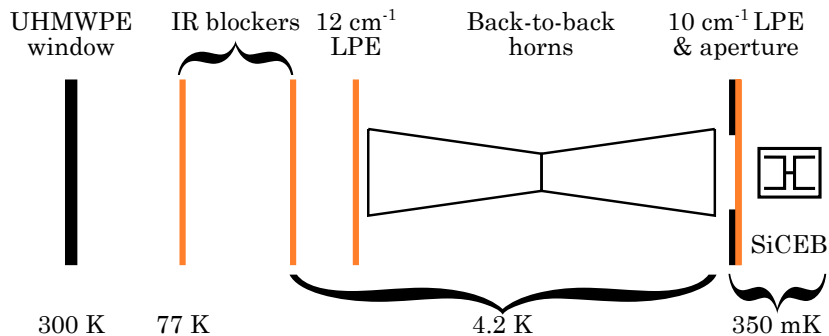


Figure 6.7: Optical components housed in cryostat used for optical measurements.

front of the back-to-back horns (at 4.2 K but after the thermal blocker) a 12 cm^{-1} low-pass edge filter was used (this is the red line in Figure 6.6). The device holder, which was mounted on the 350 mK stage of the cryostat, was fitted with a 10 cm^{-1} low-pass edge filter. No bandpass filters were used to further reduce the spectral range of the incident radiation since this would obviously prohibit any meaningful study of a detector's spectral response.

The optical key optical components in this system were a pair of back-to-back corrugated horns, these were mounted at 4.2 mK, in a shield surround the 350-mK detector stage. These back-to-back horns produced an excellent Gaussian beam with low side-lobes. This horn arrangement is very similar to that used on Planck's HFI instrument as described by Maffei et al. (2010). A simplistic schematic of the optical configuration of this cryostat is shown in Figure 6.7. A photograph of this system, in which the outer UHMWPE window can be seen, is shown in Figure 6.8.

6.5 DETECTOR HOLDER

In order for the detectors to be characterised they needed to be mounted in a holder which not only held them firmly in place but also facilitated easy electrical connections along with ensuring that only desired radiation was incident on the detector. Such a holder was manufactured in house by a computer-numerical-control mill. The holder (shown in Figure 6.9) included an aperture through which light could enter the holder for optical testing; a metal-mesh filter was clamped behind the aperture. For dark measurement the filter could be replaced by a blank.

Check if I should italicise this.

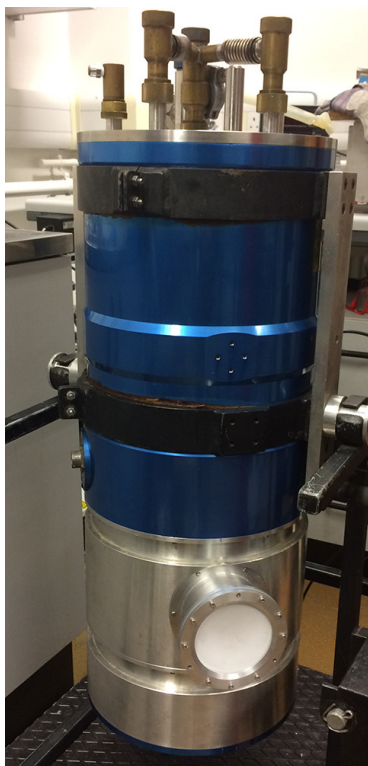


Figure 6.8: Photograph of cryostat used for optical measurements. The relatively large UHMWPE window can be seen towards the bottom of the photograph.

The various components of the holder all included a lipped edge, this ensured that the holder was reasonably light tight. A Teflon ring was used to clamp the silicon lens in place, this ring also ensured the lens was correctly aligned. A printed circuit board, wired to a micro-miniature D-type connector, allowed for simple connection to the detector holder. The electrical connection from the connector to the detector itself was completed by aluminium wire bonds between the print circuit board and the detector⁵. The detector was secured in the holder via careful glueing, with GE varnish, to a piece of silicon (matched to the lens) which in turn was glued to the rear of the circuit board. When glueing the detector to this silicon it was important to ensure that the GE varnish was only present at the edges and did

⁵The circuit board was gold plated to make the wire bonds more reliable.

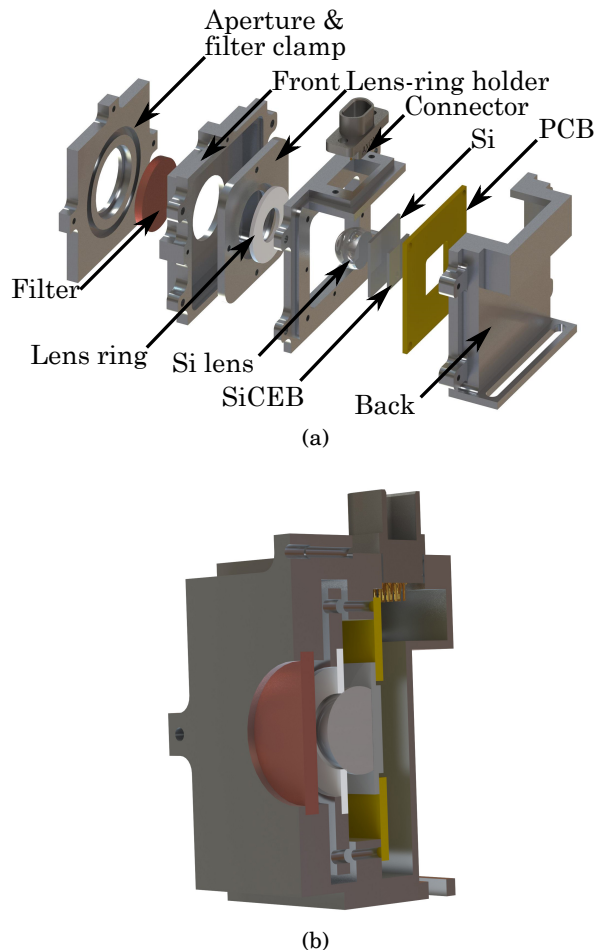


Figure 6.9: Computer-generated model of the detector holder. (a)—exploded view of the detector holder, showing the various components; (b)—cross-sectional view of the assembled detector holder.

not seep under the detector chip, since this would interfere with the radiation incident on the detector (which was rear illuminated through the silicon substrate). A computer-generated model of the device holder can be seen in Figures 6.9a and 6.9b, which show an exploded view of the various components of the holder (including the detector chip itself) and a cross section of the fully assembled holder.

Chapter Seven

Detector Readout

“The audience is the most revered member of the theater. Without an audience there is no theater.”
— Viola Spolin

7.1 INTRODUCTION

Like all high-sensitivity detectors operating in the far-infrared, cold electrons bolometers need to be readout using amplification (Rieke, 2007). Amplification is of either the voltage or the current, with the quantity not being amplified for readout usually providing the bias. Golubev and Kuzmin (2001) provide a good discussion of the advantages and disadvantages of current-bias versus voltage-bias for use with Cold Electron Bolometers (CEBs), along with a basic schematic for each case.

In reality the Superconducting Quantum Interference Devices (SQUIDs) and their associated electronics used to amplify current in a voltage bias regime are both more expensive and more complex to setup compared to the voltage amplifiers used for current biased measurements. This means that it is often preferable to use a current biased system for early device development.

During the development of Silicon Cold Electron Bolometers (SiCEBs) numerous iterations of voltage amplifier have been used. Each readout system was designed to offer the possibility of improved device characterisation, from either a

lower contribution to the noise measurement or by allowing measuring to higher frequencies of readout.

In addition to changes that were required to the amplification system it has also been necessary to change the exact technique by which the detector has been biased. The main driver for these changes has been the desire to reduce electrical noise input to the device as well as to create the most stable and capable testing regime possible.

7.2 REQUIREMENTS OF THE READOUT SYSTEM

In order to specify a readout system it is important to define a number of desirable goals for its performance. For the early development stage testing of CEBs the following desired points were set:

- The system had to be as simple as possible. This is to say that the design and operation of the readout should not become a distraction from the testing of devices.
- The system needed contribute a sufficiently low electrical noise that noise measurements of the detector could be successfully performed.
- The system was capable of measuring the speed of response of the detector by measurement of the roll-off of device noise.

Although it was possible to estimate both the speed and expected noise levels for a CEB, these estimates were only vague ‘ball-park’ figures. This meant that it was necessary to produce an testing system believed to be capable of meeting these criteria and then to make improvements as required. Further to these requirements any system needed to be able to perform DC-measurements, such as recording IV curves with a high degree of stability.

7.3 INITIAL TESTING SYSTEM

7.3.1 INITIAL READOUT SYSTEM

The initial amplification system used was heavily based upon an existing circuit designed to readout Resistance Temperature Detectors (RTDs). This was used as

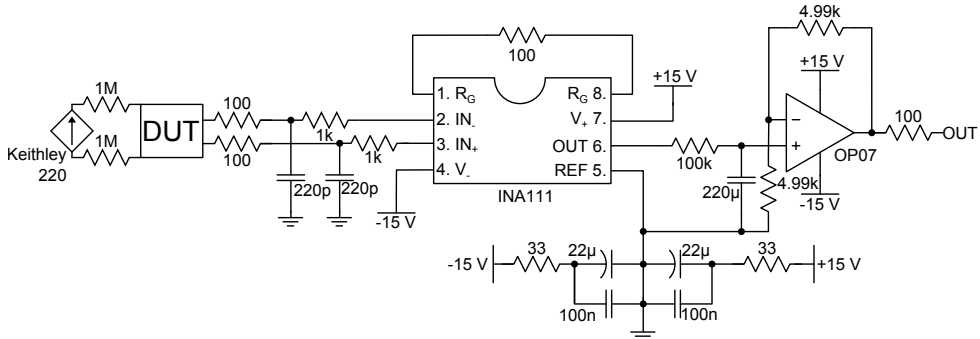


Figure 7.1: Initial bias and readout system using a Keithley 220 programmable current source to bias the device under test (DUT). The voltage is then amplified by the INA111 differential amplifier (configured for a gain factor of 500) and then by the OP07 operational-amplifier (configured to give a gain of two).

it was readily available within the department and early (somewhat optimistic) estimations of device performance indicated that noise measurements would be possible. This amplifier was used in conjunction with a Keithly 220 Programmable Current Source to provide the bias across the device. Figure 7.1 shows the circuit diagram of the amplifier used here along with the connection of current source. To perform an IV measurement the current source, which is controlled by a computer, is stepped through the desired range of values and at each step a data acquisition unit (DAQ) records the amplified voltage across the device.

The *INA111 Data Sheet* (2010) and *OP07 Data Sheet* (2011) state that both these amplifiers have, when operating in the configuration shown in Figure 7.1, a noise voltage, referred to the input, of $10 \text{ nV}\text{Hz}^{-\frac{1}{2}}$. In order to understand how the internal noise of these amplifiers contributes to the total noise measured at the output of the system we can think of each of the two amplifiers as containing some source which generates a noise voltage with a spectral density of e_n and some *black-box* which provides the gain while generating no noise. This is illustrated in Figure 7.2.

In Figure 7.2 we see that if there is no input signal at point I then the input to the second amplifier, point A, will consist of only the noise generated in the first amplifier, multiplied by that amplifier's gain factor. The, uncorrelated, noise from the second amplifier is then added to the amplified noise from the first and both

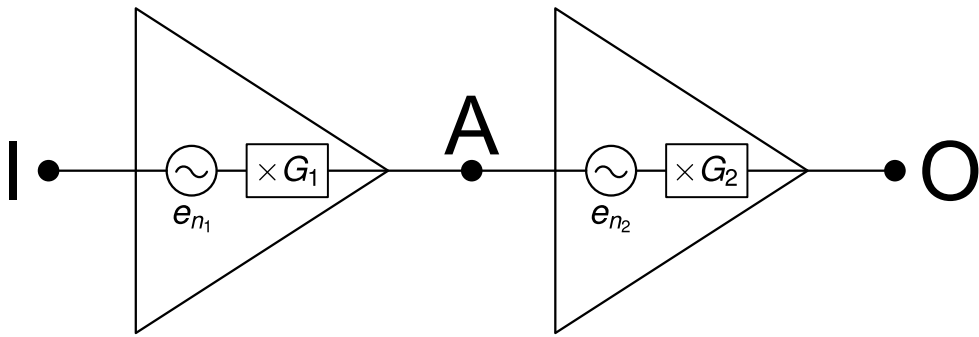


Figure 7.2: Simple model of two amplifiers working in series. Each amplifier contains a component which generates a noise voltage with spectral density e_n before an ideal, noiseless, component amplifies the signal by a gain factor of G .

are multiplied by the gain of the second amplifier. From this we can define the total noise, e_{tot} , at the output of this system, in the absence of any input signal, as:

$$e_{tot} = \sqrt{(e_{n_1} \times G_1)^2 + e_{n_2}^2} \times G_2. \quad (7.1)$$

If, as is the case in Figure 7.1, $e_{n_1} \times G_1 \gg e_{n_2}$ then we can say:

$$e_{tot} \approx e_{n_1} G_1 G_2. \quad (7.2)$$

We can define the input referred noise voltage spectral density, e_{RTI} , simply as:

$$e_{RTI} = \frac{e_{tot}}{G_{tot}}, \quad (7.3)$$

where G_{tot} is the product of the various gain stages, given by:

$$G_{tot} = \prod_n G_n. \quad (7.4)$$

By applying Equation 7.1 for the system shown in Figure 7.1 ($e_{n_1} = e_{n_2} = 10 \text{ nVHz}^{-\frac{1}{2}}$, $G_1 = 500$ and $G_2 = 2$) we find that $e_{RTI} = 10.00002 \text{ nVHz}^{-\frac{1}{2}}$. The above approximation can be verified by calculating e_{RTI} again using Equation 7.2, this gives $e_{RTI} \approx 10 \text{ nVHz}^{-\frac{1}{2}}$. This shows that in this case the internal noise from the second amplifier is contributing only 0.0002 % of the noise at the output.

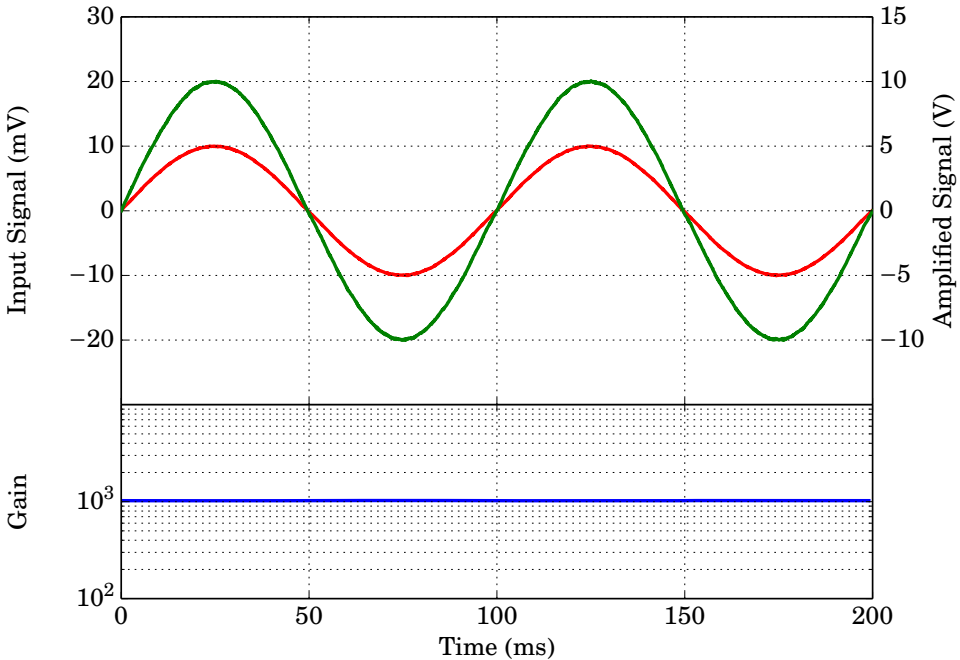


Figure 7.3: Gain measurement of RTD amplifier using a 10 Hz sinusoidal wave. Upper plot – Input signal (red, primary vertical axis) compared to the amplified signal (green, secondary vertical axis). Lower plot – Gain measured from taking the ratio of the amplified and input signals.

It is possible to characterise the amplifier by measuring three simple parameters, the amplifier's: gain, bandwidth and internal noise. The gain can be found by measuring how much a signal, a simple sinusoidal wave for example, is amplified; the bandwidth of the amplifier can be found by measuring the frequency at which the noise spectral density decreases from $e_{tot}G_{tot}$ (this can also serve as a measure of the uniformity of the gain across a wide range of frequencies). Finally the internal noise (referred to the amplifiers input) can be found from the noise spectral density, corrected for the measured gain, when the input of the amplifier is shorted (no input signal).

Figure 7.3 shows the amplification of a 10 Hz sinusoidal wave generated by a signal generator, the output of which was split between the amplifier to be tested and a direct input to a digital oscilloscope. The input signal (red, shown on the

primary vertical axis of the upper plot of Figure 7.3) was measured to have a peak amplitude of 10 mV ($V_{rms} = 7.07$ mV). The amplified signal (green, secondary vertical scale) was measured as having a peak amplitude of 10 V ($V_{rms} = 7.07$ V), from this it is clear the gain factor of the amplifier is 1000 at the voltage peaks. The uniformity of the gain, for various input amplitudes, was verified by simply taking the ratio of these two signals at all points, the result of this is shown in the lower plot of Figure 7.3, from this it is clear that the gain factor of 1000 does not vary with the amplitude of the input signal (up to 10 V). The (INA1112010) states that the input amplitude range (the range over which the input is amplified by a constant gain) of this device is 12.7 mV when operating at a gain of 1000.

The next stage in characterising this amplifier was to measure the bandwidth, in frequency, over which a signal is consistently amplified. This was performed by using a signal generator to output a white noise signal¹ of known amplitude. Similarly to the previous test this signal was then split with one output being passed directly to a digital oscilloscope and the other being amplified before being passed to the oscilloscope. The digital oscilloscope was also used to process both of these signals by computing the Fast Fourier Transform (FFT) of both. When defining the frequency bandwidth of an electronic device it is usual to take the frequency that the voltage throughput has fallen to a factor of the square root of two times the maximum throughput. This is called the 3-dB bandwidth since:

$$20\log_{10}\left(\frac{1}{\sqrt{2}}\right) \approx -3 \text{ dB.} \quad (7.5)$$

More correctly the 3-dB bandwidth is defined as the frequency at which the power throughput has fallen by a factor of one half, i.e.:

$$10\log_{10}\left(\frac{1}{2}\right) \approx -3 \text{ dB.} \quad (7.6)$$

Figure 7.4 shows the result of the bandwidth measurement. It is clear from the figure that at frequencies below 10 kHz the output of the amplifier (green trace on upper plot) differed only from the generated noise (red trace on upper plot) by the gain factor of 1000. As the frequency increased the gain factor (blue trace on lower plot) ceased to be constant and started to decrease. Using Equation 7.5, the 3-dB

¹The Agilent 33220A Function / Arbitrary Waveform Generator Data Sheet (2011) states that this device has a bandwidth, when generating noise, of 9 MHz.

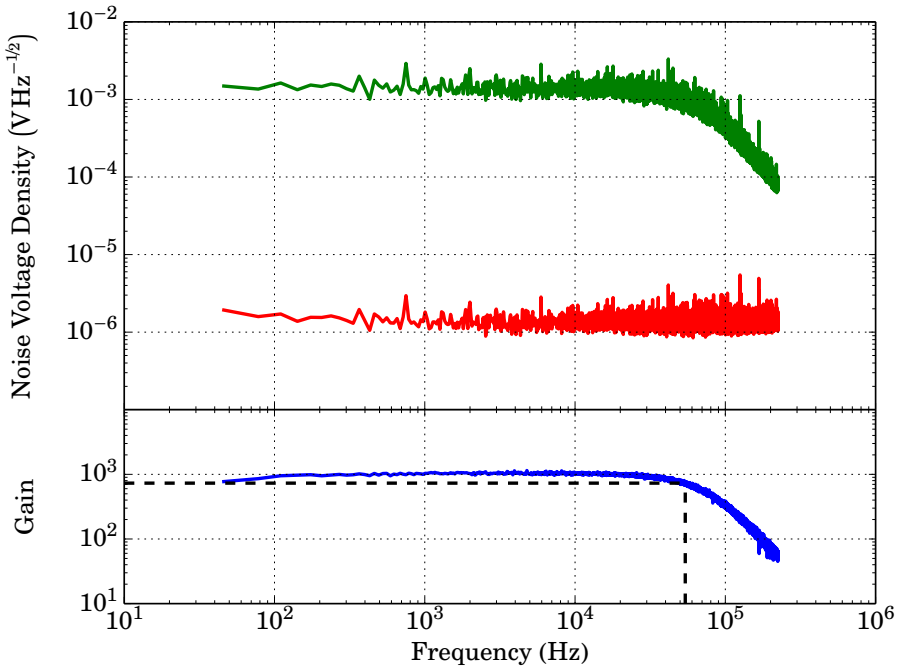


Figure 7.4: Bandwidth measurement of RTD amplifier. A white noise signal was generated by a signal generator, this was split with one feed being fed directly to the oscilloscope (red line) and one feed being amplified first (green line). The ratio (the gain of the amplifier) is shown on the lower plot the 3 dB level and corresponding frequency limit to the bandwidth are shown by the dashed line in the lower plot.

bandwidth corresponds to the gain dropping to 731; this occurred at a frequency of 55 kHz, this is illustrated by the dashed line on the lower plot of Figure 7.4.

The final part of characterising the amplifier was to measure the input referred noise. As seen earlier in this section for the configuration of this amplifier (shown in Figure 7.1) the expected input referred noise was $10 \text{ nV}\text{Hz}^{-1/2}$ (explained on Page 84). To measure this quantity the input of the amplifier was shorted and the output of the amplifier was measured as in the previous tests.

Figure 7.5 shows the measured noise spectrum for the amplifier (as referred to the input), measured up to 10 kHz. From this figure we can see that the internal noise is equivalent to a noise source of $10 \text{ nV}\text{Hz}^{-1/2}$ at the input of the amplifier.

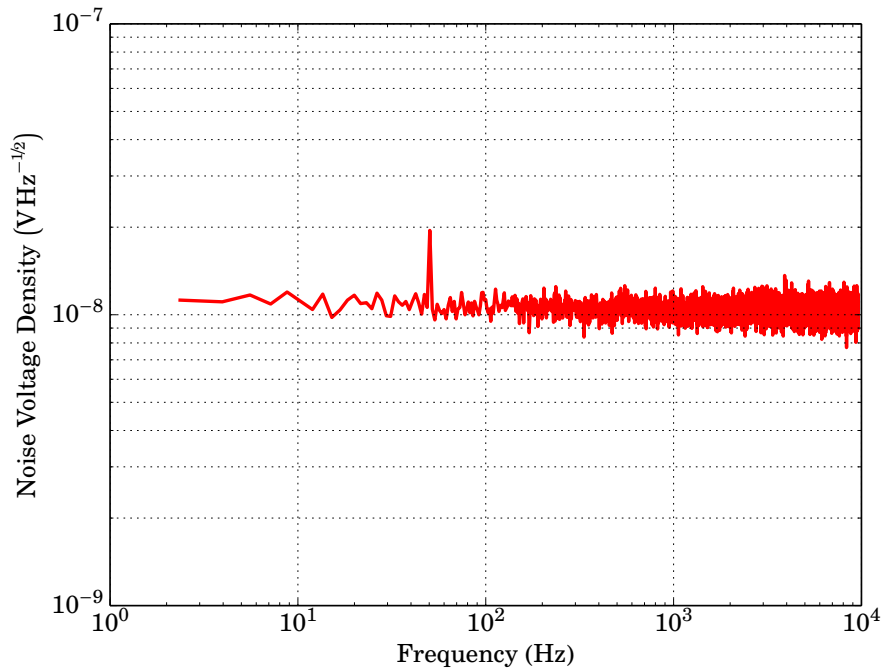


Figure 7.5: Measurement of the internal noise of the original amplifier, referred to the input of the amplifier. The measurement was performed by shorting the input of the amplifier and measuring the output of the amplifier with a digital oscilloscope, which also computed the FFT.

This is the value which was predicted on Page 84 and this result, along with the results of the other tests carried out thus far, indicated that the amplifier system was performing as designed.

7.3.2 INITIAL BIAS SYSTEM

The amplifier only contributes one part to the total performance of the electronic system. The source of biasing current also plays a substantial role in the final performance. Unlike the amplifier the speed or bandwidth of this current source not of high importance since the IV measurements can be performed at a low frequency and noise measurements are measured with the device at a constant (DC) bias. The bias circuitry can however have a negative effect on measurement by either

failing to provide a stable bias and thus causing some degree of *jitter* in a measurement or by adding undesired level of noise (either as white noise or as finite tones). In the case of the current supply contributing additional noise, this could in-turn cause additional energy to be dissipated across the device being tested and thus affect the result.

In the first system used the current bias was provided by a Keithley 220 Programmable Current Source, this unit is capable of providing currents between 500 fA and 100 mA with a peak to peak noise level of between 400 ppm and 100 ppm depending on the output range specified².

In order to test the effect of the current source two simple measurements were performed using a *dummy* device (typically a resistor with an appropriate value) as the DUT in Figure 7.1³. Firstly, a test was carried out to ensure that the output of the device was stable enough to all for reliable measurements. This was performed in two parts: initially the Keithley 220 current source was set to a constant value (specifically 10 μ A) and the voltage across the *dummy* device (a 1 k Ω resistor) was measured multiple times using a reliable DAQ; after this the current across the resistor was increased in steps through a defined range and the voltage across the DUT was measured for each step. These tests were selected as they closely resemble the tests which were to be performed on the eventual SiCEB devices.

Figure 7.6 shows the measured jitter of a signal caused by the Keithley 200 unit. The signal varied around expected value of 10 mV by up to 550nV. The signal was measured by a trusted data acquisition system using shielded cables. This variation is equivalent to a peak-to-peak noise level of 110 ppm. The *Keithley 220 Programmable Current Source Data Sheet* (2009) states that when outputting a current of 10 μ A the expected peak-to-peak noise level is 100 ppm, although this is slightly lower than the measured value and thus indicates either an additional noise source or an issue with the unit, the measured jitter was still sufficiently low for preliminary measurements.

There are several possible reasons for the small amount of additional jitter measured in this test. Both the Keithley 220 unit used and the triaxial cables

²The full specifications of Keithley's 220 current source are stated in the *Keithley 220 Programmable Current Source Data Sheet* (2009).

³The 1 M Ω resistors shown in Figure 7.1 were used offer protection to sensitive detectors and were not included in this test.

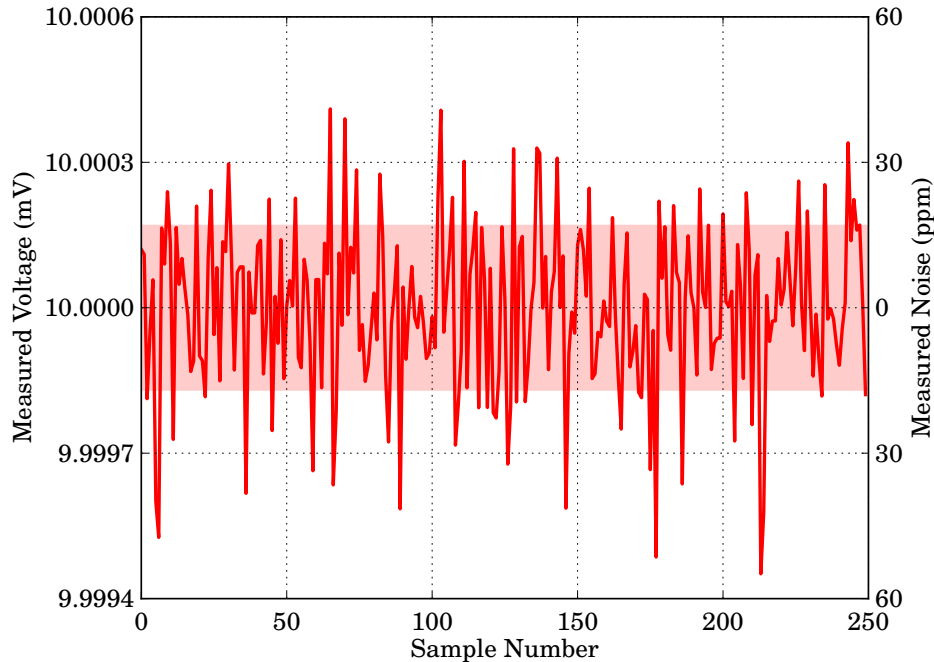


Figure 7.6: Jitter in a measurement caused by current supplied by a Keithley 220 Programmable Current Source. The current source was set to output a constant current of $10 \mu\text{A}$ which was driven across a $10 \text{ k}\Omega$ resistor. Multiple measurements were made with a trusted data acquisition system. The primary vertical axis shows the voltage measured across the resistor in each measurement (the expected voltage was 10 mV); the secondary vertical axis shows the jitter or noise about the expected value in terms of noise parts per million; the shaded region shows the standard deviation of the noise about the expected value.

used as interconnects between the current source and the device under test were several years old and it is entirely possible that a number of small breaks were present in either the cable's inner guard layer or the insulator, this could cause current to be lost between the inner-most conductor and the outer-most shield layer and thus for current to be lost between these two. The age of the unit may also have meant that some of the internal components had degraded and were no longer working within their original specification. It is most likely that a combination of these factors caused the additional noise measured. It is also possible

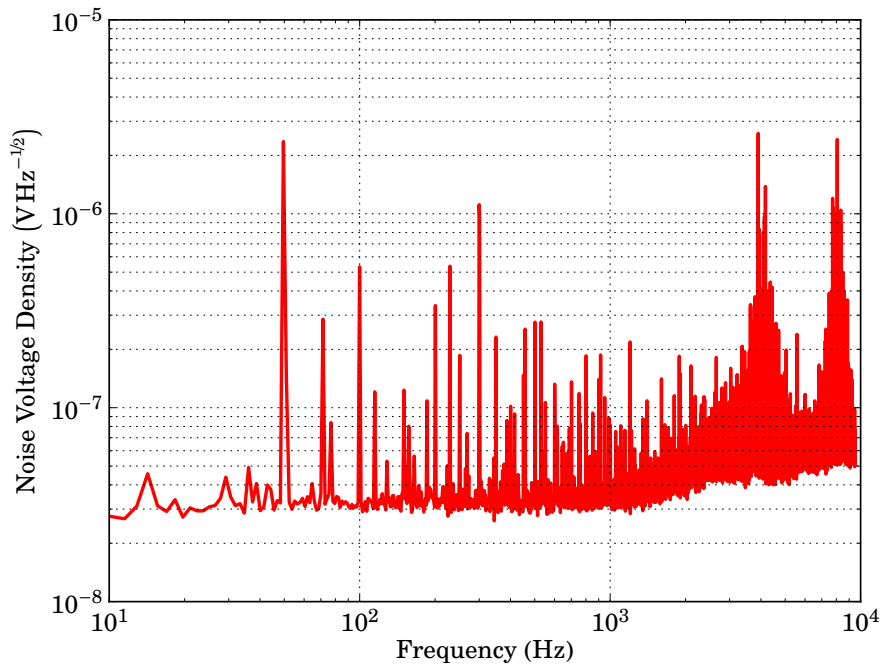


Figure 7.7: Noise spectrum measured across a resistor which was biased by the Keithley 220 Current Supply. A current of $10 \mu\text{A}$ was driven across the resistor and the voltage (and noise spectrum) was measured using a digital oscilloscope. It was expected that noise spectrum would be dominated by the amplifier noise of $10 \text{nV}\text{Hz}^{-1/2}$, it is clear that this measurement shows a white noise level greater than this and is dominated by several other sources.

that the degrading of the interconnecting cables could have made the system more susceptible to electromagnetic pickup.

The noise voltage spectrum measured across the resistor is shown in Figure 7.7, this did not resemble the *clean* spectrum seen in Figure 7.5, instead there was a substantial tone, due to mains pickup, seen at 50 Hz, along with several harmonics of this tone there were various other noise sources evident include two large clusters of tones at 4 & 8 kHz. This large clusters of noise tones were of particular concern as they indicated that in addition to the desired DC biasing signal, there could have been a substantial amount of power dissipated in the device

under test from these sources. The cause of this noise was confirmed by repeating the measurement across the resistor having disconnected the current supply. The result of this closely resembled that shown in Figure 7.5 and showed that the noise was due to the presence of the current supply. By disconnecting the interconnecting triaxial cable from the current supply, while leaving it attached to the device under test, it was found that the two clusters of high frequency tones were no longer present, this indicated that these were due to internal components within the current supply unit. However, many of the lower frequency tones remained, these were attributed to electromagnetic pickup in the cable. This result meant that the Keithley 220 Current Supply would not be appropriate for use when carrying out noise measurement since there was sustainably contamination of the signal.

7.4 REVISIONS TO THE INITIAL BIAS SYSTEM

7.4.1 CHANGES MADE AND ADVANTAGES

As was found by the test described in the previous section, the Keithley 220 current source was not appropriate for noise measurement since the was substantial contamination (at AC frequencies) of the biasing signal from both electromagnetic pickup and the issues within the unit itself. To address this a simply circuit was constructed which generated a controlled differential signal, which had an amplitude determined by a controllable input signal. This signal could then be converted to a biasing current via a pair of resistors and the resulting current was found using Ohm's Law, measuring the voltage dropped across these biasing resistors.

There are several advantages to housing the biasing unit inside the casing of the amplifier, which during device testing was directly mounted to a cryostat. Firstly, since no interconnecting cabling was required, the possibility of electromagnetic pickup was greatly reduced. Secondly, due to the close physical proximity of the amplifier and the current supply it was possible to have greater control over the grounding of these two components and thus remove any ground loops which could have offset a measurement or contributed to the total noise measured, further to this since the biasing signal was now sent using a differential connection there was no connection to ground across the device under test is fully isolated

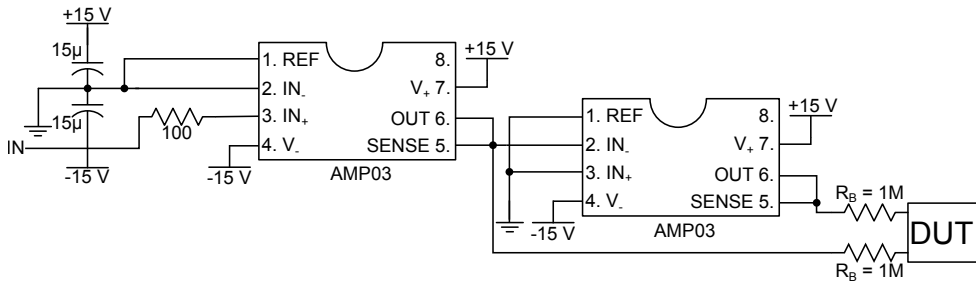


Figure 7.8: Circuit diagram for the custom made internal bias generator used with the first amplifier. A single ended input was fed to the non-inverting input of a unity gain amplifier, the output of this amplifier was split with one feed being supplied to the inverting input of a second unity gain amplifier. The output of this amplifier, along with that of the first, was then used to bias the device under test via a pair of biasing resistors.

from any possible ground loops or other contamination from the ground line. Finally, since the amplitude of the current was not directly controlled by the bias generator but instead is governed by an external source, it was possibly to produce a smooth range of currents, as opposed to Keithley unit which was only able to step current, all be it in relatively small steps.

The bias generator worked by using two unity gain amplifiers to generate a differential biasing signal, V_{bias} , from a single-ended input. The input was fed into the non-inverting input of the first amplifier, the output of this was equal, in amplitude, to the input signal and was then split with one feed connected to the inverting input of the second amplifier. The output of the second amplifier was again equal in amplitude to the input signal but had the opposite sign, the output of this amplifier along with that of first amplifier served as the biasing voltage. This biasing voltage, V_{bias} , formed a differential signal and was given by:

$$V_{bias} = V_+ - V_-, \quad (7.7)$$

where V_+ and V_- are the outputs of the first and second amplifiers respectively. Since, in the this case, the outputs of these amplifiers were $V_+ = +V_{in}$ and $V_- = -V_{in}$, the final biasing voltage was given by:

$$V_{bias} = 2V_{in}. \quad (7.8)$$

The biasing current, I_{bias} , across the device under test is the same as the current through the two biasing resistors, which from Ohm's Law is given by:

$$I_{bias} = \frac{V_R}{2R_{bias}}, \quad (7.9)$$

where V_R is the voltage dropped across the two biasing resistors. By measuring the voltage across the device under test, V_{DUT} , and from knowing the voltage generated by the bias circuitry, the voltage dropped across the biasing resistor was given by:

$$V_R = V_{bias} - V_{DUT}. \quad (7.10)$$

By using the result of Equation 7.8 the above can be written as:

$$V_R = 2V_{in} - V_{DUT}. \quad (7.11)$$

Finally combining this with Equation 7.9, the biasing current can be calculated by:

$$I_{bias} = \frac{2V_{in} - V_{DUT}}{2R_{bias}}. \quad (7.12)$$

There were further advantages of this biasing regime, offered by the fact that the system now used a differential signal to bias the device under test. Since the device under test was now isolated from the ground line, which is often a source of signal contamination. This regime also offers a dramatic reduction in the effect of electromagnetic pickup. Since this differential bias generator produced two signals of equal and opposite voltage and since noise due to electromagnetic pickup would have added to both, this meant that the difference between the two signals, at any given time, remained the same and the output of the final amplifier, which only depended on this difference, was not affected. In terms of differential signals a change which maintains the same difference between the two signals is referred to as a common-mode, when the difference between the two is affected there is said to be a normal-mode. This concept is illustrated in Figure 7.9.

7.4.2 PERFORMANCE OF UPDATED BIAS SYSTEM

In order to ascertain whether or not this current generator offered improved performance over the Keithley 220 the same test, which were described in Section 7.3.2,

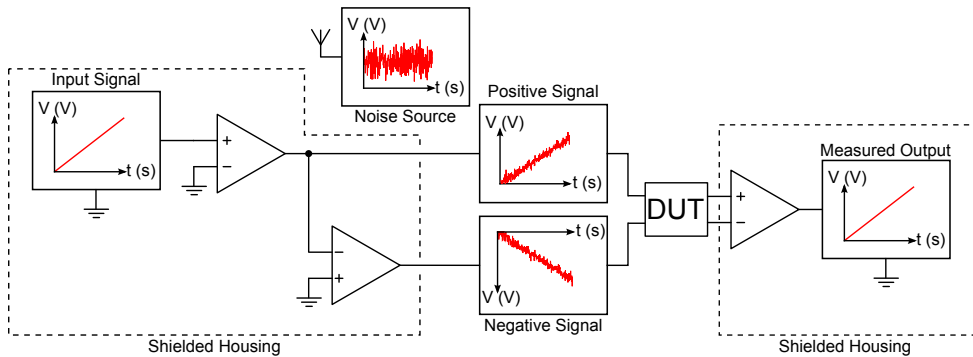


Figure 7.9: Rejection of common-mode noise in a differential signal bias and readout system. The two amplifiers which make up the differential signal generator produce two signals which are equal and opposite to each other and related in magnitude to the input signal. This is then carried, by a pair of wires, through an unshielded environment. Any electromagnetic pickup adds to both of these signals as a common-mode, this does not affect the difference, in amplitude, between the two signals and thus is not measured by the final differential amplifier.

were repeated with the new system. Of particular interest were the results of measuring the noise spectrum produced by this system.

Figure 7.10 shows the jitter measured for current generator which replaced the Keithley unit. The measured peak-to-peak jitter for this system was 200 ppm which corresponded to a maximum variation of $1 \mu\text{V}$ from the expected value. While this value is approximately twice what was measured in Section 7.3.2 for the Keithley unit (illustrated in Figure 7.6), the level was still deemed to be acceptable for IV characterisation.

The noise spectrum measured across a resistor, biased using the newer current generator, is shown in Figure 7.11. When compared to the corresponding measurement in Section 7.3.1 for the Keithley 220 (Figure 7.7) it is noted that the noise spectrum measured here is much cleaner; there are far fewer noise tones present and the two clusters of tones seen at higher frequencies in Figure 7.7 are no longer present, in fact the only undesired feature present within the spectrum is a noise tone at 50 Hz, this was due to the 50 Hz variation of the mains power. The white noise level measured in this test was $10 \text{ nV}\text{Hz}^{-1/2}$ compared to a minimum value of $30 \text{ nV}\text{Hz}^{-1/2}$ (rising to over $70 \text{ nV}\text{Hz}^{-1/2}$) for the Keithley unit. In fact when

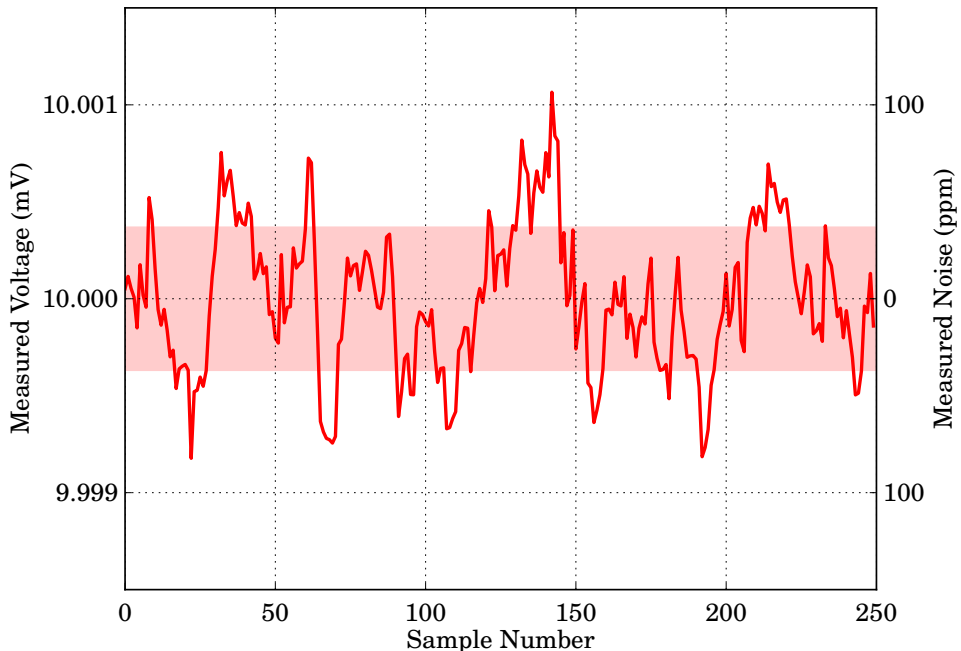


Figure 7.10: Jitter measured from custom made current bias generator. The input voltage to the system was set such that a current of $10 \mu\text{A}$ flowed through the $1 \text{k}\Omega$ resistor (which took the place of the device under test). The voltage across the resistor was measured using a trusted data acquisition system. The primary vertical axis shows this voltage (which was expected to be 10 mV); the secondary vertical axis shows the jitter or noise about the expected value, in terms of noise parts per million; the shaded region shows the standard deviation of the noise about the expected value.

the noise spectrum shown in Figure 7.11 is compared to the measurement made with the input of the amplifier shorted (Figure 7.7) it is clear that the two compare extremely favourably. This showed that this measurement was limited by the internal noise generated by the readout amplifier (as shown in Section 7.3.1).

From these tests it was clear that the revised biasing system offered a notable overall improvement when compared to the Keithley 220, despite there being a decrease in the stability of the bias signal produced, the improvements to noise spectrum, and the resulting reduction in unwanted power dissipated across the

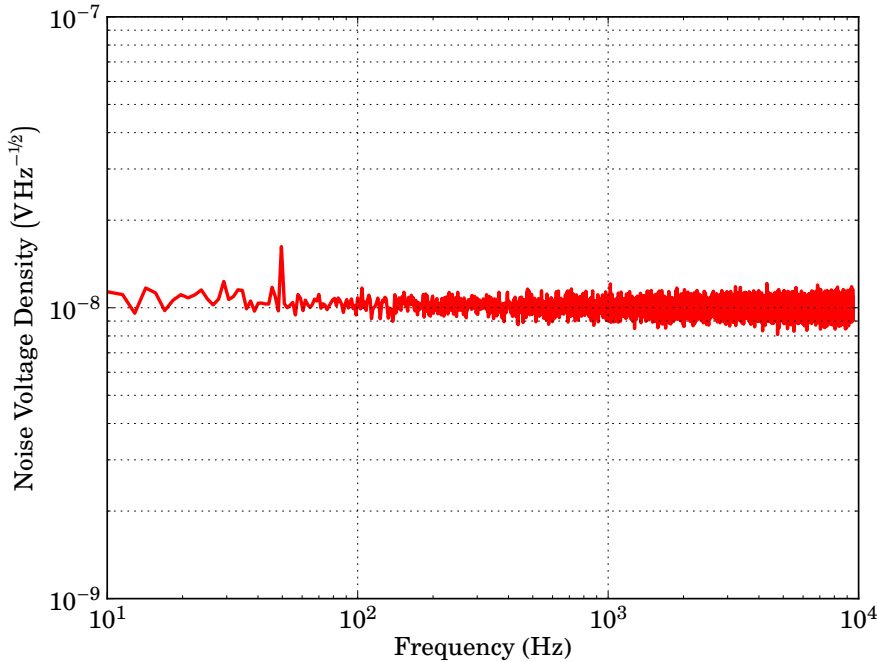


Figure 7.11: The noise spectrum measured across a $1\text{ k}\Omega$ resistor biased using the custom made bias generator. When compared to the spectrum measured using the Keithley 220, shown in Figure 7.7, it is clear that the newer system showed very little contamination of this signal.

device under test, meant that this system was used for the preliminary testing of CEB devices.

7.5 FINAL TESTING SYSTEM

7.5.1 REASON FOR REPLACEMENT

Despite having reached a stage where the initial readout system was performing as well as could have been expected of it, it became clear, as testing of devices progressed, that its limitations were prohibiting the full characterisation of devices. When compared to list of desirable features for the readout system (as defined in

Section 7.2) neither the second nor third points were met. That is to say that measurements of noise spectra were limited by the amplifiers own internal noise and that the amplifier did not offer sufficient bandwidth to allow the speed of response of a detector to be measured.

For these reasons it was decided to replace the initial readout amplifier and bias generator, which had been constructed from non-optimised components and designs already existing within the Department, with a new specifically designed system. This system would continue to offer a bias generator similar to the one described in Section 7.4.1 but with the added feature of being able to internally generate the voltage input to the bias generator, this feature was desired to offer an ultra-low noise DC bias, all be it at the slight cost of functionality.⁴

7.5.2 FINAL READOUT SYSTEM

Figure 7.12 shows the amplifier used for the final stages of testing Silicon Cold Electron Bolometers. The main amplification was performed by a INA103 chip manufactured by Texas Instruments. However, in order to provide a low-impedance input to the amplifier, as well as isolating the device under test from the amplifier circuitry, a matched pair of junction field effect transistors (JFETs) were used to create a differential source follower to act as the input of the amplifier.

One disadvantage of this configuration was that the addition of the JFET source followers was that a offset voltage was added to the input of the amplifier. As explained by Horwitz and Hill (1989, chap. 2) this is the result of inconsistencies in the current produced by a given voltage across the gate and source of the JFET. The reason for these inconsistencies is due to this parameter being poorly controlled in the manufacture of JFETs. This could have been addressed by including a second JFET, matched to the existing JFET, that acted to vary the source voltage to the first JFET such that there would have been no voltage offset at the output (which would have been at the drain terminal of this second JFET). This modification was not however applied since the differential input to the amplifier already necessitated the two JFETs be matched and the increase to quad-matched JFETs was prohibitively expensive for a non-critical improvement.

⁴Since this ultra-low noise level was only required when measuring noise spectra, the system could still be used in a way similar to the method described in Section 7.4.1 without any loss of functionality.

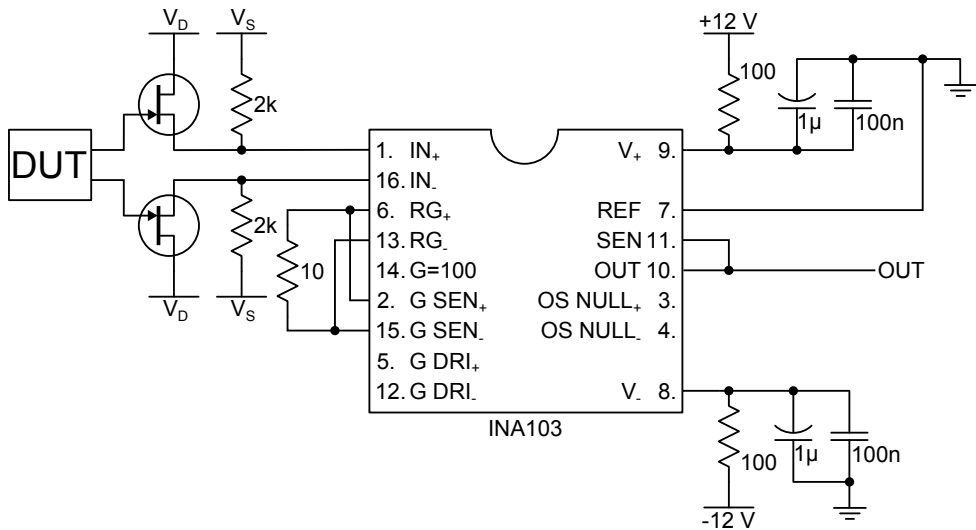


Figure 7.12: Final amplifier used for measuring voltage across devices. As opposed to the previous system (Figure 7.1) only one amplifier stage was used, the Texas Instruments INA103 amplifier, which was configured to offer a gain of 600. In addition to the amplifier a matched pair of JFETs were used as a source follower. This improved coupling to the amplifier by offering a low output impedance. It also isolated the amplifier from the device being measured, thus resulting in a lower noise level.

The preliminary testing had indicated that the previous amplifier's gain of 1000 was possibly excessive. To this end it was decided that a lower gain, of approximately 600, would be used in this case. The *INA103 Data Sheet* (2000) does not provide a table of the required resistance across the gain setting pins to achieve this value, there is however the equation for the gain, G :

$$G = 1 + \frac{6000}{R_G}, \quad (7.13)$$

where R_G is the value of the gain setting resistor required to achieve a gain of G . Thus the value of the resistor required for a gain of 600 could be found as:

$$R_{G=600} = \frac{6000}{600 - 1}, \quad (7.14)$$

$$R_{G=600} \approx 10. \quad (7.15)$$

As had been performed for the previous amplifier (Section 7.3.1), a sinusoidal signal was split with one feed supplied to the input of the amplifier and the other,

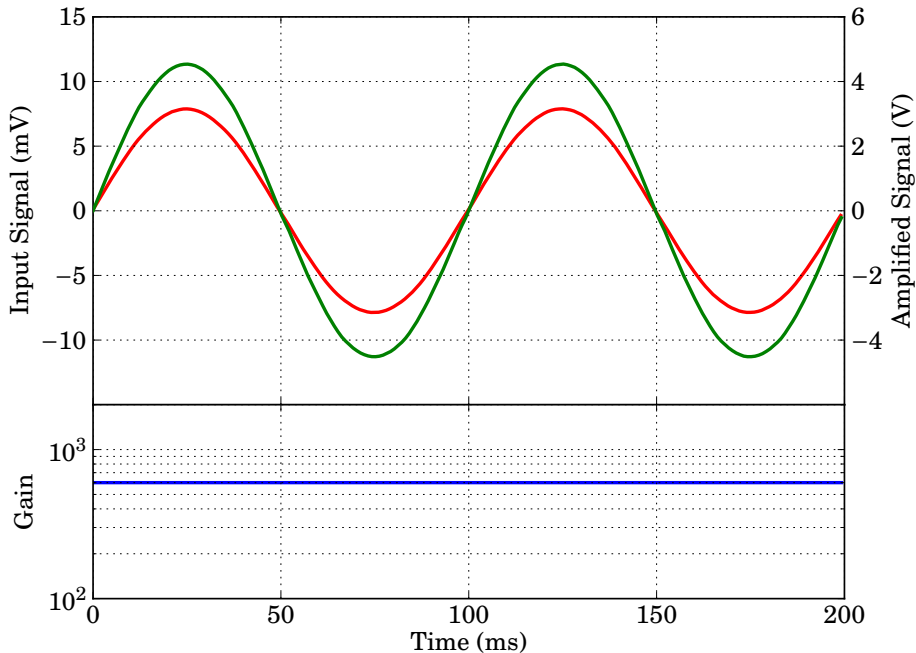


Figure 7.13: Gain measurement for the amplifier used in the final test of Silicon Cold Electron Bolometers. As in Section 7.3.1, a 10 Hz sinusoidal signal was supplied to the input of the amplifier and the output measured. Upper plot – Input signal (red, primary vertical axis) compared to the output of the amplifier (green, secondary vertical axis). Lower plot – Gain measured from the ratio of the output and input signals.

along with the output of the amplifier, measured using a digital oscilloscope. The gain of the amplifier could then be calculated by simply taking the ratio of these two. The results of this measurement are shown in Figure 7.13 where it can be seen that, for an input signal with an amplitude of 7.5 mV, there is uniform amplification at all amplitudes and the gain factor was 600.

The addition of the JFET source followers caused a further complication with this amplifier. Figure 7.14 show what happened when the amplitude of the input signal to the amplifier was increased above the 7.5 mV illustrated in Figure 7.13. In Figure 7.14 it is clear that there is a lower limit to the output voltage (green line shown on the secondary vertical axis) of approximately -4.5 V. In order to

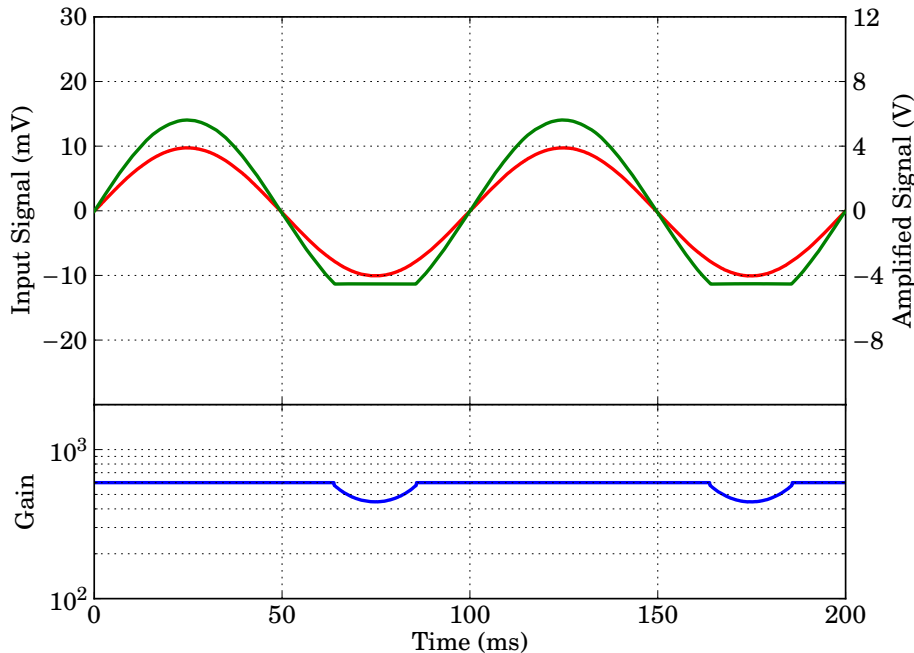


Figure 7.14: When the input to the final amplifier was increased above an amplitude of 7.5 mV an asymmetric response was noted. While positive signal continued to be amplified, by a gain factor of 600, the negative signal with the same magnitude became limited to a certain minimum value. Upper plot – Input signal (red, primary vertical axis) compared to the output of the amplifier (green, secondary vertical axis). Lower plot – Gain measured from the ratio of the output and input signals.

understand the origin of this limit and any significance it might have had on testing it is important, as always, to fully understand how these data were collected. As has already been mentioned the presence of the JFET source followers resulted in an (undesired) DC voltage offset to the input of the INA103 amplifier. When measured this offset was found to be -6.59 V at the output of the amplifier (or -11 mV at the input), in order to simply correct for this in the measurement, the input of the digital oscilloscope (which was used for all the measurements in this section) was set to AC-coupling. This meant that values which were recorded as 0 V in the AC-coupled measurement corresponded to an output voltage of -6.59 V

...maybe add glossary for this

from the amplifier. The *INA103 Data Sheet* (2000) explains that the amplifier is capable of a maximum voltage output range of ± 11 V. By dividing by the gain of the amplifier (600 in the configuration used) it was possible to calculate the range of input voltages, to the amplifier, for which a correctly amplified output was attainable (i.e. those which corresponded to an output of less than ± 11 V); this was found to be ± 18.3 mV. As explained earlier however the JFET source follower used resulted in an offset voltage of -11 mV at the input of amplifier. When this was subtracted from the input range of the amplifier the effective range of input voltages, $V_{input_{eff}}$, was found to be

$$V_{input_{eff}} = V_{input} - V_{offset}, \quad (7.16)$$

$$= \pm 18.3 \text{ mV} - -11.0 \text{ mV}, \quad (7.17)$$

$$= {}^{+29.3}_{-7.3} \text{ mV}. \quad (7.18)$$

While this result has the advantage of meaning the amplifier system had an increased range for positive signals, there was a severe restriction places on the amplifiers ability to handle negative signals. Fortunately the required measurable input voltage range for testing SiCEB devices was only of the order of ± 1 mV, with few circumstances existing where signals of greater magnitude were measured and none that would require measuring down to 7.3 mV across the device. For comparison the previous amplifier's input range, which did not suffer from any asymmetry, was ± 13 mV.

Since the restricted range of input voltage did not, in fact, affect the amplifier's suitability for the and measurements being undertaking, despite this clearly being non-ideal, it was decided that there was no need to address this. As previously mentioned, the DC offset due to the JFET could have been removed via the addition of a second JFET on each input.

In order to measure the 3-dB bandwidth of this amplifier that same procedure was used as for the initial amplifier (described fully in Section 7.3.1), a signal generator was used to create a white noise signal which was input into the amplifier. The output of the amplifier, along with the output of the signal generator, were monitored using a digital oscilloscope. To measure the bandwidth of the amplifier the ratio of the input of the amplifier to its output (its gain) was measured, the results of this are shown in Figure 7.15. As explained by Equation 7.5 the edge of the 3 dB bandwidth corresponds to the frequency at which the gain has

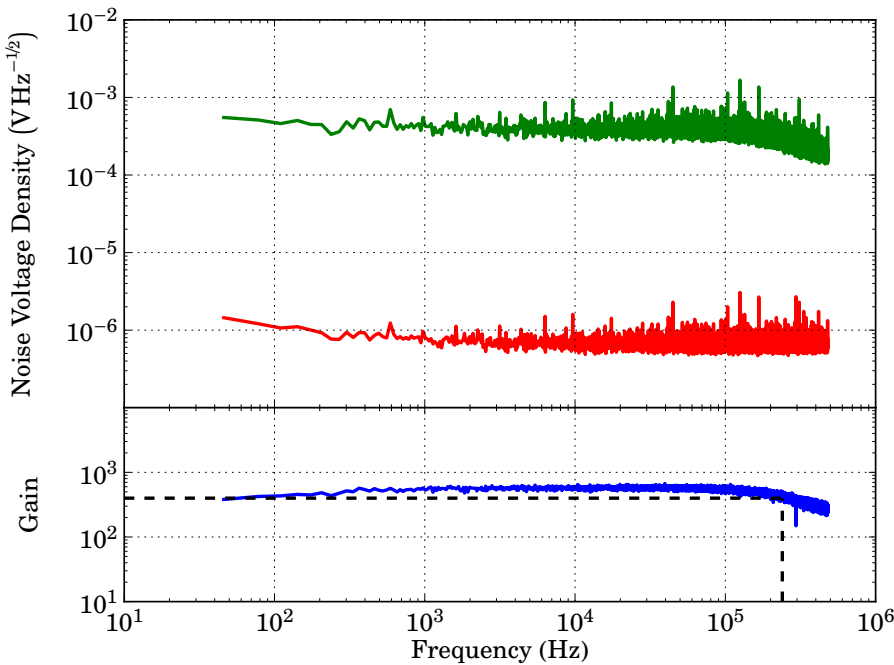


Figure 7.15: Bandwidth measurement of final amplifier. A white noise signal (red trace) was generated and supplied to the amplifier whose output (green trace) was also monitored. The ratio of these two (the gain, blue trace) was also calculated.

fallen by a factor of $\sqrt{2}$. The lower plot in Figure 7.15 shows the measured gain with the dashed lines illustrating the 3 dB level, which was a gain of 424, and the corresponding frequency found to be 240 kHz. This shows the amplifier offered a substantial improvement compared to its predecessor whose 3-dB bandwidth was equal to 55 kHz (calculated on page 87). Although the *INA103 Data Sheet* (2000) does not provide a figure for the expected bandwidth of the amplifier when operating with a gain of 600, it does provide values of 6 MHz and 800 kHz for gains of 1 and 100 respectively, this seems to indicate that the value of 240 kHz, at a gain of 600, is to be expected.

Figure 7.16 shows the measurement of the internal noise of the final amplifier. This was measured with the input to the amplifier (the gates of the two JFET source followers) shorted such that there was a differential signal of 0 V at the

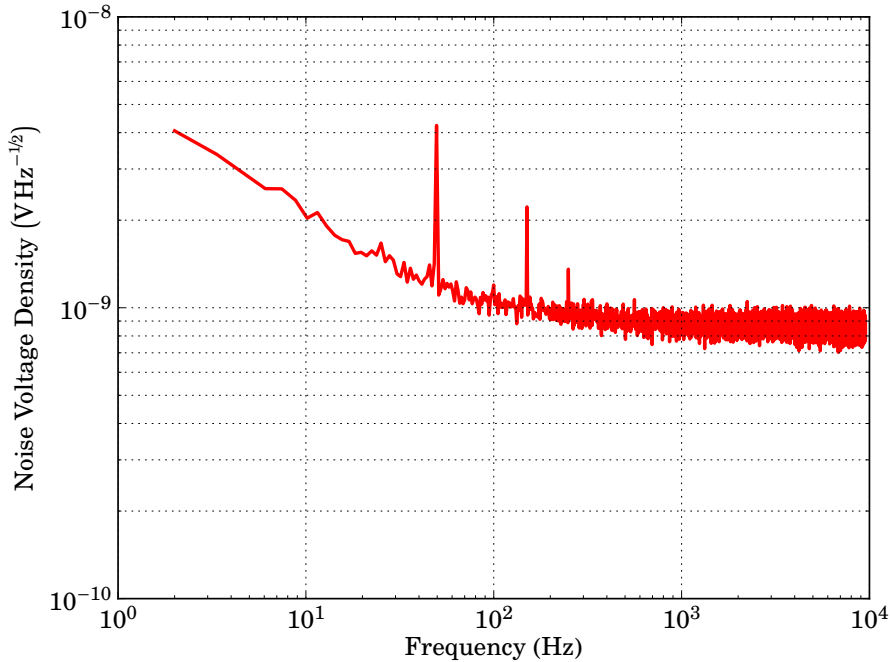


Figure 7.16: Measurement of the internal noise, referred to the input, for the final amplifier. Measured for a shorted input of the amplifier.

input of amplifier. The output of the amplifier was fed to a digital oscilloscope, which computed the Fourier Transform of the signal. This was then divided by the gain (measured in Figure 7.13) to give the input referred internal noise of the amplifier. From Figure 7.16 it can be seen that the white noise level of this noise spectrum is approximately $1.5 \text{ nV}\text{Hz}^{-1/2}$ and the spectrum is white from a few hundred hertz up until the end of the measurement at 10 kHz.

When compared to the corresponding measurement for the previous amplifier, shown in Figure 7.5, two key differences are immediately apparent. Firstly, the newer amplifier has a substantially lower noise level, with the white noise floor of the previous amplifier having been $10 \text{ nV}\text{Hz}^{-1/2}$ compared to the newer device's level of $850 \text{ pV}\text{Hz}^{-1/2}$; this notable improvement was the key reason for switching to the newer amplifier. Secondly, there is a more pronounced level of $1/f$ noise visible in the spectrum for the newer amplifier compared to its predecessor, while indeed

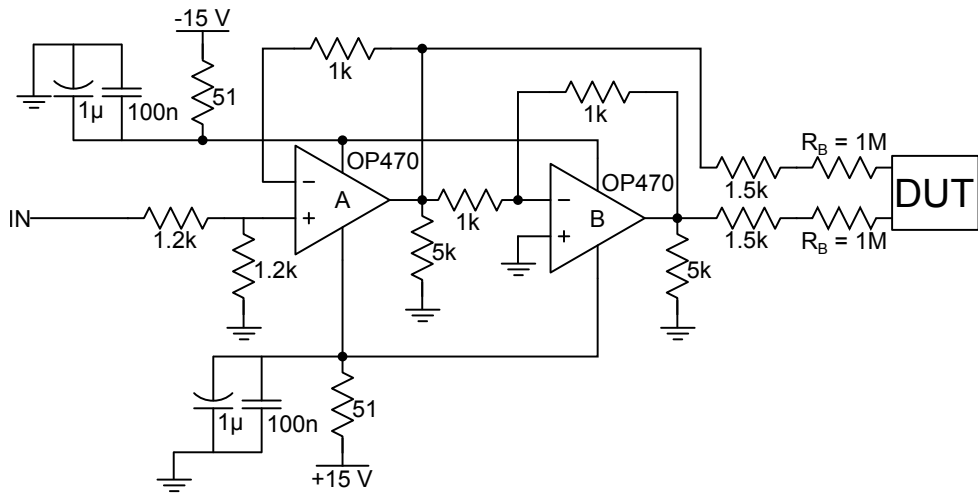


Figure 7.17: Circuitry used to generate a differential signal used to bias the device under test. The principle is the same as described in Section 7.4.

undesirable the *INA103 Data Sheet* (2000) indicates that this is to be expected for this device and it is worth noting even when allowing for this additional noise the newer amplifier still offered low noise at these frequencies than the previous amplifier.

These two tests showed that the replacement amplifier offered a notable improvement, in all areas, over the initial amplifier used and also showed that despite the newer device having some limitations not present in its predecessor (principally the asymmetric limit to the input voltage, shown in Figure 7.14), these limitations did not stop it from being fit for the testing required.

7.5.3 FINAL BIAS SYSTEM

For simplicity of integration a biasing system, similar to that described in Section 7.4, was integrated into this final system. The circuitry for this, shown in Figure 7.17. The only difference in operation between this circuit and the system used previously was the relation between the input signal and the differential output. For the previous system this was 1 : 2, meaning for an input of 1 V a differential signal of 2 V was output (as explained on Page page 93). The key difference here was that although both of the OP470 amplifiers (manufactured by Analog Devices and in fact housed within a single package) were configured to provide a

gain factor of unity, an additional potential divider was included at the input of the first amplifier. This divider (the two $1.2\text{ k}\Omega$ resistors seen in Figure 7.17) acted to reduce the input of the first amplifier by a factor of a half. This meant that the output of each of the amplifiers was equal to one half of the input voltage, thus the total differential voltage at the output was the same as the input voltage. As in the previous case the device was biased via a pair of $1\text{ M}\Omega$ biasing resistors and the biasing current can be calculated similarly to the method on page 93. For this system, using Equation 7.7 the biasing voltage V_{bias} was simply given by:

$$V_{bias} = V_{in}, \quad (7.19)$$

where V_{in} was the input voltage to the bias generator. This meant that the biasing current, I_{bias} , across the device under test was calculated as:

$$I_{bias} = \frac{V_R}{2R_{bias}}, \quad (7.9 \text{ revisited})$$

where V_R is again the voltage dropped across the biasing resistors and, given the result shown in Equation 7.19, was calculated by:

$$V_R = V_{in} - V_{DUT}, \quad (7.20)$$

where V_{DUT} is the voltage measured across the device under test. Finally combining this with Equation 7.9 gave the final relation for the biasing current:

$$R_{bias} = \frac{V_{in} - V_{DUT}}{2I_{bias}}. \quad (7.21)$$

As for the previous biasing systems it was important to measure the jitter in the current produced. This was preformed by configuring⁵ the bias generator to produce a current of $1\text{ }\mu\text{A}$ which was driven across a $10\text{ k}\Omega$. This meant that the expected voltage measured across the resistor, according to Ohm's Law, was 10 mV . Figure 7.18 shows the results of this measurement. The maximum variation from the expected value was 800 nV which corresponded to a peak-to-peak jitter of 160 ppm . While this was still not as low as the jitter measured for the Keithley 220 unit, which was 110 ppm , it was in fact an improvement of the value

⁵The input voltage to the bias generator for this measurement was provided by using the system's on board voltage (controlled through a potential divider) rather than an external source.

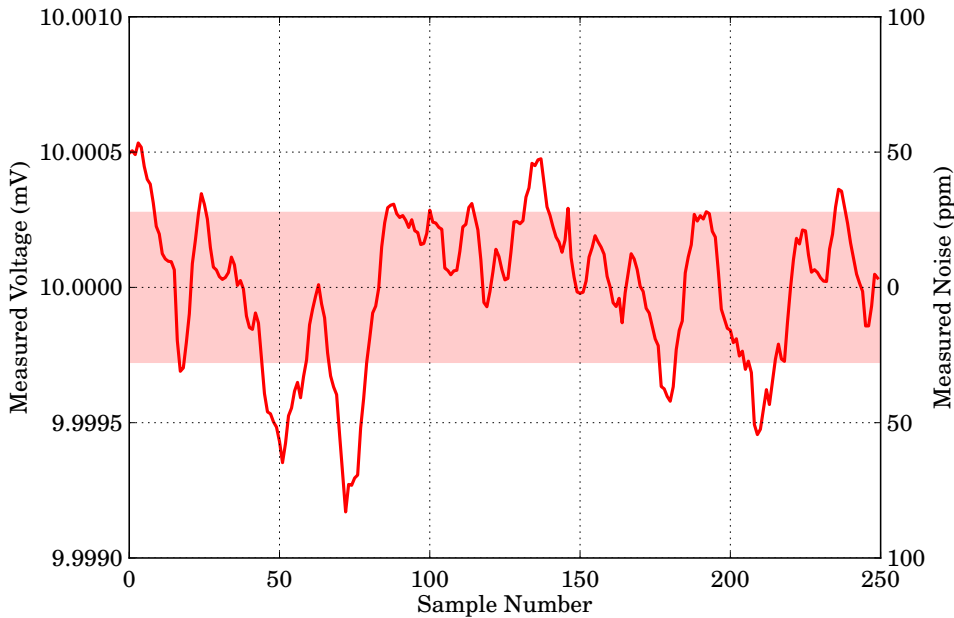


Figure 7.18: Measurement of jitter from the bias generator used with the final readout amplifier. The generator was configured to produce a biasing current of $1 \mu\text{A}$ which was driven across a $10 \text{ k}\Omega$ resistor.

of 200 ppm which was measured for the previous bias generator in Section 7.4.2. Since the jitter of the previous system had caused no problems, there was no reason to conclude that any issue would be presented here.

Figure 7.19 shows the noise spectrum, measured using the amplifier described in Section 7.5.2, for a device (a low resistance resistor) biased by the system shown in Figure 7.17. Comparison between this figure and the noise spectrum shown in Figure 7.16 shows that the dominating noise is from the internal processes in the amplifier and the bias generator did not contribute any additional noise to this measurement. This is that same as had been found for the previous bias generator system and is not a surprise considering the similarities, in operational principle, between the two systems.

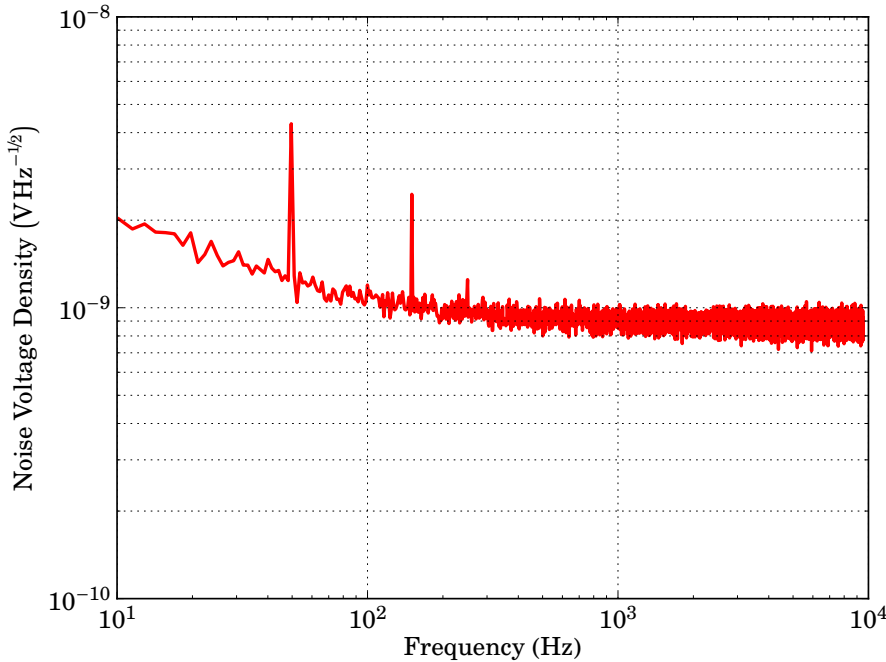


Figure 7.19: Noise measurement for bias generator used in conjuncture with final readout system. A low value resistor ($\approx 10 \Omega$) was placed across the output generator and the amplifier was used to amplify the signal. The output of the amplifier was read by a digital oscilloscope which computed the noise spectrum.

7.6 CROSS-CORRELATED NOISE MEASUREMENT

Despite the improved (lower) noise limit of the system detailed in Section 7.5 this system was, at best, only able to measure noise generated within a device at optimum bias⁶. To allow a full study of the sensitivity of a device it was important to be able to measure the noise in the device over the greatest possible range of biases. To this end an innovative solution was devised to reduce the noise level of the readout system. This was to split the voltage readout of the device between

Add glossary entry

two identical amplifiers and then to use a computer to cross-correlate the output

⁶The dependance of various noise sources to the bias, or more correctly the bias dependant responsivity, is explained in Section 3.7.

of these to effectively remove the noise contribution of the amplification.

7.6.1 CONVOLUTION

The convolution of two signal or functions is a third function whose amplitude is given by the area overlap of the f and g when one of the functions is reversed and then translated across the other function. Common applications of convolution include: measuring the response function to an impulse function (Callier and Desoer, 1978), in probability the convolution of two independent variables gives the probability distribution (Hogg, McKean, and Craig, 2012), in acoustics and sound-engineering reverberation is the convolution of an original signal with reflections (echos) from surfaces (Begault, 2007), in signal processing a weighted average of a signal is a convolution.

In time-space the convolution of two functions, f and g , is written as $f * g$. Mathematically this is computed by reversing one of these functions such that $f(t) \rightarrow f(t - \tau)$ and then translated across the other function. This can be written as an integral as,

$$(f * g)(t) \stackrel{\text{def}}{=} \int_{-\infty}^{\infty} f(\tau)g(t - \tau) d\tau. \quad (7.22)$$

Convolution is commutative so $f * g = g * f$ or more completely:

$$\begin{aligned} (f * g)(t) &\stackrel{\text{def}}{=} \int_{-\infty}^{\infty} f(\tau)g(t - \tau) d\tau, \\ &= \int_{-\infty}^{\infty} f(t - \tau)g(\tau) d\tau. \end{aligned} \quad (7.23)$$

It is, perhaps, easiest to understand convolution in the time-domain graphically. This is shown in Figure 7.20. From this figure it can be seen that the value of convolution at any time τ is given by the area overlap of the two function (shown as the highlighted regions in Figures 7.20d to 7.20h) when the leading non-zero value of the reversed function ($g(t)$ in this case) is at τ .

Convolution can be thought of much more simply in the frequency domain. As explained by Bracewell (2000, chap. 2), Convolution Theory states that the Fourier Transform of the convolution of two functions is the multiplication of the Fourier transforms of the functions. This can be written as:

$$\mathcal{F}\{f * g\} = \mathcal{F}\{f\} \cdot \mathcal{F}\{g\} \quad (7.24)$$

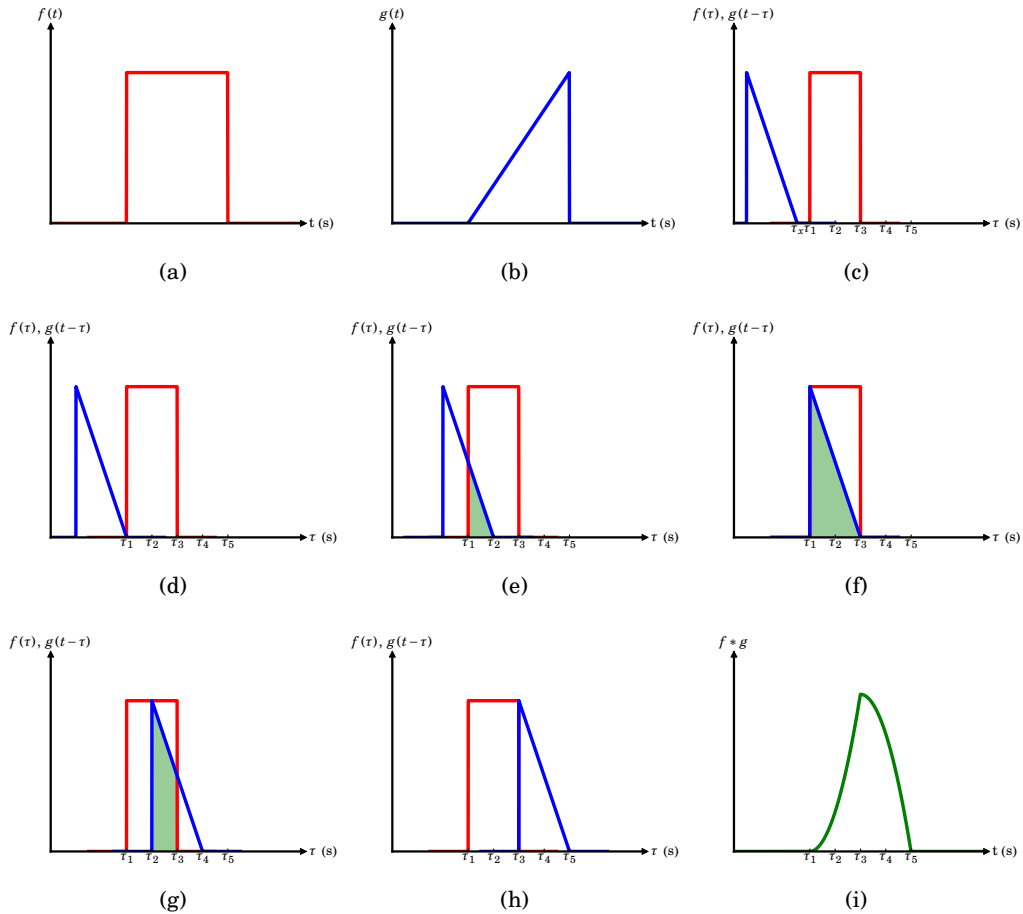


Figure 7.20: RERUN THESE AND CORRECT NON-ITALIC ‘t’ IN AXIS!!!!!! Graphical representation of convolution in the time domain. Two function $f(t)$ and $g(t)$, shown in parts (a) and (b) respectively. To find the convolution of the two functions one function is reversed in time (in this case $g(t)$ was chosen), this is shown in part (c), and then translated across the other function, shown in parts (d) through to (h). The value of the convolution at any time, τ , is the area overlap (shown as the highlighted areas in parts (d) through to (h)) of the two functions when the leading non-zero value of the translated function is at τ . The convolution function is shown in part (i).

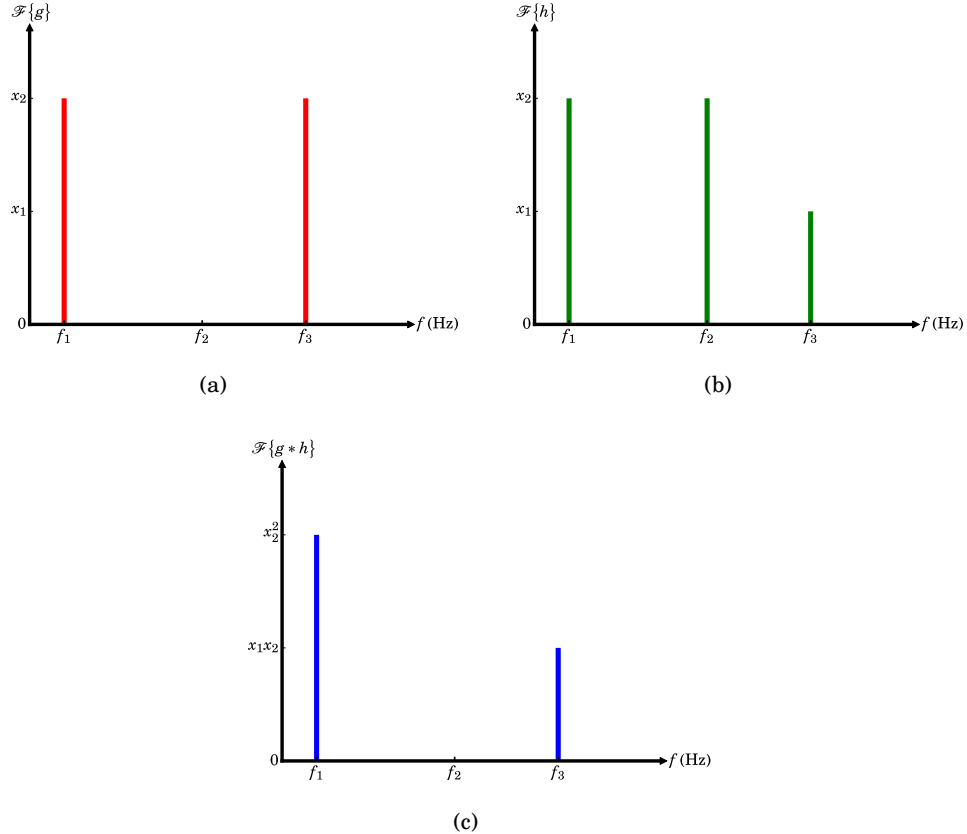


Figure 7.21: Convolution in the frequency domain. Two functions g and h , whose Fourier transforms ($\mathcal{F}\{g\}$ and $\mathcal{F}\{h\}$) are shown in (a) and (b) respectively. (c) shows the Fourier transform of the convolution of g and h ($\mathcal{F}\{g * h\}$), it can clearly be seen that this is the same as the point-by-point multiplication of the two Fourier transforms of g and h (as is expected from the convolution theory).

where \mathcal{F} is the Fourier Transform function, and f and g are functions⁷. The convolution of two functions in the frequency domain is illustrated in Figure 7.21.

Change back to
PDF

⁷The scalar product symbol (\cdot) is used in Equation 7.24 to avoid confusion with the vector product (\times) since the two Fourier transforms are multiplied on a point-by-point basis.

7.6.2 CROSS CORRELATION

Cross-correlation is a mathematical process which can be used to measure the similarity of two functions or signals and is closely related to convolution. Mathematically the cross-correlation of two functions, $f(t)$ and $g(t)$, is defined as:

$$(f \star g)(t) \stackrel{\text{def}}{=} \int_{-\infty}^{\infty} f^*(-\tau)g(t-\tau) d\tau, \quad (7.25)$$

where f^* is the complex conjugate of f . A quick comparison to the definition of the convolution (Equation 7.22):

$$(f * g)(t) \stackrel{\text{def}}{=} \int_{-\infty}^{\infty} f(\tau)g(t-\tau) d\tau, \quad (\text{Equation 7.22 revisited})$$

shows that the convolution and cross-correlation are simply related by:

$$f(t) \star g(t) = f^*(-t) * g(t). \quad (7.26)$$

7.6.3 APPLICATION OF CROSS CORRELATION TO DETECTOR READOUT

In order to completely characterise a detector it is important to measure the electronic noise generated within the detector itself; this is because it is this noise that will define the ultimate sensitivity of the detector—for a CEB-type detector the various internal noise sources have been covered in Section 3.6. The measurement of a detector’s noise is complicated however by the fact that the amplitude of internal noise in the detector is, in most cases, much less than the input-referred noise of the readout amplifier. While it is possible to simply state that in any realistic scenario the performance of the detector (in terms of sensitivity at least) will be limited by the amplifier and thus it is justifiable to calculate the sensitivity of the detector based upon the noise of the readout amplifier; in a study of the detector itself (rather than an instrument utilising the detector) it is important to characterise the detector as completely as possible. This was one of the main reason for the switch from the readout amplifier described in Section 7.3 to that described in Section 7.5.

Unfortunately the INA103 based amplifier (described in Section 7.5, which had an input-referred noise amplitude of $\sim 1 \text{ nV}\text{Hz}^{1/2}$) was unable to directly measure the internal noise of the CEB detectors being studied, to address this a novel readout and data-processing system was devised utilising two parallel JFET-buffered

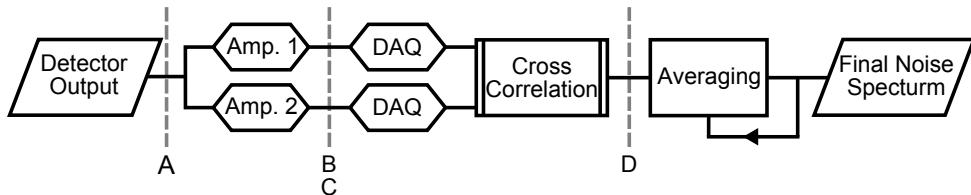


Figure 7.22: Simplified process flow for measurement of low levels of electrical noise by utilising cross correlation of two signal from a common source. Intersections with dashed lines correspond to the example noise power spectra shown in Figure 7.23.

INA103 amplifiers (as shown in Figure 7.12) and cross correlating their outputs. The concept behind the design of this readout system was that while the average noise amplitude of the two amplifiers would be the same their noise spectrum are not correlated hence the cross correlation techniques described above should be capable of removing the noise signal generated by the amplifier⁸, on the other hand and signal supplied to both amplifiers will be present and correlated in the output of both amplifiers and thus would be present after the two signals were cross correlated. The voltage output of the detector was split between the two amplifiers with the output each amplifier fed into a separate channel of a data acquisition system. Once the signals had been digitised by the data acquisition system the two signals were cross correlated by National Instruments LabView software. A simplified process flow for the measurement detector noise using this technique is shown in Figure 7.22.

The effect of using cross correlation to remove electrical noise introduced by readout amplifiers is illustrated in Figure 7.23 which shows simplified examples of the noise power spectrum at various stages of the process flow shown in Figure 7.22—the spectra shown in Figure 7.23 correspond to the points at which the process flow intercepts the dashed lines in Figure 7.22. Figure 7.22 shows that while the majority of the noise contributed by the amplifiers is successfully removed some features remain, this is due to the random probability of both amplifiers generating a tone at a given frequency. When both noise spectra contain features at corresponding frequencies there will also be a tone at the same frequency

[Change back to PDF](#)

⁸Since the exact amplitude and frequency spectrum of the amplifier noise is random, it is clear that multiple cross correlated acquisitions may need to be combined to remove the amplifier noise.

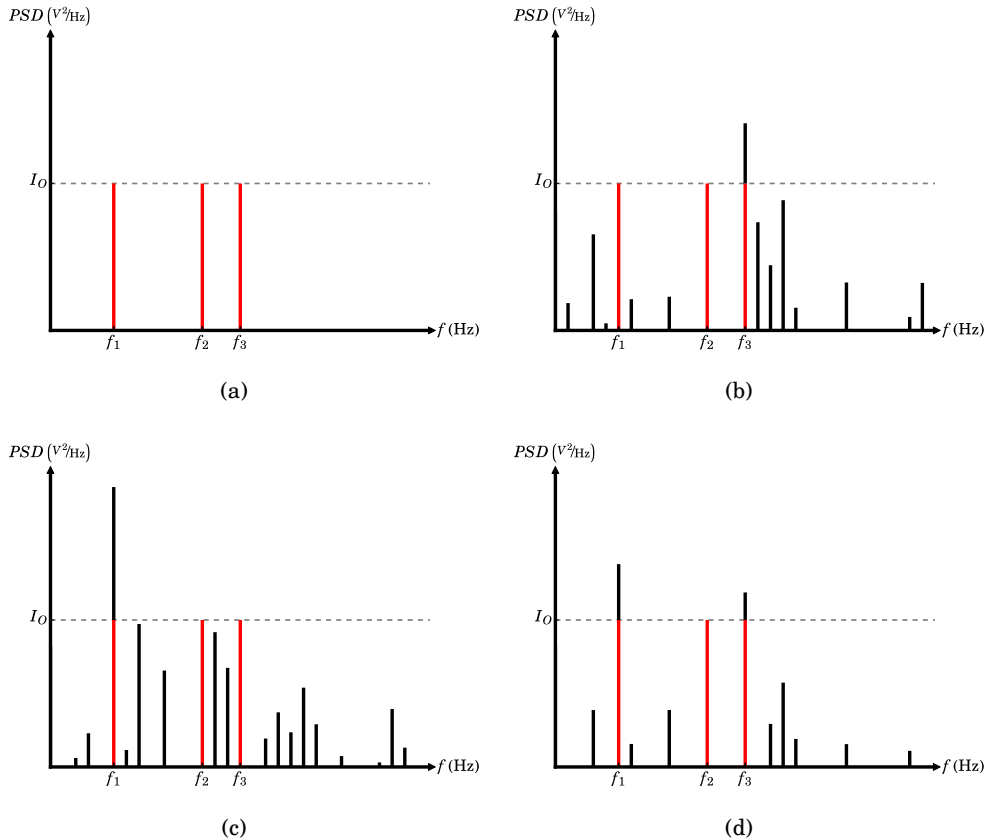


Figure 7.23: Removal of amplifier noise from a measurement by the use of cross correlation. (a) Power spectrum of detector output; the signal consists of three tones, each of intensity I_O , at frequencies f_1 , f_2 and f_3 . (b) and (c) Outputs of the two parallel amplifiers; the signal (shown in red) is still present however the power spectra now also includes several other features including noise which has affected the signal at f_3 in (b) and f_1 in (c). (d) Output from readout system without any averaging; the majority of the noise introduced by the amplifiers has been removed (some features remain due to the random nature of the noise generated by the amplifiers meaning that it is possible for features to exist at the same frequency in the outputs of both amplifiers, such features will *survive* the cross correlation) the alteration to the signal at f_1 and f_3 has also been reduced. Subfigure numbering corresponds to the points at which the signal intersects with the dashed lines in Figure 7.22. (Colours for reference only.)

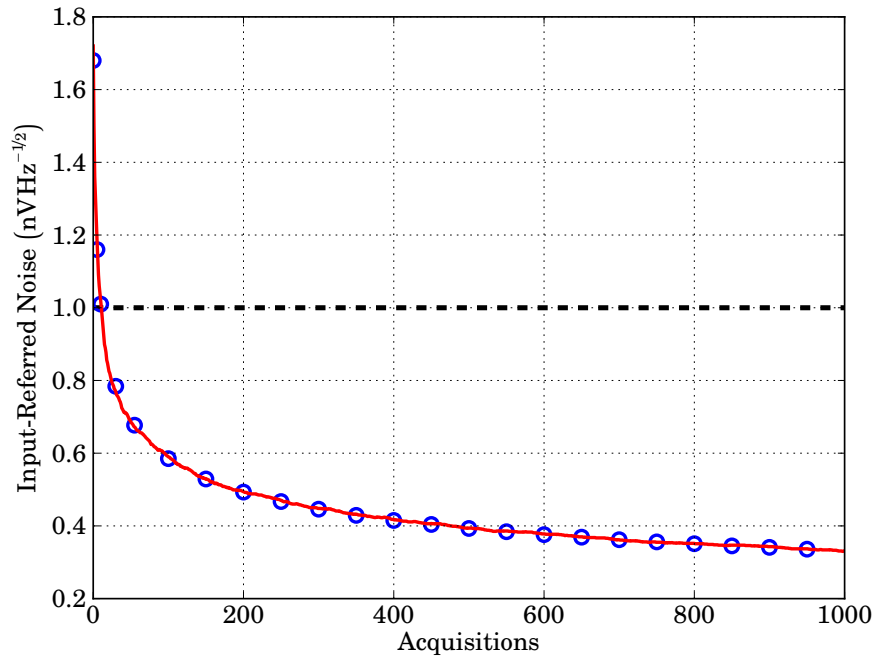


Figure 7.24: Reduction in input-referred noise with increased number of averaged acquisitions for cross-correlated amplifiers. Solid line—simulation performed in National Instruments LabView software. Open circles—Experimental data. Dashed line—Expected input-referred noise for a single INA103 amplifier. It is clear that the simulation and experimental data are in excellent agreement.

in the cross correlated spectrum. While this cannot be avoided, the amplitude of these tones can be substantially reduced with averaging.

The performance of this readout system has been both simulated (using artificial signals generated by National Instruments LabView software) and measured experimentally. Both the simulation and the measurement were of the amplifiers having a shared connection to a short (equivalent to the scenario for measuring the input-referred noise of an amplifier used throughout the work covered in this chapter). Figure 7.24 shows the results the simulation (solid line), along with experimental data (open circles)⁹ and the expected noise level resulting from one

⁹For clarity the experimental data have been reduced prior to plotting.

of the amplifiers operating singularly. It can be seen from Figure 7.24 that the simulation and measured data are in excellent agreement. Both the simulation and the measured data start above the specified amplifier noise, this is due to the mechanics of the noise measurement and the possibility of a single cross-correlated acquisition causing an increase in the noise. After a small number of acquisitions (approximately ten) the measured noise level has dropped to that of the input-referred noise of a single amplifier. With continued acquisitions the noise level continues to drop until a constant level, well below the amplifiers' input-referred noise, is reached. This *noise floor* is caused by the binning of the waveform in the sampling process and the random probability of a noise feature at each of the binned frequencies in the Fourier transform of the sampled data. The minimum achieved input-referred noise of the cross-correlated amplifier setup was found to be approximately $330 \text{ pVHz}^{-1/2}$.

7.7 SUMMARY OF READOUT AND BIASING SYSTEMS

As has been covered in this chapter a number of systems have been developed and used to measure SiCEB detectors. While the majority of the measurements presented in this work were performed with the equipment described in Section 7.5 (with successful measurements of the device and photon noise performed using the techniques described in Section 7.6), some early measurements were performed with the systems described earlier in this chapter (where this is the case it has been made apparent). A summary of the performance of the various bias systems and readout amplifiers described throughout this chapter is given in Tables 7.1 and 7.2 respectively.

Table 7.1: Summary of detector bias systems.

System	Bias Jitter (μA)	Notes
Keithley 220	0.55	See below ^a
Initial custom bias generator ^b	1.00	
Final custom bias generator ^c	0.80	

^a This unit caused substantial levels of electrical noise to be introduced into the measurement (as seen in Figure 7.7).

^b Based upon Analog Devices' AMP03 amplifier.

^c Based upon Analog Devices' OP470 amplifier.

Check this, simulation should, should possibly start at Vamp, check what averaging does to a single amplifier

Table 7.2: Summary of detector readout systems.

System	Gain	Input Range (mV)	3-dB BW (kHz)	IRN ($\text{nV}\text{Hz}^{-1/2}$)
Initial System	1000	± 12.7	55	10.00
Final System	600	$+29.3$ $- 7.3$	240	0.85
Final System w/ Cross-Correlation	600	$+29.3$ $- 7.3$	240	0.33

Check figures for correct hyphenation of input-referred noise. Check text for correct hyphenation of cross-correlated amplifiers and IRN (only when compound adjective)

For any acronyms which have glossary entries, make the glossary the main key used and include first = { gls acr:*

Chapter Eight

Results: Dark Measurements

8.1 INTRODUCTION

The first stage of device testing was to characterise the device in the absence of any optical signal. These tests were performed in one of the first two cryogenic systems described in Chapter 6. The purpose of these tests was firstly to ascertain that the detectors had been fabricated correctly, that is to say that a Schottky contact had formed between the aluminium and the doped silicon. The second goal of these measurements was to produce a set of data to which later—optical—data could be compared. The characterisation performed in these measurements concentrated on the current-voltage relationship of the detectors at various different bath temperatures. Attempts were also made to measure the device noise at this point however it was found that the amplifier noise of the readout circuitry used at the time dominated these measurements.¹

8.2 UNSTRAINED SILICON

It is logical to start the exploration of Silicon Cold Electron Bolometers with the devices fabricated from the unstrained (but still highly-doped silicon material); the structure of these devices has already been illustrated in Figure 5.6a. This device could be thought of as offering a benchmark to which the performance of a detector utilising strained silicon could be compared. Inspection of Equation 3.113 shows immediately that key limiting parameter to the noise equivalent power is

¹This was the reason the system described in Section 7.6 was devised.

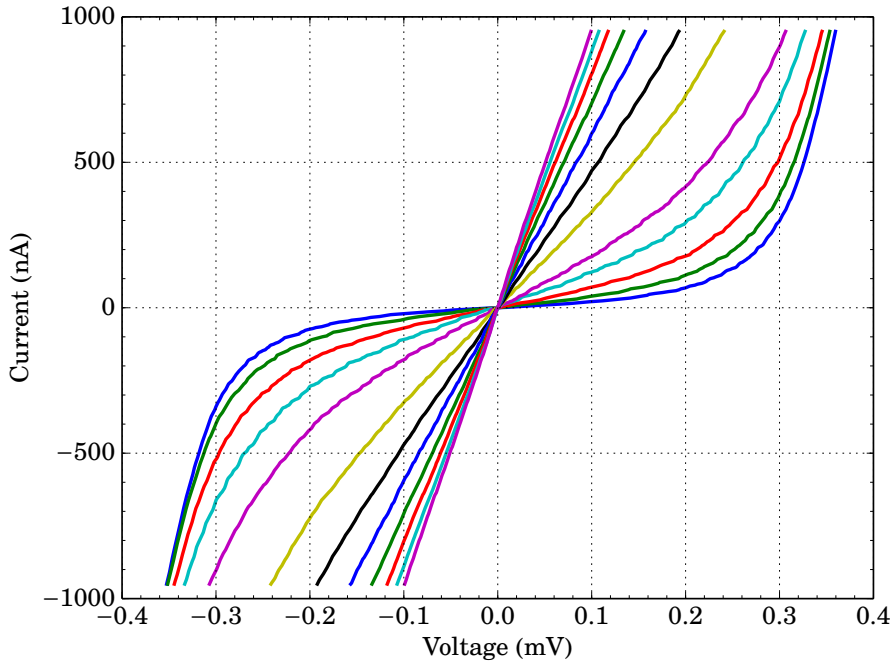


Figure 8.1: Current-voltage characteristics for a SiCEB with an unstrained absorber at various bath temperatures. Bath temperature from outermost (blue) to innermost (magenta, second occurrence): 0.30, 0.35, 0.40, 0.45, 0.50, 0.60, 0.70, 0.80, 0.90, 1.00, 1.10, and 1.20 K.

the electron-phonon coupling, Σ ; Table 5.3 shows that this parameter is substantially larger for a unstrained detector compared to a detector using strained silicon (by a factor of 26 in fact). From this it is immediately clear that one should expect the detector described in this section to be less sensitive than the detector utilising strained silicon, described later in this chapter. Furthermore, Equations 3.53 and 3.63 show that the responsivity, in either bias regime, is decreased for increased electron-phonon coupling, further increasing the noise equivalent power (reducing the detectors sensitivity).

The current-voltage (I-V) characteristics of the unstrained SiCEB have been tested in the *Aloysius* system detailed in Section 6.4.1 and were performed with the bias and readout system described in Section 7.5. The current-voltage characteristics at various bath temperatures are shown in Figure 8.1.

Examination of Figure 8.1 shows that for low bath temperatures the I - V curve is highly non-linear. The low voltage area corresponds to where the Fermi level in the silicon corresponds to the energy gap within the superconductor and thus electrons cannot tunnel out of the silicon absorber into the superconducting contacts (this corresponds to the scenario shown in Figure 3.3). As the voltage across the device increases the energy levels in the semiconductor and superconducting contacts are rearranged such that the Fermi level within the semiconductor corresponds to the vacant states above the superconducting energy gap, allowing carriers to exit the semiconductor via the tunnelling contacts (the arrangement shown in Figure 3.4). This change is seen in the I - V curve by the increased gradient (lower resistance) at higher biases. At the highest biases, where the Fermi level in the semiconductor is well above the superconductor's energy gap, the I - V curve is linear with a resistance determined by the sum of the two tunnelling resistance and the resistance of the silicon absorber itself. It should be mentioned that the data quality in this Figure 8.1 is lower than might have been desired, this has been attributed to contamination of the signals within the *Aloysius* testbed. Specifically it is believed that this was caused by microphonic noise introduced by the pulse tube cooler combined with pickup from the refrigerator control and monitoring circuitry. As will be seen later in this chapter these issues were addressed for later, more critical, measurements.

As the bath temperature was increased (the outermost curve in Figure 8.1 corresponds to the lowest bath temperature) it is clear that the non-linearity of the I - V curve diminished. This is due to the reduction of the superconducting energy gap (as shown in Figure 3.6) with increasing temperature. As the gap decreases the energy needed to align the absorber with the vacant states above the superconducting gap decreases accordingly until the situation where $T_{bath} = T_c$ at which point the gap is diminished to zero and no additional energy is required for tunnelling from the absorber to the contacts. The case where $T_{bath} = T_c$ is shown by the innermost curve of Figure 8.1, which is entirely linear with a resistance corresponding to the tunnelling resistance (along with any contribution from the absorber and the now normal-state contacts) at all biases. For the aluminium contacts used in this detector T_c was equal to 1.2 K.

An alternative way of viewing the data shown in Figure 8.1 is to calculate the differential resistance (dV/dI) of the detector as a function of either the voltage across the detector or the current flowing through the detector. This is shown in

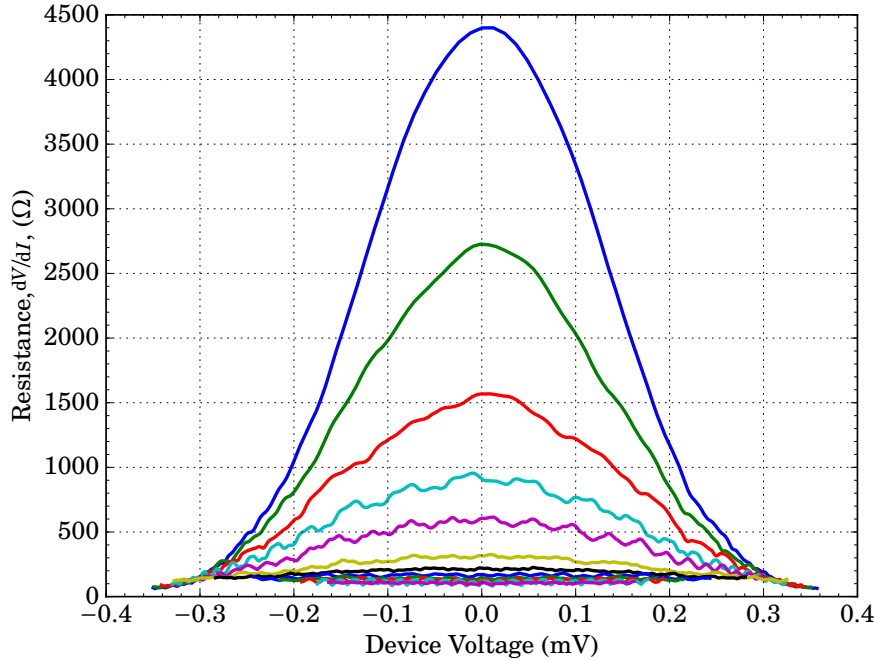


Figure 8.2: Differential resistance for a SiCEB with an unstrained absorber at various bath temperatures. Colours as in Figure 8.1 Bath temperature from outermost (blue) to innermost (magenta, second occurrence): 0.30, 0.35, 0.40, 0.45, 0.50, 0.60, 0.70, 0.80, 0.90, 1.00, 1.10, and 1.20 K.

Figure 8.2.² It is clear from this figure that as the voltage across increases the resistance tends to the same value which is independent of the bath temperature. Closer inspection of the various data found this value to be of the order 80 Ω . This is slightly lower than the anticipated value of 98 Ω which was derived from combining the anticipated contact resistance of 24 Ω per contact with the absorber resistance of 50 Ω . This slight discrepancy was most likely due to a Schottky contact not being formed evenly throughout the contact but instead some areas forming Ohmic contacts.

²Device voltage was selected as the x-axis of Figure 8.2 simply because this selection produced a clearer figure.

Using the data presented in Figure 8.1 it was possible to compute the electron temperature, T_e as a function of either the voltage across or current through the detector.³ This has been performed by fitting the data using Equation 3.28 with T_e as the only free parameter. In order to do this the data first needed to be prepared by noting a few facts about Equation 3.28 (previously discussed in Chapter 3). Firstly, Equation 3.28 only computes the current due to electron tunnelling through the barrier, it does not allow for the current drawn due to the series resistance of the detectors absorber, R_A ; to address this it was necessary to scale the voltage such that the current due to this resistance was removed, this voltage, V_J was simply given by:

$$V_J = V_{CEB} - IR_A, \quad (8.1)$$

where V_J is the voltage dropped through the two junctions, V_{CEB} is the total voltage across the detector, I is the current flowing through the detector, and R_A is the resistance of the absorber. Secondly, R_N in Equation 3.28 is the normal-state resistance of the structure (excluding the absorber resistance, as discussed above), that is to say the resistance of tunnelling through both junctions of the detector as seen at higher biases in Figure 8.1, Equation 3.28 however computes the current due to a single junction and as such it was necessary to simply divide the normal state resistance by a factor of two.⁴

This electron-temperature fitting has been performed for the data presented in Figure 8.1 and is shown in Figure 8.3 for the three lowest bath temperatures available 0.30, 0.35, and 0.40 K. It is clear from this figure that the electron temperature is equal to the bath temperature at zero bias and falls to minimum at a voltage corresponding to $2\Delta/e$ (≈ 0.3 mV). At voltages beyond $\approx 2\Delta/e$ the temperature of the electrons start to climb rapidly; this climb corresponds to the situation where a great number of carriers in the absorber have energies corresponding to the vacant states above the superconductor's energy gap and tunnelling becomes decreasing less thermally selective.

³As previously mentioned for Figure 8.2 figures have mostly commonly been plotted as a function of the device voltage for clarity along with providing a clearer link to the underlying physical processes.

⁴Note that Equation 3.28 already divides the voltage by a factor of two to allow for the series arrangement of two identical junctions.

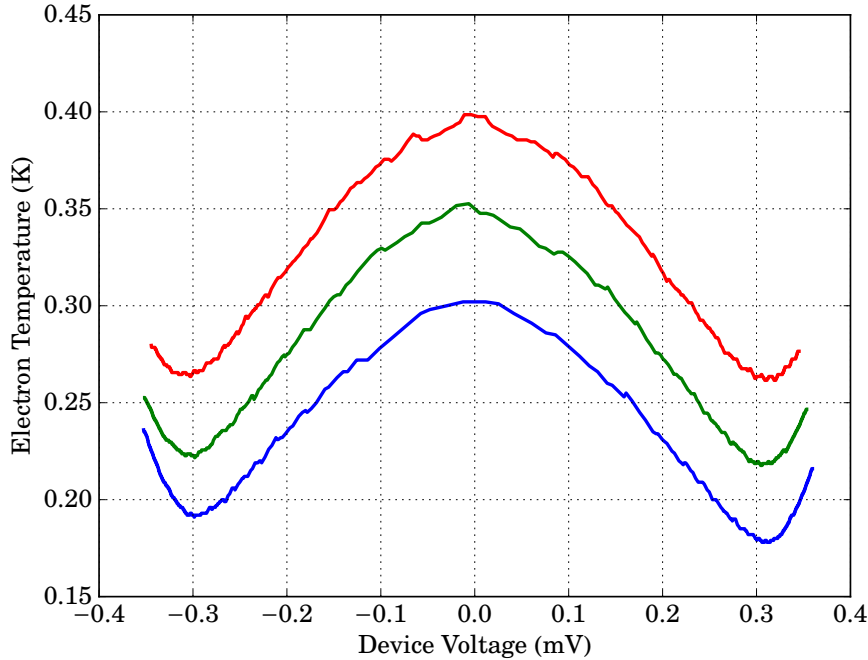


Figure 8.3: Electron-temperature fitting for SiCEB with an unstrained absorber at low bath temperatures. Bath temperatures from bottom to top: 0.30, 0.35, and 0.40 K. Note that $T_e = T_{bath}$ at $V = 0$.

8.3 STRAINED SILICON

The same measurements detailed in the previous section have been performed for a detector utilising a strained-silicon absorber. The expectation for this device was that it should show an ability to access lower electron temperatures due to reduced power flow between the phonons and the electrons in this material.

The current-voltage characteristics for the strained-silicon devices is shown in Figure 8.4. An immediate comparison which can be made is that the I - V curves measured at the lowest temperatures are much more tightly grouped than was seen in Figure 8.1 for the unstrained device. To illustrate this point the inset plot in Figure 8.4 shows the current-voltage relationship around the area $V = 2\mathcal{A}_e$, allowing the two coldest measurements ($T_{bath} = 0.30$ and 0.35 K, the outermost blue and green curves) to be seen distinctly. Closer comparison of the unstrained

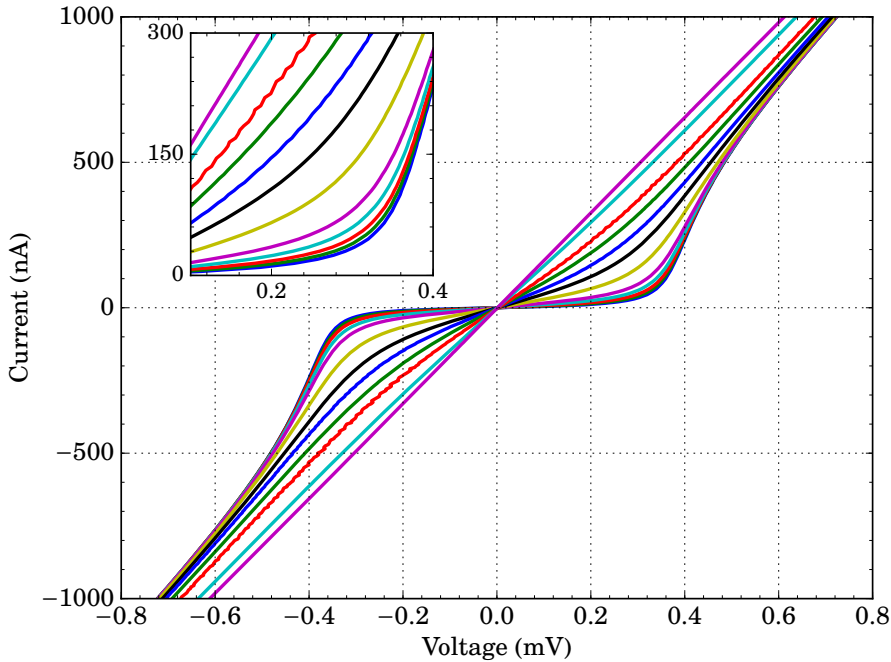


Figure 8.4: Current-voltage characteristics for a SiCEB with a strained absorber at various bath temperatures. Inset—zoomed-in plot around voltages corresponding to $24e$ to show the difference in the I - V curves at the lowest bath temperatures, the axes are the same as in the main figure. Bath temperature from outermost (blue) to innermost (magenta, second occurrence): 0.30, 0.35, 0.40, 0.45, 0.50, 0.60, 0.70, 0.80, 0.90, 1.00, 1.10, and 1.20 K, inset colours as in main figure.

and strained measurements also shows that the I - V curves in Figure 8.4 are flatter in the sub-gap region ($V = -0.3\text{--}0.3$ mV), this indicates that a higher-quality Schottky junction has been formed and as a result the so-called sub-gap leakage is reduced.

Some of the key differences between these data and the previously covered data for the unstrained silicon can be seen by examining the resistance of the detector as a function of the voltage across the device (as was done in Figure 8.2 for the unstrained-silicon device), this is shown in Figure 8.5. The normal-state

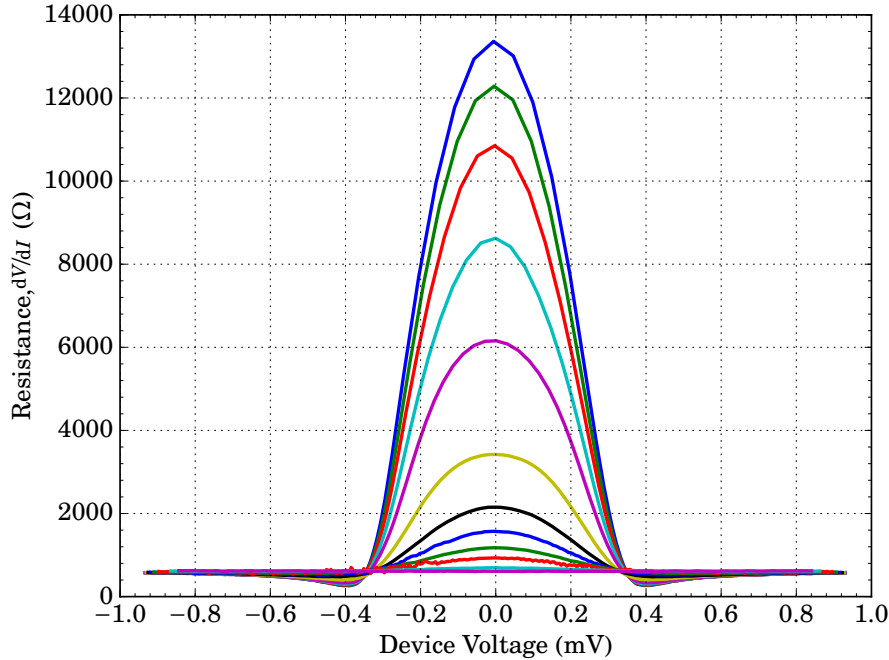


Figure 8.5: Differential resistance of a SiCEB with a strained absorber at various bath temperatures. Bath temperature from top (blue) to bottom (magenta, second occurrence): 0.30, 0.35, 0.40, 0.45, 0.50, 0.60, 0.70, 0.80, 0.90, 1.00, 1.10, and 1.20 K.

resistance of the strained-silicon device was noticeably higher than that of the unstrained detector, 580Ω compared to 80Ω measured for the unstrained detector. This increase was to be expected since the aluminium-silicon-junction resistance was shown in Table 5.3 to be a factor of almost 40 higher for this material than for the unstrained material. The discrepancy between this value and the measured ratio of the two normal-state resistances (a mere factor of 8) is further indication that high-quality Schottky contacts may not have formed evenly across the entire contact area during fabrication. A further increase in the normal-state resistance was to be expected due to the slightly higher sheet resistance of the strained material, this resulted in the absorber resistance being 75Ω (compared to 50Ω for the unstrained detector). This difference however is clearly negligible compared to the change in the contact resistance.

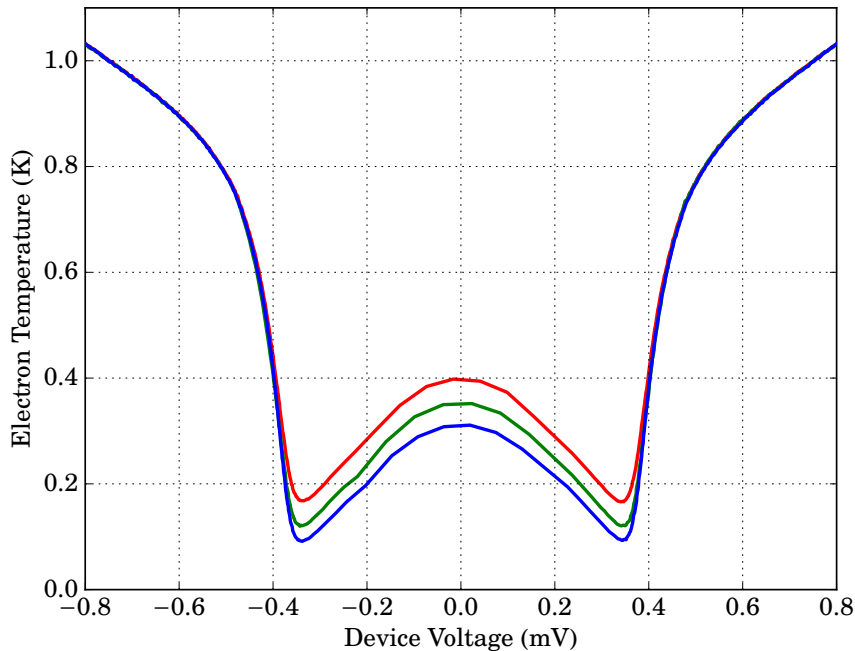


Figure 8.6: Electron temperature for a Strained-Silicon Cold Electron Bolometer at low bath temperatures. Bath temperatures from bottom to top: 0.30, 0.35, and 0.40 K. Note that $T_e = T_{bath}$ at $V = 0$.

As was performed for the unstrained-silicon device the electron temperature has been calculated (after the previously discussed relevant changes were made) for this device. The results of this are shown for the three lowest bath temperatures (0.30, 0.35, and 0.40 K) in Figure 8.6. This figure shows that at optimum bias the device was able to self-cool to electron temperatures of ≈ 100 mK from an initial bath temperature of 300 mK. The overall behaviour of this device seems much as expected with the electron temperature at zero bias being set by the temperature of the phonons (the bath temperature), the minimum value of electron temperature again occurs at the situation where the absorber's Fermi level is aligned with the top of the superconducting energy gap.

8.4 COMPARISON OF UNSTRAINED & STRAINED DETECTORS

A simple comparison between the two devices tested here can be made by comparing the measured characteristics on a like-for-like basis. Comparing the current-voltage curves of the two detectors (Figures 8.1 and 8.4) it can be seen that the curves for the strained-silicon detector have a much greater resistance below the superconducting gap (this point is made much more clearly from Figures 8.2 and 8.5 which show the resistance of the device), it can also be seen tunnelling occurs at slightly lower voltages in the unstrained device compared to the strained detector, this is not a property of the absorber but possibly a sign of a small issue with the aluminium contacts to the detector, this may also explain the lower subgap resistance in this device. The higher currents achieved for the strained sample are a result of the higher device resistance.

Comparing the electron-cooling performance of the two detectors (Figures 8.3 and 8.6) show that the device utilising strained silicon offered a notable reduction in the minimum achieved electron temperature. This device was able to cool carriers to a minimum temperature of 100 mK from a bath temperature of 300 mK compared to a minimum temperature of 170 mK for the untrained device operating in the same conditions.

The results collected in this chapter indicate that the optical testing of both devices is merited in order to compare the two materials in terms of their performance as detectors.

Maybe plots curves of V vs T at various biases

Bibliography

“The problem with quotations on the internet is that you can never be sure they’re authentic.”
— Abraham Lincoln

- Ade, P. A. R., G. Pisano, C. Tucker, and S. Weaver (2006). “A review of metal mesh filters”. In: vol. 6275, 62750U. DOI: 10.1117/12.673162 (Cited on page 75).
- Agilent 33220A Function/Arbitrary Waveform Generator Data Sheet* (2011). Agilent Technologies. URL: <http://cp.literature.agilent.com/litweb/pdf/5988-8544EN.pdf> (Cited on page 86).
- Arams, F., C. Allen, B. Peyton, and E. Sard (1966). “Millimeter mixing and detection in bulk InSb”. In: *Proceedings of the IEEE*. Vol. 54. 4, pp. 612–622. DOI: 10.1109/PROC.1966.4781 (Cited on page 6).
- Bardeen, J., L. N. Cooper, and J. R. Schrieffer (1957). “Theory of Superconductivity”. In: *Phys. Rev.* 108 (5), pp. 1175–1204. DOI: 10.1103/PhysRev.108.1175 (Cited on pages 22, 23).
- Begault, D. R. (2007). *3-D Sound: For Virtual Reality and Multimedia*. Academic Press (Cited on page 109).
- Bhatia, R. S., J. J. Bock, P. A. R. Ade, A. Benoît, T. W. Bradshaw, B. P. Crill, M. J. Griffin, I. D. Hepburn, V. V. Hristov, A. E. Lange, P. V. Mason, A. G. Murray, A. H. Orlowska, and A. D. Turner (1999). “The susceptibility of incoherent detector systems to cryocooler microphonics.” In: *Cryogenics* 39.8, pp. 701–715. DOI: 0.1016/S0011-2275(99)00071-5 (Cited on page 73).

- Bhatia, R. S., S. T. Chase, S. F. Edgington, J. Glenn, W. C. Jones, A. E. Lange, B. Maffei, A. K. Mainzer, P. D. Mauskopf, B. J. Philhour, and B. K. Rownd (2000). “A three-stage helium sorption refrigerator for cooling of infrared detectors to 280 mK”. In: *Cryogenics* 40.11, pp. 685–691. DOI: 10.1016/S0011-2275(00)00072-2 (Cited on page 68).
- Bintley, D., A. L. Woodcraft, and F. C. Gannaway (2007). “Millikelvin thermal conductance measurements of compact rigid thermal isolation joints using sapphire-sapphire contacts, and of copper and beryllium-copper demountable thermal contacts”. In: *Cryogenics* 47.5–6, pp. 333–342. DOI: 10.1016/j.cryogenics.2007.04.004 (Cited on page 75).
- Bracewell, R. N. (2000). *The Fourier Transform and its Applications*. 3rd ed. McGraw-Hill Higher Education (Cited on page 109).
- Brien, T. L. R., P. A. R. Ade, P. S. Barry, C. Dunscombe, D. R. Leadley, D. V. Morozov, M. Myronov, E. H. C. Parker, M. J. Prest, M. Prunnilla, R. V. Sudiwala, T. E. Whall, and P. D. Mauskopf (2014). “A strained silicon cold electron bolometer using Schottky contacts”. In: *Applied Physics Letters* 105.4, p. 043509. DOI: <http://dx.doi.org/10.1063/1.4892069> (Cited on page 8).
- Cabrera, N. and N. F. Mott (1949). “Theory of the oxidation of metals”. In: *Reports on progress in physics* 12.1, p. 163 (Cited on page 14).
- Callier, F. M. and C. A. Desoer (1978). “An algebra of transfer functions for distributed linear time-invariant systems”. In: *Circuits and Systems, IEEE Transactions on* 25.9, pp. 651–662. ISSN: 0098-4094. DOI: 10.1109/TCS.1978.1084544 (Cited on page 109).
- Caughey, D. M. and R. E. Thomas (1967). “Carrier mobilities in silicon empirically related to doping and field”. In: *Proceedings of the IEEE*. Vol. 55. 12, pp. 2192–2193. DOI: 10.1109/PROC.1967.6123 (Cited on pages 51, 52).
- Chi, C. C. and J. Clarke (1979). “Enhancement of the energy gap in superconducting aluminum by tunneling extraction of quasiparticles”. In: *Phys. Rev. B* 20 (11), pp. 4465–4473. DOI: 10.1103/PhysRevB.20.4465 (Cited on page 6).
- Clark, A. M., N. A. Miller, A. Williams, S. T. Ruggiero, G. C. Hilton, L. R. Vale, J. A. Beall, K. D. Irwin, and J. N. Ullom (2005). “Cooling of bulk material by electron-tunneling refrigerators”. In: *Applied Physics Letters* 86.17, p. 173508. DOI: 10.1063/1.1914966 (Cited on page 6).
- Cooley, J. W. and J. W. Tukey (1965). “An algorithm for the machine calculation of complex Fourier series”. In: *Math. comput.* 19.90, pp. 297–301. DOI: 10.1090/S0025-5718-1965-0178586-1 (Cited on page 140).
- Dall’Oglio, G., L. Pizzo, L. Piccirillo, and L. Martinis (1991). “New $^3\text{He}/^4\text{He}$ refrigerator”. In: *Cryogenics* 31.1, pp. 61–63. DOI: 10.1016/0011-2275(91)90193-Z (Cited on page 68).

- ESA (2014). *SPICA - A SPACE INFRARED TELESCOPE FOR COSMOLOGY AND ASTROPHYSICS*. Press Release. URL: <http://sci.esa.int/cosmic-vision/53635-spica/> (Cited on page 10).
- Golubev, D. and L. S. Kuzmin (2001). "Nonequilibrium theory of a hot-electron bolometer with normal metal-insulator-superconductor tunnel junction". In: *Journal of Applied Physics* 89.11, pp. 6464–6472. DOI: 10.1063/1.1351002 (Cited on pages 32, 34, 36, 38, 81).
- Golwala, SR, J Jochum, and B Sadoulet (1997). "Noise considerations in low resistance NIS tunnel junctions". In: *Proceedings of the Seventh International Workshop on Low Temperature Detectors*, pp. 56–59 (Cited on page 38).
- Hagmann, C., D. J. Benford, and P. L. Richards (1994). "Paramagnetic salt pill design for magnetic refrigerators used in space applications". In: *Cryogenics* 34.3, pp. 213–219. DOI: 10.1016/0011-2275(94)90171-6 (Cited on page 71).
- Hagmann, C. and P. L. Richards (1994). "Two-stage magnetic refrigerator for astronomical applications with reservoir temperatures above 4 K". In: *Cryogenics* 34.3, pp. 221–226. DOI: 10.1016/0011-2275(94)90172-4 (Cited on page 71).
- Hartog, R. den, J. Beyer, D. Boersma, M. Bruijn, L. Gottardi, H. Hoevers, Rui Hou, M. Kiviranta, P. de Korte, J. van der Kuur, B. van Leeuwen, M. Lindeman, and A. Nieuwenhuizen (2011). "Frequency Domain Multiplexed Readout of TES Detector Arrays With Baseband Feedback". In: *Applied Superconductivity, IEEE Transactions on* 21.3, pp. 289–293. DOI: 10.1109/TASC.2010.2101998 (Cited on page 10).
- Hogg, R. V., J. McKean, and A. T. Craig (2012). *Introduction to mathematical statistics*. 2nd ed. Pearson (Cited on page 109).
- Holland, W. S. et al. (2013). "SCUBA-2: the 10 000 pixel bolometer camera on the James Clerk Maxwell Telescope". In: *Monthly Notices of the Royal Astronomical Society* 430.4, pp. 2513–2533. DOI: 10.1093/mnras/sts612 (Cited on pages 9, 10).
- Horwitz, P. and W. Hill (1989). *The art of electronics*. 2nd ed. Cambridge University Press (Cited on pages 39, 98).
- INA103 Data Sheet* (2000). Texas Instruments. URL: <http://www.ti.com/product/ina103> (Cited on pages 99, 102, 103, 105).
- INA111 Data Sheet* (2010). Texas Instruments. URL: <http://www.ti.com/lit/ds/symlink/ina111.pdf> (Cited on page 83).
- Irvin, J. C. (1962). "Resistivity of Bulk Silicon and of Diffused Layers in Silicon". In: *Bell System Technical Journal* 41.2, pp. 387–410. ISSN: 1538-7305. DOI: 10.1002/j.1538-7305.1962.tb02415.x (Cited on page 51).
- Irwin, K. D. (1995). "An application of electrothermal feedback for high resolution cryogenic particle detection". In: *Applied Physics Letters* 66.15, pp. 1998–2000. DOI: 10.1063/1.113674 (Cited on page 7).

- Jaeger, R.M., H. Kuhlenbeck, H.-J. Freund, M. Wuttig, W. Hoffmann, R. Franchy, and H. Ibach (1991). "Formation of a well-ordered aluminium oxide overlayer by oxidation of NiAl (110)". In: *Surface science* 259.3, pp. 235–252 (Cited on page 14).
- Johnson, J. B. (1928). "Thermal Agitation of Electricity in Conductors". In: *Phys. Rev.* 32 (1), pp. 97–109. DOI: 10.1103/PhysRev.32.97 (Cited on page 141).
- Joule, J. P. (1837). "On the Production of Heat by Voltaic Electricity." In: *Abstracts of the Papers Printed in the Philosophical Transactions of the Royal Society of London*. Vol. 4. The Royal Society, pp. 280–282 (Cited on page 30).
- Karasik, B. S. and R. Cantor (2011). "Demonstration of high optical sensitivity in far-infrared hot-electron bolometer". In: *Applied Physics Letters* 98.19, p. 193503. DOI: 10.1063/1.3589367 (Cited on page 7).
- Karasik, B. S., W. R. McGrath, M. E. Gershenson, and A. V. Sergeev (2000). "Photon-noise-limited direct detector based on disorder-controlled electron heating". In: *Journal of Applied Physics* 87.10, pp. 7586–7588. DOI: 10.1063/1.373026 (Cited on page 7).
- Karasik, B. S., D. Olaya, J. Wei, S. Pereverzev, M. E. Gershenson, J. H. Kawamura, W. R. McGrath, and A. V. Sergeev (2007). "Record-Low NEP in Hot-Electron Titanium Nanobolometers". In: *Applied Superconductivity, IEEE Transactions on* 17.2, pp. 293–297. DOI: 10.1109/TASC.2007.897167 (Cited on page 7).
- Keithley 220 Programmable Current Source Data Sheet* (2009). Keithley. URL: <http://www.keithley.com/support/data?asset=367> (Cited on page 89).
- Kuzmin, L. S. (2000). "On the concept of a hot-electron microbolometer with capacitive coupling to the antenna". In: *Physica B: Condensed Matter* 284–288, pp. 2129–2130. DOI: 10.1016/S0921-4526(99)03032-X (Cited on page 8).
- Kuzmin, L. S. (2003). "Superconducting cold-electron bolometer with proximity traps". In: *Microelectronic Engineering*. Vol. 69. 2–4. Proceedings of the Symposium and Summer School on: Nano and Giga Challenges in Microelectronics Research and Opportunities in Russia, pp. 309–316. DOI: [http://dx.doi.org/10.1016/S0167-9317\(03\)00314-9](http://dx.doi.org/10.1016/S0167-9317(03)00314-9) (Cited on page 8).
- Kuzmin, L. S. (2004). "Ultimate cold-electron bolometer with strong electrothermal feedback". In: *Proc. SPIE*. Vol. 5498, pp. 349–361. DOI: 10.1117/12.554317 (Cited on pages 8, 9, 45).
- Kuzmin, L. S., I. A. Devyatov, and D. Golubev (1998). "Cold-electron bolometer with electronic microrefrigeration and general noise analysis". In: *Proc. SPIE*. Vol. 3465, pp. 193–199. DOI: 10.1117/12.331165 (Cited on pages 7, 8).
- Lamarre, J. M. et al. (2003). "The Planck High Frequency Instrument, a third generation CMB experiment, and a full sky submillimeter survey". In: *New Astronomy Reviews* 47.111112, pp. 1017–1024. DOI: 10.1016/j.newar.2003.09.006 (Cited on page 57).

- Leivo, M. M., J. P. Pekola, and D. V. Averin (1996). "Efficient Peltier refrigeration by a pair of normal metal/insulator/superconductor junctions". In: *Applied Physics Letters* 68.14, pp. 1996–1998. DOI: 10.1063/1.115651 (Cited on page 5).
- Maffei, B. et al. (2010). "Planck pre-launch status: HFI beam expectations from the optical optimisation of the focal plane". In: *A&A* 520, A12. DOI: 10.1051/0004-6361/200912999 (Cited on page 78).
- Manninen, A. J., J. K. Suoknuuti, M. M. Leivo, and J. P. Pekola (1999). "Cooling of a superconductor by quasiparticle tunneling". In: *Applied Physics Letters* 74.20, pp. 3020–3022. DOI: 10.1063/1.124051 (Cited on page 6).
- Muhonen, J. T., M. J. Prest, M. Prunnila, D. Gunnarsson, V. A. Shah, A. Dobbie, M. Myronov, R. J. H. Morris, T. E. Whall, E. H. C. Parker, and D. R. Leadley (2011). "Strain dependence of electron-phonon energy loss rate in many-valley semiconductors". In: *Applied Physics Letters* 98.18, p. 182103. DOI: <http://dx.doi.org/10.1063/1.3579524> (Cited on pages 54, 60, 63).
- Nahum, M., T. M. Eiles, and J. M. Martinis (1994). "Electronic microrefrigerator based on a normal-insulator-superconductor tunnel junction". In: *Applied Physics Letters* 65.24, pp. 3123–3125. DOI: 10.1063/1.112456 (Cited on pages 5, 24).
- Nahum, M., P. L. Richards, and C. A. Mears (1993). "Design analysis of a novel hot-electron microbolometer". In: *Applied Superconductivity, IEEE Transactions on* 3.1, pp. 2124–2127. DOI: 10.1109/77.233921 (Cited on pages 6–8, 140).
- Nyquist, H. (1928a). "Certain topics in telegraph transmission theory". In: *American Institute of Electrical Engineers, Transactions of the* 47.2, pp. 617–644. DOI: 10.1109/T-AIEE.1928.5055024 (Cited on page 39).
- Nyquist, H. (1928b). "Thermal Agitation of Electric Charge in Conductors". In: *Phys. Rev.* 32 (1), pp. 110–113. DOI: 10.1103/PhysRev.32.110 (Cited on page 141).
- OP07 Data Sheet* (2011). Analog Devices. URL: http://www.analog.com/static/imported-files/data_sheets/OP07.pdf (Cited on page 83).
- Orlando, A. et al. (2010). "Antenna-coupled TES bolometer arrays for BICEP2/Keck and SPIDER". In: *Proc. SPIE*. Vol. 7741, 77410H. DOI: 10.1117/12.857914. arXiv: 1009.3685 [astro-ph.IM] (Cited on page 10).
- Otto, E., M. Tarasov, P. K. Grimes, A. Chekushkin, L. S. Kuzmin, and G. Yassin (2013). "Optical response of a titanium-based cold-electron bolometer". In: *Superconductor Science and Technology* 26.8, p. 085020. DOI: 10.1088/0953-2048/26/8/085020 (Cited on pages 8, 9, 45).
- Parmenter, R. H. (1961). "Enhancement of Superconductivity by Extraction of Normal Carriers". In: *Phys. Rev. Lett.* 7 (7), pp. 274–277. DOI: 10.1103/PhysRevLett.7.274 (Cited on pages 5, 6).

- Pearson, G. L. and J. Bardeen (1949). "Electrical Properties of Pure Silicon and Silicon Alloys Containing Boron and Phosphorus". In: *Phys. Rev.* 75 (5), pp. 865–883. DOI: 10.1103/PhysRev.75.865 (Cited on page 50).
- Pekola, J. P. (2005). "Low-temperature physics: Tunnelling into the chill". In: *Nature* 435.7044, pp. 889–890. DOI: 10.1038/435889a (Cited on page 6).
- Prest, M. J., J. T. Muhonen, M. Prunnila, D. Gunnarsson, V. A. Shah, J. S. Richardson-Bullock, A. Dobbie, M. Myronov, R. J. H. Morris, T. E. Whall, E. H. C. Parker, and D. R. Leadley (2011). "Strain enhanced electron cooling in a degenerately doped semiconductor". In: *Applied Physics Letters* 99.25, p. 251908. DOI: 10.1063/1.3670330 (Cited on pages 6, 8, 31, 54, 63).
- Rhoderick, E. H. and R. H. Williams (1988). *Metal-semiconductor contacts*. 2nd ed. Clarendon Press Oxford (Cited on page 16).
- Richards, P. L. (1994). "Bolometers for infrared and millimeter waves". In: *Journal of Applied Physics* 76.1, pp. 1–24. DOI: 10.1063/1.357128 (Cited on page 65).
- Rieke, G. H. (2007). "Infrared Detector Arrays for Astronomy". In: *Annual Review of Astronomy and Astrophysics* 45.1, pp. 77–115. DOI: 10.1146/annurev.astro.44.051905.092436 (Cited on page 81).
- Roccaforte, F., F. La Via, V. Rainieri, P. Musumeci, L. Calcagno, and G.G. Condorelli (2003). "Highly reproducible ideal SiC Schottky rectifiers: effects of surface preparation and thermal annealing on the Ni/6H-SiC barrier height". In: *Applied Physics A* 77.6, pp. 827–833. DOI: 10.1007/s00339-002-1981-8 (Cited on page 14).
- Salatino, M., P. de Bernardis, L. S. Kuzmin, S. Mahashabde, and S. Masi (2014). "Sensitivity to Cosmic Rays of Cold Electron Bolometers for Space Applications". In: *Journal of Low Temperature Physics* 176.3–4, pp. 323–330. DOI: 10.1007/s10909-013-1057-5 (Cited on page 9).
- Savin, A., M. Prunnila, J. Ahopelto, P. Kivinen, P. Törmä, and J. Pekola (2003). "Application of superconductor-semiconductor Schottky barrier for electron cooling". In: *Physica B: Condensed Matter* 329–333, Part 2. Proceedings of the 23rd International Conference on Low Temperature Physics, pp. 1481–1484. DOI: 10.1016/S0921-4526(02)02400-6 (Cited on page 6).
- Savin, A., M. Prunnila, P. P. Kivinen, J. P. Pekola, J. Ahopelto, and A. J. Manninen (2001). "Efficient electronic cooling in heavily doped silicon by quasiparticle tunneling". In: *Applied Physics Letters* 79.10, pp. 1471–1473. DOI: 10.1063/1.1399313 (Cited on page 6).
- Schmidt, D. R., K. W. Lehnert, A. M. Clark, W. D. Duncan, K. D. Irwin, N. Miller, and J. N. Ullom (2005). "A superconductor-insulator-normal metal bolometer with microwave readout suitable for large-format arrays". In: *Applied Physics Letters* 86.5, p. 053505. DOI: <http://dx.doi.org/10.1063/1.1855411> (Cited on page 10).

- Schottky, W. (1918). "Über spontane Stromschwankungen in verschiedenen Elektrizitätsleitern". German. In: *Annalen der Physik* 362.23, pp. 541–567. ISSN: 1521-3889. DOI: 10.1002/andp.19183622304 (Cited on page 35).
- Schottky, W. (1939). "Zur Halbleitertheorie der Sperrsicht- und Spitzengleichrichter". German. In: *Zeitschrift für Physik* 113.5–6, pp. 367–414. DOI: 10.1007/BF01340116 (Cited on page 14).
- Sesame Workshop (2015). *Mr. Snuffleupagus - Muppets - Sesame Street - Sesame Street*. URL: www.sesamestreet.org/muppets/mr-snuffleupagus (visited on 21/01/2015) (Cited on page 72).
- Shannon, C. E. (1949). "Communication in the presence of noise". In: *Proceedings of the IRE*. Vol. 37. 1. IEEE, pp. 10–21. DOI: 10.1109/JRPROC.1949.232969 (Cited on page 39).
- SRON (2014). *A new start for the SPICA mission*. Press Release. URL: <http://www.sron.nl/news-mainmenu-588/press-releases-mainmenu-686/3927-a-new-start-for-the-spica-mission> (Cited on page 10).
- Welser, J., J. L. Hoyt, and J. F. Gibbons (1994). "Electron mobility enhancement in strained-Si n-type metal-oxide-semiconductor field-effect transistors". In: *Electron Device Letters, IEEE* 15.3, pp. 100–102. ISSN: 0741-3106. DOI: 10.1109/55.285389 (Cited on page 54).

Acronyms

ADR Adiabatic Demagnetisation Refrigerator. 66,
Glossary: adiabatic demagnetisation refrigerator

CEB Cold Electron Bolometer. 8, 81, 82, 112,
Glossary: cold electron bolometer

DAQ Data acquisition unit. 83, 89

FFT Fast Fourier Transform. 86, 88,
Glossary: Fast Fourier Transform

HEB Hot Electron Bolometer. 5,
Glossary: Hot Electron Bolometer

IV current-voltage measurement where one of the quantities is varied and the response in the other is recorded. 23, 41, 82, 83, 88, 95

JFET Junction Field Effect Transistor. 99, 112,
Glossary: JFET

NEP Noise Equivalent Power. 39,
Glossary: noise equivalent power

NIS Normal metal-Insulator-Superconductor. 5–8

RMS Root Mean Square. 40,
glossary: Root mean square

RTD Resistance Temperature Detector. 82,
Glossary: Resistance Temperature Detector

SiCEB Silicon Cold Electron Bolometer. 81, 89, 116,

Glossary: Silicon Cold Electron Bolometer

SINIS Superconductor-Insulator-Normal metal-Insulator-Superconductor. 5, 6

SIS Superconductor-Insulator-Superconductor. 5, 6

SIS' Superconductor-Insulator-(different) Superconductor. 8

SIS'IS Superconductor-Insulator-(different) Superconductor-Insulator-Superconductor, sometimes written as SIS'IS. 6

SNR Signal-to-noise ratio. 39,

Glossary: signal-to-noise ratio

SQUID Superconducting QUantum Interference Device. 81,

Glossary: SQUID

SSmS Superconductor-Semiconductor-Superconductor, a type of tunnelling structure used to make SiCEBs. 6, 17

Glossary

3-dB bandwidth The frequency at which the throughput of an electrical circuit or component has fallen by a factor of 3 dB (one half in power or root two in amplitude). 86, 102

Adiabatic demagnetisation refrigerator A type of cryogenic refrigerator which uses changes in a salts entropy to achieve temperatures of a few millikelvin above absolute zero. 65

Cold electron bolometer A bolometric detector that utilises tunnelling contacts as both sensitive thermometers as well as to offer direct electron cooling. The main study of this work. 8, 10, 45, 81

Common-mode A signal which adds to both lines of a differential pair with the same sign and thus does not alter the voltage difference between the pair. This should be rejected by the measurement system. 94, 95.

See also: differential signal & normal-mode

Convolution A mathematical process performed on two functions which produces a third function whose value is given by the area overlap of the two functions after one has been reversed and then translated across the other. 109, 112.

See also: cross-correlation

Cross-correlation A mathematical process which is used to determine the similarity of two signals. 112.

See also: convolution

Current responsivity, S_I The change in current flowing through a voltage biased detector per unit power of radiation absorbed. 30, 32.

See also: responsivity

Differential signal A differential signal sends voltages across a pair of wire as

opposed to a single conductor. The voltage is measured by an amplifier which measures the voltage difference between the two wires. Usually the two conductors have equal and opposite voltage. Only changes which alter the voltage difference between the two are measured. 93, 94, 103, 105.

See also: common-mode & normal-mode

Electromagnetic pickup Electromagnetic pickup describes the phenomenon of stray electronic signals coupling to another signal and degrading the signal quality. This is often from signals on ground or power lines or from radio signals coupling to poorly shielded cabling. 90, 95

Fast Fourier Transform An algorithm used to compute the Fourier Transform of a signal. As is implied by the name a Fast Fourier Transform is notably faster than other methods. The most common method was constructed by Cooley and Tukey, 1965 and involves breaking down the matrix into smaller matrices and multiplication factors. 86.

See also: Fourier Transform

Fourier Transform A transform function which converts a spatial signal into a one in the frequency domain or vice versa. 103

Ground loop An unwanted current which flows between two points which are suppose to be at the same potential. A ground loop is created when two circuits are independent except for sharing a common connection to ground, if this connection has a non-zero resistance and one of the circuits has an additional connection to ground, this and the common resistance to ground, act as a potential divider causing some voltage to be dropped across the resistor and thus a current to flow to ground. This current can then flow back through the circuit from other ground points. 92

Hot Electron Bolometer A bolometric detector where incident power heats the electrons above the temperature of the lattice. Incident power is measured by a sensitive electron thermometer. First proposed by Nahum, Richards, and Mears (1993). 5, 6, 10

JFET Junction Field Effect Transistor. A three terminal semi-conductor based electronic component. A potential applied to the middle of the three terminals (the gate) controls the size of a depletion region between the other two terminals

(the source and the drain). They are commonly used as switches, amplifier or as a resistor whose resistance can be controlled via a voltage. 99, 100

Jitter The amount a supposedly constant signal varies about the expected value due to electronic noise or other influences. 89, 90, 95, 96, 106, 107

Johnson noise A form of noise generated with resistive electronic components. It is caused by thermal agitation of a charge in the component. Johnson noise can exist even if there is no circuit connected to the resistive component since the charges will still move (and collide) randomly due to thermal excitations. First described by Johnson, 1928 and further explained by Nyquist, 1928b. 39, 41

Noise In this work *noise* is always taken to mean electrical noise (as opposed to acoustic noise). This is the uncertainty of a measurement due to anyone of a number of factors, which commonly include fluctuations in the energy of charge carriers, contamination of one signal by another or statistical fluctuations in power. 34

Noise equivalent power The noise equivalent power is the a figure of merit for a detector or instrument system. It is the signal power required to achieve a signal-to-noise ratio of unity with an integration time of half a second

add see alsos for SNR and bandwidth

. 7, 8, 39–44.

See also: signal-to-noise ratio

Normal-mode A signal which adds to the two conductors of a differential pair with opposite signs, or to only one of the conductors, and thus alters the voltage difference between the pair. This is measured at the readout stage. 95.

See also: common-mode & differential signal

Ohmic contact A junction between a metal and a semiconductor which exhibits no rectifying behaviour. 16

Potential divider An electrical component used to reduce a voltage by a defined factor. Typically made of a pair of impedances one (Z_1) in line to the output and the other (after the first) to ground (Z_2). The voltage at the output is equal to the input voltage multiplied by the ratio of the impedance to ground to the total impedance. That is to say $V_{out} = \frac{Z_2}{Z_1+Z_2} \times V_{in}$. 105

Resistance Temperature Detector A secondary thermometer where the electrical resistance of the thermometer is usually inversely proportional to temperature. 82

Responsivity, S The change in a measured signal per unit of power of radiation absorbed by a detector. A *system or instrument responsivity* may be defined as the change in signal per unit of power of radiation arriving at the system (i.e. the *system responsivity* accounts for losses within the system). 30.

See also: current responsivity & voltage responsivity

Root mean square A measure of the amplitude of a varying signal or function. 40

Signal-to-noise ratio, SNR The ratio of the signal amplitude to the noise amplitude. A signal-to-noise ratio of ≤ 1 means that the signal cannot be distinguished from the noise. 39, 40, 42

Silicon Cold Electron Bolometer A form of cold electron bolometer where the central absorbing island is made from silicon and the tunnelling contacts are Schottky barriers formed naturally between the silicon and the superconducting contacts. 81

Source follower An element of an electrical circuit which utilises a transistor (usually in the form of a JFET) as a voltage buffer. This is normally to offer a low input impedance to subsequent electronic components or to isolate components being measured via a high input impedance. 99, 100.

See also: JFET

SQUID Superconducting QUantum Interference Device - a type of low-noise current amplifier, typical used at cryogenic temperatures. 81

Triaxial cable A form of electronic interconnect cable often used in sensitive low current measurements. It is similar the more standard coaxial cable but includes an additional inner-shield (guard) in an attempt to reduce any leakage current from the central conductor to the shield. 89

Voltage responsivity, S_V The change in voltage flowing through a current biased detector per unit power of radiation absorbed. 30, 32, 34, 41–43.

See also: responsivity

White noise Noise is being defined as being *white* if it is present at all frequencies and has a constant mean amplitude across these frequencies. 86, 89, 102,

List of Figures

2.1 Schematic of a simple bolometer.	4
3.1 Growth and chemical fabrication of a metal-oxide layer	13
3.2 Formation of a Schottky barrier	15
3.3 Possible tunnelling of charges in a SiCEB	17
3.4 Tunnelling in of charges across a positively biased device	18
3.5 Tunnelling in of charges across a negatively biased device	19
3.6 BCS model of the superconducting energy gap	23
3.7 Dependance of tunnelling current on electron temperature	25
3.8 Most likely route for charges to tunnel in a two junction system.	26
3.9 Examples of the physical effects of various signal-to-noise ratios	40
4.1 Band structure of an intrinsic semiconductor	46
4.2 Crystal lattice of silicon with an n-type dopant inserted.	47
4.3 Crystal lattice of silicon with a p-type dopant inserted.	48
4.4 Energy level diagrams for doped semiconductors	49
4.5 Change in electron mobility with increasing donor concentration	52
4.6 Introducing strain into a silicon lattice	53
5.1 Model of SiCEB detector chip	56
5.2 Key dimensions of a twin-slot antenna	57
5.3 Model of SiCEB detector chip with DC cuts in the ground plane	58
5.4 Dimensions of bolometer bridge in a coplanar waveguide	59
5.5 Example sections from photomask	60
5.6 Cross sections of strained and unstrained SiCEB structures and photograph of a fabricated detector	62

6.1	Artistic impression of the cross section of a sorption refrigerator	67
6.2	Artistic impression of a simple single-stage adiabatic demagnetisation refrigerator	70
6.3	Computer-generated model of Aloysius cryostat	73
6.4	Filters used for optical measurement in Aloysius	74
6.5	Photograph of cryostat housing the adiabatic demagnetisation refrigerator used for testing detectors	76
6.6	Filter profile of filters used in optical measurement cryostat	77
6.7	Optical components housed in cryostat used for optical measurements .	78
6.8	Photograph of cryostat used for optical measurements	79
6.9	Detector holder	80
7.1	Initial readout system using RTD amplifier and programmable current source	83
7.2	Noise model of series amplifiers	84
7.3	Gain measurement of original amplifier	85
7.4	Bandwidth measurement of original amplifier	87
7.5	Input referred noise of original amplifier	88
7.6	Jitter from a Keithley 220 Current Source	90
7.7	Noise spectrum from a Keithley 220 Current Source	91
7.8	Internal bias generator used with initial amplifier	93
7.9	Rejection of common-mode noise in a differential bias and readout system	95
7.10	Jitter from initial, custom made, current bias system.	96
7.11	Noise spectrum from original bias generator system, used in conjunction with the initial amplifier.	97
7.12	Final voltage Readout Amplifier	99
7.13	Gain measurement of final amplifier	100
7.14	Asymmetric limit to input of the final amplifier	101
7.15	Bandwidth measurement of final amplifier	103
7.16	Measurement of the internal noise, referred to the input, for the final amplifier.	104
7.17	Differential bias generator used with final readout system.	105
7.18	Measurement of jitter from the bias generator used in conjunction with the final readout system.	107

7.19 Noise measurement bias generator used in conjuncture with the final readout system.	108
7.20 Graphical representation of convolution in the time domain.	110
7.21 Convolution in the frequency domain.	111
7.22 Cross correlated noise measurement process flow	113
7.23 Removal of amplifier noise from a measurement by the use of cross correlation.	114
7.24 Reduction in input-referred noise with increased number of averaged acquisitions for cross-correlated amplifiers	115
8.1 Current-voltage characteristics for a SiCEB with an unstrained absorber	120
8.2 Differential resistance for a SiCEB with an unstrained absorber	122
8.3 Electron-temperature fitting for SiCEB with an unstrained absorber . .	124
8.4 Current-voltage characteristics for a SiCEB with a strained absorber . .	125
8.5 Differential resistance of a SiCEB with a strained absorber	126
8.6 Electron temperature for a Strained-Silicon Cold Electron Bolometer . .	127

List of Tables

4.1 Carrier mobility curve-fitting parameters from Caughey and Thomas (1967)	52
5.1 Dimensions of designed antennae	57
5.2 Dimensions and expected contact resistance for different bolometer bridge designs	59
5.3 Summary of key material properties for unstrained (control) and strained silicon materials	63
7.1 Summary of detector bias systems	116
7.2 Summary of detector readout systems	117

Todo list

■ Probably just going to wrap all of this into the introduction	3
■ hunt a reference for this	5
■ Ref.	5
■ Add glossary entry: add Electrothermal feedback	7
■ Add glossary entry: TES	7
■ Add glossary entry: FDM TDM acr and gls	9
■ Add glossary entry: TES acr and gls	10
■ Add section on applications???	10
■ Add glossary entry: add Schottky Barrier	12
■ These images are PNGs and need changing to PDFs when pagroup error is fixed	12
■ cite	12
■ list and cite	12
■ These are PNGs and need setting back to vectors when pdflatexc fix is done	14
■ add glossary entry	16
■ Maybe rewrite equation with $R_N/2$	23
■ Add glossary entry: Amplifier Noise	35
■ work out how this is done	38
■ Add glossary entry: Sampling theorem and measurement bandwidth . .	39
■ maybe change to $\langle \delta V \rangle_{tot}$	41
■ Add ref to where amp. noise is covered	41
■ Add glossary entry: add shot noise	43
■ Go back and check that I use “current shot noise” consistently (I don’t!). .	44
■ maybe add a ref?	47
■ Add glossary entry: doping	47
■ Add glossary entry: holes	48

	Switch to vectors	48
	Add glossary entry: mobility	50
	Switch to vectors	53
	Optical Properties and modelling (FP model).	54
	add ref	58
	add footnoted references	58
	and illustrated in...???	60
	Add cross-ref	65
	Update to re-rendered image	69
	Check if I should italicise this.	78
	...maybe add glossary for this	101
	Add glossary entry	108
	Change back to PDF	111
	Change back to PDF	113
	Check this, simulation should, should possibly start at Vamp, check what averaging does to a single amplifier	116
	For any acronyms which have glossary entries, make the glossary the main key used and include first = { gls acr:*	117
	Check figures for correct hyphenation of input-referred noise. Check text for correct hyphenation of cross-correlated amplifiers and IRN (only when compound adjective)	117
	Maybe plots curves of V vs T at various biases	128
	add see alsos for SNR and bandwidth	141